Analysis and evaluation of the pulse shape performance of an Inverted Coaxial HPGe detector for $0\nu\beta\beta$ Experiments

Dissertation

der Mathematisch-Naturwissenschaftlichen Fakultät

der Eberhard Karls Universität Tübingen

zur Erlangung des Grades eines

Doktors der Naturwissenschaften

(Dr. rer. nat.)

vorgelegt von

Andreas Zschocke

aus Buchholz in der Nordheide

Tübingen

2020

Gedruckt mit Genehmigung der Mathematisch-Naturwissenschaftlichen Fakultät der Eberhard Karls Universität Tübingen.

Tag der mündlichen Qualifikation: 05.02.2021

Stellvertretender Dekan: Prof. Dr. József Fortágh

1. Berichterstatter: Prof. Dr. Josef Jochum

2. Berichterstatter: Prof. Dr. Tobias Lachenmaier

Abstract

One of the most challenging tasks in modern particle physics is the search of the neutrinoless double beta decay ($0\nu\beta\beta$). The existence of this radioactive process would directly imply physics beyond the standard model of particle physics. Searches of the $0\nu\beta\beta$-decay require great efforts and background events must be reduced drastically in order to gain the needed sensitivity.

^{76}Ge is a promising isotope for $0\nu\beta\beta$ experiments, since it can be manufactured into high purity germanium detectors (HPGe), unifying the source and the detector. The HPGe detector technology is well established, but is still open to improvements. The ideal instrument for $0\nu\beta\beta$ searches would be a large and massive HPGe detector with an excellent energy resolution and a pulse shape discrimination capability. The newly developed inverted coaxial HPGe detectors are promising candidates to provide these characteristics.

In this work, one inverted coaxial point contact (ICPC) detector, developed by ORTEC, has been extensively tested. It will be shown, that the high requirements on energy resolution and pulse shape discrimination performance can be fulfilled, which enables a use of this detector type for future $0\nu\beta\beta$ experiments.

Furthermore, the response to α particles on the passivated surface, a surface that separates the high voltage contact from the read out contact, has been measured in the TUBE surface scanner, a scanning system located at the Technische Universität München. Due to its small thickness, the passivated surface is vulnerable to α radiation and can therefore be a window to unwanted background contributions. The analysis of this scan will reveal that the pulse shapes of the α surface events are heavily distorted and their measured energy drastically decreases. A multivariate cut procedure has been developed, that removes these Alpha surface events with high accuracy.

This work helps in the understanding of the pulse shapes of ICPC detector types in general, and of passivated surface events in particular.

Zusammenfassung

Eine der größten Herausforderungen in der modernen Teilchenphysik ist die Suche nach dem neutrinolosen doppeltem Betazerfall ($0\nu\beta\beta$). Dieser radioaktive Prozess ließe sich nur mit Physik jenseits des Standardmodells beschreiben. Die Suche nach diesem Zerfall erfordert außergewöhnliche Anstrengungen. Hintergrundereignisse müssen nahezu vollständig beseitigt werden, um die nötige Sensitivität für eine Detektion des Zerfalls zu erreichen.
Ein vielversprechender Ansatz ist die Suche des $0\nu\beta\beta$-Zerfalls am Isotop ^{76}Ge, da ^{76}Ge zu einem hochreinen Halbleiterdetektor verarbeitet werden kann. Dadurch wäre Quelle und Detektor identisch, was eine hohe Quanteneffizienz ermöglicht. Germanium-Halbleiterdetektoren sind zudem eine sehr gut verstandene und kommerziell nutzbare Technologie, die jedoch immernoch Raum für Optimierungen lässt. Für die $0\nu\beta\beta$-Suche sollte ein idealer Germanium-Detektor möglichst groß sein, über eine hervorragende Energieauflösung verfügen und Pulsformanalysen ermöglichen. Der "Inverted Coaxial Point Contact" Detektortyp (ICPC) könnte den hohen Anforderungen entsprechen.

In dieser Arbeit wurde solch ein ICPC-Detektor der Firma ORTEC detailliert untersucht und auf seine Eigenschaften bezüglich der Energieauflösung und Pulsformanalyse getestet. Es wird gezeigt, dass die getesteten Charakteristiken den Anforderungen entsprechen, und dass sich der ICPC Detektortyp für die Suche nach dem $0\nu\beta\beta$ Zerfall eignet.
Des Weiteren wurde die passivierte Oberfläche zwischen den elektrischen Kontakten mit Alphateilchen beschossen und die Reaktion des Detektors auf diese Ereignis Klasse analysiert. Aufgrund ihrer geringen Dicke ist die passivierte Oberfläche anfällig für das Eindringen externer Radioaktivität. Diese Untersuchungen wurden in dem TUBE-Oberflächenscanner der Technischen Universität München durchgeführt. Es wird gezeigt, dass die Pulsform dieser Alpha-Oberflächenereignisse stark verformt ist, und dass die gemessene Energie stark reduziert ist. Eine multivariate Prozedur wurde entwickelt, die diese Alpha-Oberflächenereignisse mit hoher Genauigkeit entfernt.
Das Ergebnis dieser Arbeit hilft beim Verständnis der Signale eines ICPC Detektortyps im Allgemeinen, und beim Verständnis von Ereignissen in der passivierten Oberfläche im Speziellen.

Contents

1 Introduction

In modern particle physics the neutrino might be one of the most interesting and one of the strangest particles. It is a particle that only interacts via the weak interaction, which makes the reaction rate with matter exceptionally rare compared to processes of the electromagnetic or the strong force. The mean free path of neutrinos with kinetic energies of a few MeV is in the order several light years. This makes experiments that want to study the neutrino and its properties complex and great efforts have to be made in order to gain the needed sensitivity to measure such small cross sections.

In the standard model of particle physics (SM) the neutrino is described as a massless, uncharged, spin 1/2 fermion, which comes in three different flavors, that are related to their charged partners (e^-, ν_e), (μ^-, ν_μ), (τ^-, ν_τ) and their corresponding antiparticles $(e^+, \overline{\nu}_e)$, $(\mu^+, \overline{\nu}_\mu)$, $(\tau^+, \overline{\nu}_\tau)$. The weak interaction is maximal parity violating and neutrinos are only observed with defined chiral states. The neutrinos ν_α, the subscript α indicates the flavor state, are only observed as left-handed particles, whereas the antineutrinos $\overline{\nu}_\alpha$ are only observed as right-handed neutrinos, which is consistent with the assumption that the neutrino is a massless particle.

However, from the phenomenon of the neutrino oscillation it is known that neutrino must have different mass eigenstates and therefore the flavor neutrinos and antineutrinos also must be massive. This contradicts the assumption from the standard model and makes neutrinos beyond standard model (BSM) particles.

The question, how neutrinos can be massive particles and why their masses are so extremely small, could be answered if neutrinos were Majorana particles, making them their own antiparticle. The quest to observe the Majorana character of the neutrino has been pursued for many years and is still one of the most challenging tasks in modern physics.

The Germanium Detector Array experiment GERDA and its successor, the LEGEND experiment, are designed to measure the neutrinoless double β-decay of ^{76}Ge isotopes. The existence of such a $0\nu\beta\beta$-decay is equivalent to the existence of the Majorana character of the neutrino. The exceptional long half life of such a decay needs tremendous efforts in order to gain the needed sensitivity. Therefore, large amounts of ^{76}Ge are fabricated into high purity Germanium detectors (HPGe) and are operated in the an ultra low background environment. However, background events will still be present and can lead to a drastic decrease in sensitivity

and hence a background free operation is desired.
A big impact on the background reduction is given by the offline pulse shape discrimination (PSD). The measured signals are analyzed and background events can be discriminated by their pulse shapes. Such a PSD is not valid for every detector type, and the detector geometry and design are therefore important aspects. The Inverted Coaxial Point Contact detector type (ICPC) provides an excellent energy resolution and a good pulse shape discrimination.
Radioactive α decays are the biggest external background sources at the Q-Value of the $0\nu\beta\beta$-decay $Q_{\beta\beta}$ in the GERDA experiment. Their pulse shapes must be understood in great detail for a sufficient background reduction. The ICPC detector design has large, but very thin, passivated layer (PL), dividing the electric contacts from each other. This PL is vulnerable to α particle penetration, which may oppose a threat to the $0\nu\beta\beta$-decay search. Therefore the pulse shapes of such α surface events must be understood in great detail.

In this work, one ICPC detector, manufactured by ORTEC, have been tested extensively and its characteristic performance statistics have been analyzed and compared to simulations. Furthermore, the response of α particles to the vulnerable passivated surface of the detectors has been measured and analyzed in detail. Existing pulse shape parameters, that discriminate α surface events, have been investigated and refined. Based on this parameter, a multivariate pulse shape discrimination cut has been developed, which efficiently removes these α surface events.

This work will firstly give an overview of the neutrino physics in chapter 2, followed by a description of the GERDA experiment in 3 and the Germanium detector technology in 4. Then, the performed measurements and analysis procedures will be introduced and the α surface pulse shape discriminator will be presented in 5. Finally, the results of the α surface event measurements and the development of the α surface cut will be reported in 6.

2 Neutrino Physics

This chapter will give a brief introduction to the theory of the neutrino, to important milestone experiments within the 90 year long history of the neutrino and the principle of the Majorana formalism. Most of the following has been adopted from [Sch97].

The neutrino has been postulated by Wolfgang Pauli in 1930 in his famous letter to the "radioactive" group of physicists at a conference in Tübingen ("Liebe Radioaktive Damen und Herren") [Pau30]. The purpose of his proposed "neutron" (the name "neutrino", little neutron, has been given by Enrico Fermi 1933 to distinguish it from the newly discovered neutron by Chadwick in 1932 [Cha32]) was to save the conservation of angular momentum as well as the conservation of energy within β-decays. In a β-decay a neutron n of a mother nucleus decays into a proton p, an electron e^- and additional non-charged electron antineutrino $\overline{\nu}_e$.

$$n \longrightarrow p + e^- + \overline{\nu}_e$$

This is a three body decay and the total energy is distributed among all decay products resulting in a continuous e^- energy spectrum. If the β-decay was a two body decay without the emission of the $\overline{\nu}_e$ and if energy conservation is not violated, the e^- would receive a fixed energy only determined by the mass difference between the mother and daughter nuclei. Therefore, the observed continuous β-spectrum either violates the energy conservation or an additional uncharged decay product is emitted alongside.
A similar motivation in the introduction of the $\overline{\nu}_e$ lies within conservation of the angular momentum and its connected quantum mechanical spin statistics. In β-decays both the mother and the daughter nucleus have either an odd or an even spin. The e^- however carries the spin $J = \frac{1}{2}$. Therefore, either the angular momentum is not conserved or an additional particle is emitted alongside, also carrying the spin $J = \frac{1}{2}$.

The great challenge was to experimentally prove the existence of the Neutrinos and it took another 26 years and the development of nuclear reactors as antineutrino sources, to build an experiment sensitive enough to measure these uncharged $J = \frac{1}{2}$ particles.
Even today great efforts have to be made in order to investigate neutrino properties and neutrino experiments remain a difficult venture.

2.1 Neutrino Experiments

In 1956 Reines and Cowan proved the existence of the $\overline{\nu}_e$ via the inverse β-decay reaction [CRHK56] [RC56]

$$\overline{\nu}_e + p \longrightarrow e^+ + n$$

on cadmium chloride target, which was dissolved in water, placed close to a nuclear reactor. The emitted e^+ from the inverse β-decay annihilates immediately into two monochromatic photons, which are detected by surrounding scintillation detectors. After a few μs, the n from the inverse β-decay will be captured on a Cd isotope. The following deexcitation of the Cd leads to an emission of another photon which also can be detected. The signature of the inverse β-decay is therefore the detection of two γ signals a few μs apart from each other. The measured cross section of $\mathcal{O}(10^{-43}\,\mathrm{cm}^2)$ was well in agreement with Fermis theory of the β-decay.
The inverse β^+ decay could not be observed with the emitted reactor $\overline{\nu}_e$ [DJ55]. This lead to the conclusion that ν_e and $\overline{\nu}_e$ are different particles which can be characterized by a lepton number L which is 1 for every lepton, e.g. (ν_e, e^-), and -1 for every anti-lepton, e.g. ($\overline{\nu}_e$, e^+). In general, no process has been observed so far that violates the lepton number.

Only one year after the first neutrino detection the famous Wu-experiment [WAH$^+$57] showed that parity is not conserved within the weak interaction and another year later, Goldhaber directly measured the helicity of the neutrino [GGS58], showing that ν_e are always left-handed particles, whereas $\overline{\nu}_e$ are always right-handed. These observations led to the conclusion, that the neutrino is a massless particle with a fixed helicity, where only left-handed ν_e and right-handed $\overline{\nu}_e$ are participating in weak interaction.

In the late 60's first measurements of the solar neutrino flux measured a deficit of the incoming ν_e, leading to the so-called solar neutrino problem [DJ64] [BD76]. The measured ν_e flux on Earth was only around one third of the expected flux, if nuclear fusion was the dominant process of the energy generation in the sun. Attempts to resolve this problem by modulating the standard solar model failed.
Another proposed solution was to introduce the idea of a neutrino mixing in the weak interaction analogous to quark flavor mixing. More than 20 years later this idea could be experimentally confirmed by the *Super-Kamiokande* [FFH$^+$03] experiment and the *Sudbury Neutrino Observatory* (SNO) [BHR$^+$00] which was awarded with the Nobel price in 2015 [Tar15].

For the idea of neutrino oscillation, the neutrino needs to consists of different mass eigenstates, which are different from neutrino flavour eigenstates. The flavour eigenstates ν_e, ν_μ, ν_τ are superpositions of the three mass eigenstates ν_1, ν_2, ν_3 and the mass eigenstates are again a superposition of the flavor eigenstates. Only the flavor eigenstates participate in the weak interaction, whereas the mass eigenstates affect the propagation of the neutrinos. A neutrino which is produced in the Sun is produced as a pure electron neutrino ν_e, composed of a mixture of the three mass eigenstates. As the neutrino travels to the Earth, the phases of the three mass eigenstates propagate differently, resulting in a different mixture. This also means that the former pure ν_e is also now partially ν_μ and ν_τ, and can be detected after the distance L as a ν_μ or ν_τ with a given probability. This probability to measure a flavor state β after the distance L of a neutrino emitted as flavor state α with the energy E can be expressed as:

$$P_{\alpha\to\beta} = \left| \sum_i U^*_{\alpha i} U_{\beta i} \cdot e^{-i m_i^2 L/2E} \right|^2 .$$

This expression holds for any number of neutrino generations. In the case of only two participating flavor states the equation reduces to

$$P_{\alpha\to\beta} = \sin^2(2\Theta) \cdot \sin^2\left(\frac{\Delta m_{12}^2 L}{4E}\right),$$

with Δm_{12}^2 as the squared mass difference between the two mass eigenstates m_1 and m_2, and Θ as the mixing angle between them. This also means, assuming three flavor states, that at least two of the mass eigenstates need to be greater than zero, making the neutrino a massive particle. This is contrary to the massless description in the SM.

In the above expression of the detection probability, the terms $U_{\alpha i}$ are the matrix elements of a mixing matrix. Analogue to the CKM matrix in the quark sector [KM73], this mixing matrix is the Pontecorvo-Maki-Nakagawa-Sakata (PMNS) matrix [MNS62] and describes the mixing of the neutrino eigenstates

$$U = \begin{pmatrix} U_{e1} & U_{e2} & U_{e3} \\ U_{\mu 1} & U_{\mu 2} & U_{\mu 3} \\ U_{\tau 1} & U_{\tau 2} & U_{\tau 3} \end{pmatrix}$$

$$U = \begin{pmatrix} 1 & 0 & 0 \\ 0 & c_{23} & s_{23} \\ 0 & -s_{23} & c_{23} \end{pmatrix} \cdot \begin{pmatrix} c_{13} & 0 & s_{13}e^{-i\delta} \\ 0 & 1 & 0 \\ -s_{13}e^{-i\delta} & 0 & c_{13} \end{pmatrix} \cdot \begin{pmatrix} c_{12} & s_{12} & 0 \\ -s_{12} & c_{12} & 0 \\ 0 & 0 & 1 \end{pmatrix} \cdot \begin{pmatrix} e^{i\alpha_1/2} & 0 & 0 \\ 0 & e^{i\alpha_2/2} & 0 \\ 0 & 0 & 1 \end{pmatrix}$$

where s_{ij} and c_{ij} are the sine and cosine of the mixing angles between the mass eigenstates ij and δ is a CP-violating phase. The parameters $\alpha_{1,2}$ are Majorana phases which only exist if the neutrino is a Majorana particle, i.e if the neutrino is its own antiparticle. These Majorana phases are irrelevant in the oscillation but, as it will be shown later, influence the strength of a possible $0\nu\beta\beta$ decay.

The absolute values of the squared mass differences Δm^2_{ij} could be experimentally found and also the sign of Δm^2_{12} could be fixed, i.e. ν_2 is heavier than ν_1. However, the sign of Δm^2_{23} is yet unknown, leading to two possible mass hierarchies where ν_3 is either the heaviest or the lightest state (see figure 2.1). Which hierarchy is realized in nature is also effecting the strength of a possible $0\nu\beta\beta$ decay and the sensitivity to measure it.

2.2 Neutrinos as Majorana particles

In the SM leptons are described as Dirac particles that can be expressed as a four component Dirac spinor ψ which satisfies the Dirac equation. The four components represent the lepton and anitlepton with a spin projection of $1/2$ or $-1/2$ respectively. The Dirac spinor can be decomposed into four chiral states ψ^D_L, ψ^D_R, $\overline{\psi}^D_L$ and $\overline{\psi}^D_R$. A SM Dirac mass term can be expressed as $m\overline{\psi}\psi$ which also can be decomposed into the chiral states:

$$m\overline{\psi}\psi = m\overline{\psi_L}\psi_R + m\overline{\psi_R}\psi_L\,, \quad \text{with } \overline{\psi_R}\psi_L = (\psi_R\overline{\psi_L})^+.$$

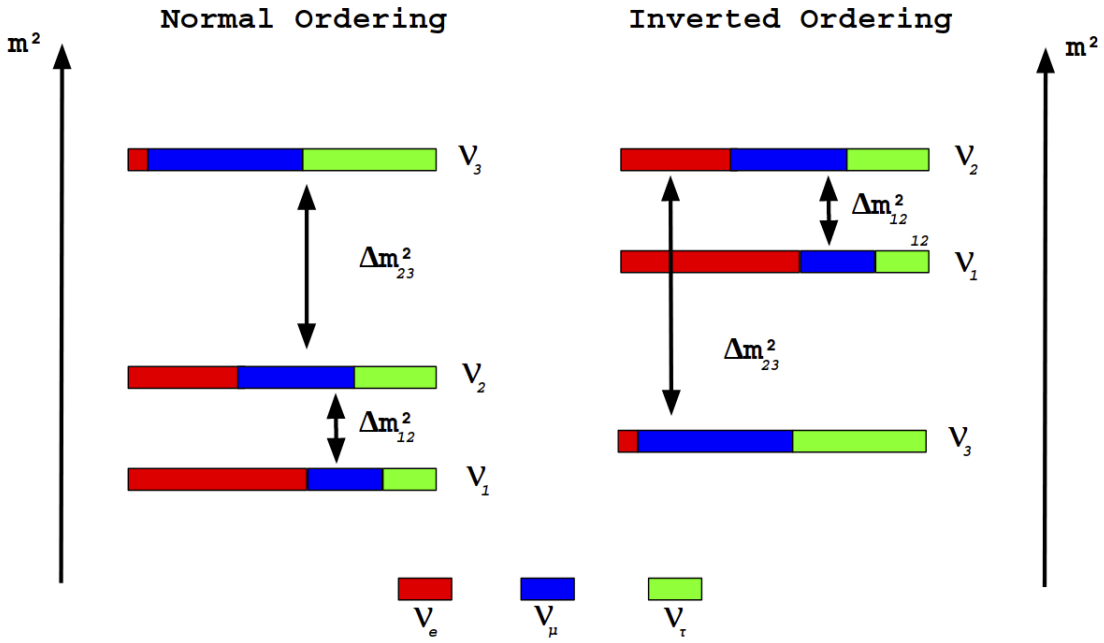

Figure 2.1: Schematic representation of the neutrino mass ordering. Left the normal ordering with ν_1 being the lightest mass eigenstate and right the inverted ordering with ν_3 being the lightest mass eigenstate.

This equation shows that a Dirac mass term requires both the left-handed and the right-handed chiral projection of the particle. The Dirac mass couples the left-handed state to the right-handed state. But since no right-handed neutrino and no left-handed antineutrino appear in the SM, the Dirac mass term for a neutrino must be zero.

From neutrino oscillation it became clear that neutrinos are in fact massive particles. Therefore another mechanism must be responsible for the generation of the neutrino masses. One possible way to assign masses to the neutrinos is via the Majorana formalism.
In the 1930's, Ettore Majorana found a way to introduce additional mass terms if a particle was its own antiparticle, a so-called Majorana particle [Maj37]. A neutrino has no electric charge and therefore is a possible Majorana particle candidate. In this case the four chiral components of the Dirac spinor would reduce to two chiral components $\nu_L = \overline{\nu}_L$ and $\nu_R = \overline{\nu}_R$.
For a Majorana neutrino, additional Majorana mass terms can be added to the Lagrangian and the most general mass term can be written as:

$$-L_m = m_D \overline{\nu}_L \nu_R + \frac{1}{2} m_L \overline{\nu_L^C} \nu_L + \frac{1}{2} m_R \overline{\nu_R^C} \nu_R + h.c,$$

or expressed as matrix equation:

$$-L_m = \begin{pmatrix} \overline{\nu_L^C} & \overline{\nu}_R \end{pmatrix} \begin{pmatrix} m_L & m_D \\ m_D & m_R \end{pmatrix} \begin{pmatrix} \nu_L \\ \nu_R^C \end{pmatrix} + h.c.,$$

in which $\begin{pmatrix} \overline{\nu_L^C} & \overline{\nu}_R \end{pmatrix}$ and $\begin{pmatrix} \nu_L \\ \nu_R^C \end{pmatrix}$ include the right-handed and the left-handed states respectively.

$$M = \begin{pmatrix} m_L & m_D \\ m_D & m_R \end{pmatrix}$$

is the mass matrix which couples the neutrino fields. In this case m_L, m_R and m_D are not the mass eigenvalues but represent the coupling strength neutrino fields to each other. The mass eigenvalues, which represent physical masses, can be found via diagonalization of the mass matrix M, resulting in two mass eigenvalues $m_{1,2}$.

If one chooses now $m_L = 0$ and $m_R \gg m_D$ the corresponding mass eigenvalues (i.e. the physical neutrino masses) become

$$m_1 = \frac{m_D^2}{m_R} \ll m_D$$

and

$$m_2 = m_R \left(1 + \frac{m_D^2}{m_R^2}\right) \approx m_R$$

This is the so called *See-Saw mechanism*. The choice of a very large m_R and a vanishing m_L naturally produces one very light physical neutrino mass and one very heavy, inactive neutrino mass, and could therefore describe the smallness of masses of the observable neutrinos. Additionally, the heavy neutrinos give rise to the idea of the so called leptogenesis. If the neutrino is a Majorana particle the lepton number L is no longer conserved. The very heavy neutrino ($m_2 \approx \mathcal{O}(10^{15}\,\mathrm{eV})$) could be produced in the early universe and could have decayed into lighter left-handed neutrinos or right-handed antineutrinos (ΔL violation) and Higgs bosons (which decay into quarks) as the universe cooled down. If the probability to decay into neutrinos was (slightly) different to decay into antineutrinos the creation of quarks (antiquarks) would also be (slightly) different. This way, the observed matter/antimatter asymmetry could also naturally arise from the *See-Saw mechanism*.

The question, whether the neutrino is its own antiparticle or not, is therefore fundamental.

2.3 The $0\nu\beta\beta$-decay

One way to probe the Majorana character of the neutrino is if a $0\nu\beta\beta$-decay can be detected. In nature, a double β-decay ($2\nu\beta\beta$) can occur on isotopes if a normal β-decay is energetically forbidden but the β-decay of two neutrons is possible and energetically preferable (see figure 2.2).

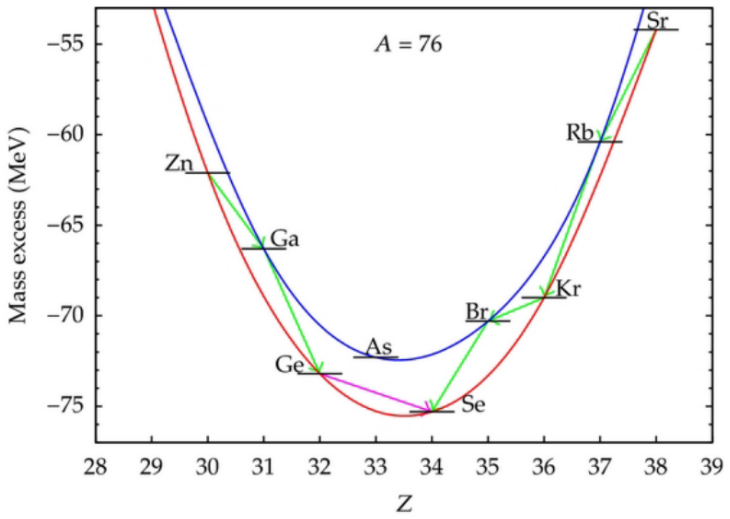

Figure 2.2: Decay scheme for isobars with $A = 76$. A normal β-decay switches between the even-even mass parabola and the odd-odd mass parabola. The normal β-decay of ^{76}Ge to ^{76}As is energetically forbidden. The $\beta\beta$-decay to ^{76}Se however is allowed. Figure taken from [Heg18].

The GERDA and the LEGEND experiment investigate the double β-decay of the ^{76}Ge isotope. In this case two neutrons of the ^{76}Ge isotope decay simultaneously into two protons under the emission of two e^- and two $\overline{\nu}_e$, forming a ^{76}Se daughter.

$$B(Z,N) \longrightarrow C(Z+2, N-2) + 2e^- + 2\overline{\nu}_e$$

However, this decay is only realized in a small number of isotopes. It is a second order process and it can only occur in nuclei with an even number of protons and an even number of neutrons. The half-life of $2\nu\beta\beta$ decays is therefore very high ($T^{2\nu}_{1/2} \approx \mathcal{O}(10^{21})$ y for ^{76}Ge).
If the neutrino was a Majorana particle, additional decay modes without an emission of the neutrinos could occur.

$$B(Z,N) \longrightarrow C(Z+2, N-2) + 2e^-$$

The simplest mechanism of such a $0\nu\beta\beta$ is the exchange of a light Majorana ν. Such a decay is shown in figure 2.3

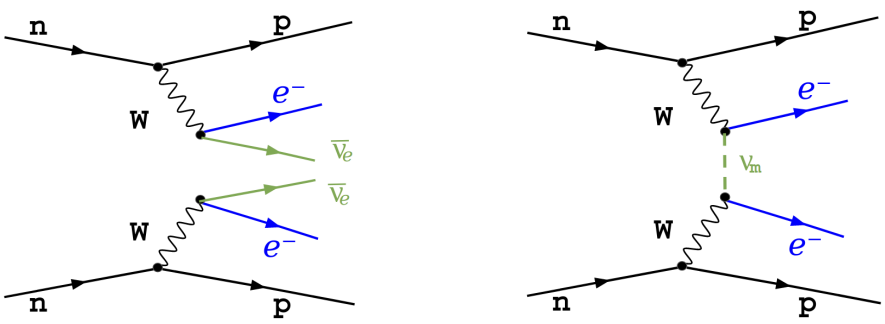

Figure 2.3: Schematic drawing of a $2\nu\beta\beta$-decay (left) and a $0\nu\beta\beta$-decay (right). The $0\nu\beta\beta$ is moderated by the exchange of a light Majorana neutrino ν_m.

If the energy of the emitted electrons is measured, the energy spectrum of the two decay types would look fundamentally different. In the $2\nu\beta\beta$-decay, the total energy of the decay (the Q-value $Q_{\beta\beta}$) is distributed between the electrons, the anitneutrinos and a negligible fraction to the daughter nucleus. Similar to a normal β-decay the resulting energy spectrum is therefore continuous.
In the $0\nu\beta\beta$-decay the energy of the decay is almost exclusively distributed to the electrons, resulting in a discrete line at $Q_{\beta\beta}$ at the very end of the $2\nu\beta\beta$ spectrum. This discrete line is the experimental signature many experiments are looking for. The $Q_{\beta\beta}$ of ^{76}Ge is 2039 keV.
Overall, the existence of a $0\nu\beta\beta$ would lead to the following conclusions:

- Neutrinos are massive particles.
- The neutrino must be a Majorana particle.
- The lepton number L is violated ($\Delta L = 2$).
- A discrete line at the Q-value $Q_{\beta\beta}$ of the decay would appear.

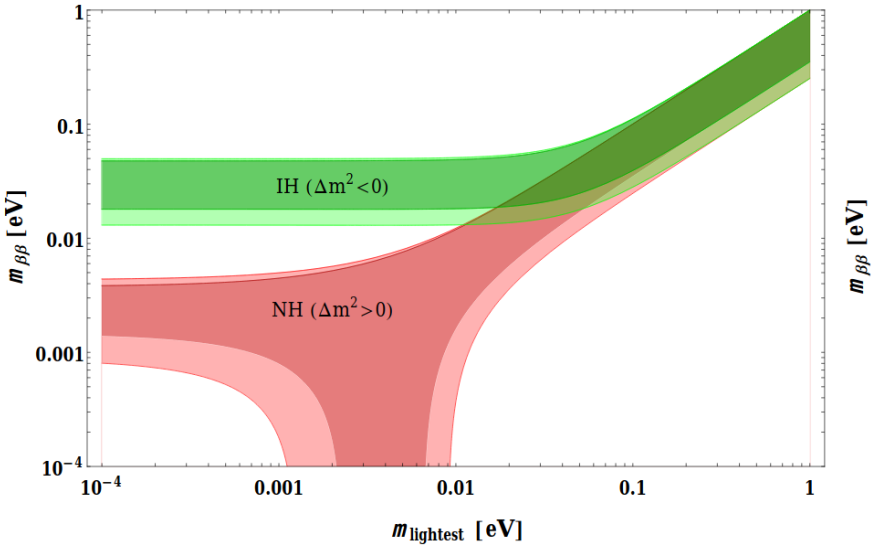

Figure 2.4: The effective neutrino mass $m_{\beta\beta}$ in dependence of the lightest mass eigenstate. The event rate of $0\nu\beta\beta$-decays is directly dependent on $m_{\beta\beta}$. Figure has been taken from [DMVV16].

The half-life of a potential $0\nu\beta\beta$ is orders of magnitude higher compared to the $2\nu\beta\beta$ and can be expressed as:

$$\left(T_{1/2}^{0\nu}\right)^{-1} = G^{0\nu}(Q(\beta\beta, Z)) \cdot |M^{0\nu}|^2 \frac{m_{\beta\beta}^2}{m_e^2}$$

Here, $G^{0\nu}(Q(\beta\beta, Z))$ is the phase space integral, $M^{0\nu}$ is the nuclear matrix element and $m_{\beta\beta}$ is the effective neutrino mass, which is a coherent sum of the ν_e mass eigenstates in dependency of the complex Majorana phases $\alpha_{1,2}$.

$$\begin{aligned} m_{\beta\beta} &= \left| \sum_i m_i U_{ei}^2 \right| \\ &= \left| m_1 |U_{e1}|^2 + m_2 |U_{e2}|^2 e^{i(\alpha_2 - \alpha_1)} + m_3 |U_{e3}|^2 e^{i(\alpha_1 + 2\delta)} \right| \end{aligned}$$

From this equation it becomes clear that the decay rate is dependent on both the absolute value of the neutrino mass eigenstates but also on the mass hierarchy.

If normal hierarchy (NH) is realized in nature, the biggest component of the flavor state ν_e is the smallest mass eigenstate m_1 and, depending on the Majorana phases $\alpha_{1,2}$, the effective mass $m_{\beta\beta}$ could become very small. In inverted ordering (IH), the biggest component of the flavor state would be heavy and $m_{\beta\beta}$ could not be canceled out.

3 GERDA and LEGEND

Among all possible isotopes, ^{76}Ge is a promising candidate for the detection of a $0\nu\beta\beta$-decay. High Purity Germanium (HPGe) detectors are well established and commercially available radiation detectors. Processes to enrich natural germanium with ^{76}Ge are very well established and an enrichment factor of more than 90 % can be achieved. This unifies the source and the detector which ensures a high quantum efficiency. HPGe detectors also provide an excellent energy resolution in the order of a few ‰, which, as it will be shown later, becomes very important for a possible signal discovery.

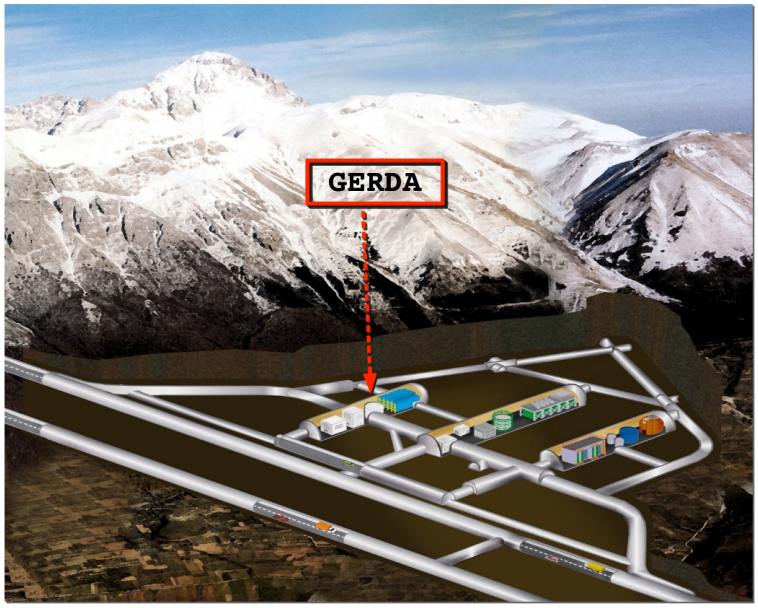

Figure 3.1: The LNGS site beneath the Gran Sasso mountain. The GERDA and LEGEND-200 site is located in Hall C.

The GERDA (GERmanium Detector Array) experiment made use of this technology and deployed around 40 kg of HPGe detectors in the Laboratori Nazionali del Gran Sasso (LNGS) beneath the Gran Sasso mountain in Italy. The GERDA Phase II started in December 2015 and ended its data taking in December 2019. A total exposure (lifetime times detector mass, $M \cdot T$) of 103.7 kg $\cdot$ y could be achieved but no $0\nu\beta\beta$ signal has been measured. The best fit favors a null signal strength and provides a lower limit for the half-life of [AAB+20]

$$T_{1/2} = 1.8 \cdot 10^{26}\,\text{yr at 90\% C.L.}$$

The Majorana Demonstrator (MJD) is another $0\nu\beta\beta$-decay experiment on ^{76}Ge operated by the MAJORANA collaboration [AAAI+19] at the Sanford Underground Research Facility (SURF), in South Dakota, USA. Details of this experiment will not be discussed in this work.

The successor of GERDA and MAJORANA is the LEGEND (Large Enriched Germanium Experiment for Neutrinoless $\beta\beta$ Decay) experiment. LEGEND is formed from the GERDA and MAJORANA collaborations and will start the operation of its first phase (LEGEND-200) presumably in 2021. LEGEND-200 will deploy up to 200 kg of HPGe detectors, also at the Gran Sasso laboratory, making use of existing GERDA infrastructure. The final goal of LEGEND (LEGEND-1000) is the operation of 1000 kg of HPGe detectors. GERDA and LEGEND have a similar baseline design and similar challenges to face. The goal of both experiments is to measure the $0\nu\beta\beta$-decay by counting events around the Q-value $Q_{\nu\beta\beta}$. If the $0\nu\beta\beta$ exists, an excess of events should appear. This decay has not been measured yet and its half-life must be larger than 10^{26} years. This means that even in the best case a measured signal would only contain a few counts.

In a background free environment the sensitivity to measure a decay with a given half-life scales directly with the exposure of the experiment

$$T_{1/2} = \epsilon \cdot \frac{\ln 2 \cdot f \cdot N_A \cdot}{m_A} \cdot \frac{M \cdot T}{N_S}.$$

The exposure is the active mass of the HPGe detectors times the lifetime of the detectors $M \cdot T$, ϵ is the signal efficiency, which is determined by the active volume of the detector, N_A the Avogadro number, m_A the atomic mass of ^{76}Ge, f is the enrichment fraction and N_S the total number of counts at $Q_{\nu\beta\beta}$. In the case that no background is present, every count at $Q_{\nu\beta\beta}$ is a signal count.

However, in a more realistic case with additional background the sensitivity only scales with

$$T_{1/2} = \epsilon \cdot \frac{\ln 2 \cdot f \cdot N_A \cdot}{m_A} \cdot \sqrt{\frac{M \cdot T}{BI \cdot \Delta E}}$$

Here the background index BI and the energy resolution ΔE decrease the sensitivity. Not every count at $Q_{\nu\beta\beta}$ is a signal count and in a Gaussian background regime the uncertainty on the number of counts scales with $\sqrt{N}$. An example of the influence of different background indices is depicted in figure 3.2. The success of a $0\nu\beta\beta$-decay experiment therefore crucially depends on both, the exposure and the background index. In the case of GERDA or LEGEND the increase in exposure can only advance slowly. HPGe detectors are not easily scaleable and the increase of the detector number and their operation also requires lots of time and a great logistic effort.

The background index can be reduced passively by the experimental design and the used materials and actively by additional veto systems and an offline background analysis. Therefore it is also important to understand the expected signature of a $0\nu\beta\beta$ signal. In a $0\nu\beta\beta$-decay, two electrons deposit energy of 2039 keV in only one detector. No additional particles are produced alongside and hence only one detector signal is expected (Detector Multiplicity = 1). If two or more detectors see an event simultaneously this event is counted as an external background event.

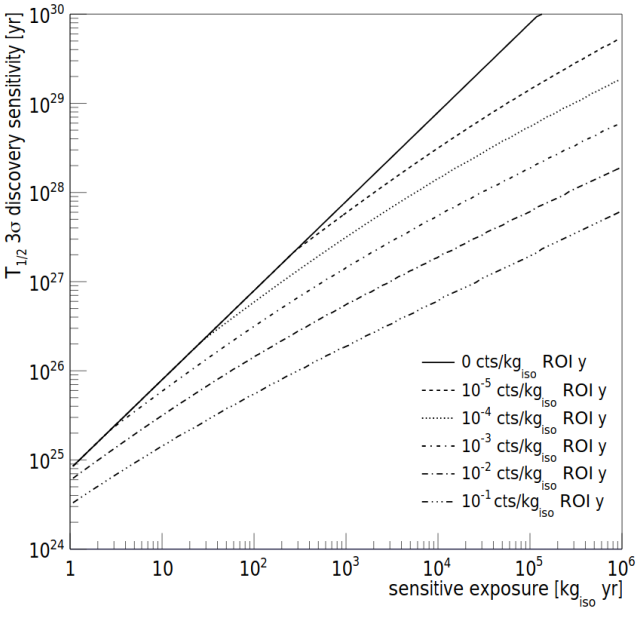

Figure 3.2: The increase in sensitivity to measure a $0\nu\beta\beta$ signal in dependence of the exposure for different background indices. In case of a zero background regime the sensitivity increase scales linear with the exposure. Figure taken from [ABD17]

External background can either be introduced by radioactive isotopes in materials close to the experiment or by cosmic background. The cosmic background is created by high energy muons which are created in the Earths atmosphere. These muons can hit the detectors themselves or create secondary particles in the surrounding volume. In order to reduce the external background, several background reduction techniques are installed.

Both GERDA and LEGEND-200 were and will be operated at LNGS which is located in the Abruzzo region in Italy. The rock overburden of around 1400 m provides an efficient shielding from cosmic and atmospheric background with a water equivalent of 3500 m. This reduces the measured muon flux at the laboratory site by a factor of around 10^{-6}, compared to the flux on the surface of the Earth. However, muons are still able to induce signals in the HPGe detectors. Therefore an active muon-veto system has been developed. This muon-veto consists of two parts, a plastic scintillator panel array on top of the experiment and a water Cherenkov detector which surrounds the whole experiment. The plastic

scintillator panels appeared to be redundant and will not be operated in LEGEND-200 anymore. The water muon-veto is a water filled tank with a diameter of 10 m and a height of 8.3 m in which up to 66 photomultiplier tubes are deployed. If a muon passes the water tank, Cherenkov light is being emitted and will be seen by the photomultipliers. If there is also a signal in at least one HPGe detector within 10 μs of the muon signal, the event is tagged as a muon induced event. The water also shields against external γ and neutron background.

The detectors are operated in a liquid argon (LAr) tank which is placed inside the water tank. The LAr provides both, a passive shielding against external radiation and an active background suppression since the LAr also scintillates when being exposed to radiation. Particles can produce light in the LAr which will be detected by Silicon Photomultipiliers (SiPM). Since the efficiency of the SiPMs is best for light with a wavelength of around 400 nm the wavelength of the emitted light (128 nm) needs to be shifted before the detection. This is done by wavelength shifting fibers which are placed like a curtain around the HPGe detector strings. If a γ deposits energy in the LAr and the HPGe at the same time, a LAr-tag is set and the event is discarded from the $0\nu\beta\beta$ analysis.

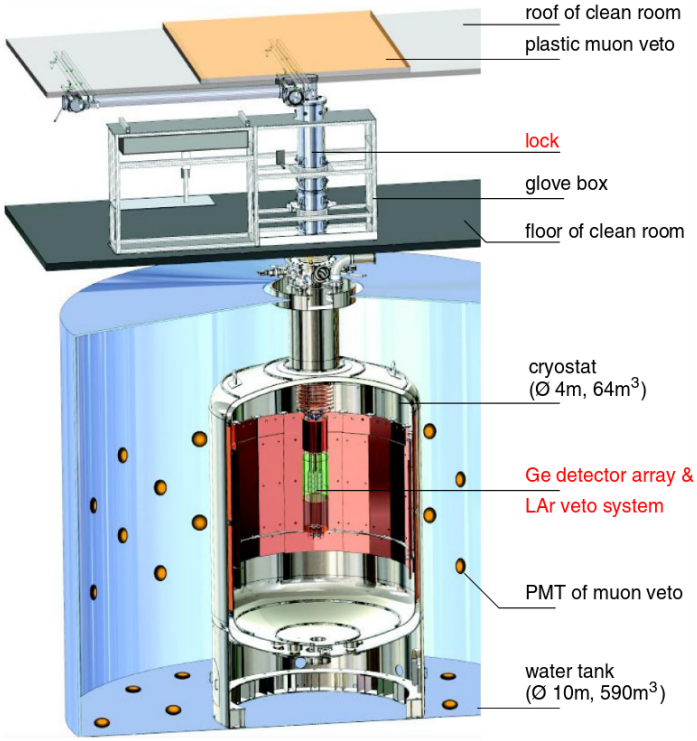

Figure 3.3: Drawing of the GERDA setup. The Detector arrays are placed inside the LAr cryostat which is again placed inside the water tank. Figure taken form [ABB+18]

Another method to classify background is the detector multiplicity cut. If an event occurs in more than one detector simultaneously, the event is classified as background. This can occur if a γ-particle Compton scatters in one of the detectors and additional deposits energy in another detector.

Other offline background reduction techniques make use of the pulse shape of the measured event and will be discussed later in chapter 5.3.

The sum of all background reduction strategies led to a total background index of of $5.2^{+1.6}_{-1.3} \cdot 10^{-4}$ counts/(keV kg yr) in the total lifetime of GERDA *Phase II* [AAB+20].
LEGEND-200 aims for a further background reduction below 10^{-4} counts/(keV kg yr). This reduction relies, among others, on the analysis and the detailed knowledge of the pulse shapes of background signals. Therefore, the mechanisms of energy deposition of particles in a HPGe detector as well as the signal formation inside a HPGe detector needs to be understood in great detail.

4 Germanium Detectors

This chapter will discuss the working principle of semiconducting detectors, such as the HPGe detectors that are used in GERDA and LEGEND, how signals are being created and what information can be gained from the signals. All signals are generated in the first place by an interaction of an ionizing particle with germanium atoms. Therefore, also the principles of the interaction of particles with matter will be described.

4.1 Interaction of particles with matter

All HPGe signals are generated by the production of electron-hole pairs due to radiation. Incoming particles interact on Ge-atoms and lift electrons from the valence band to the conducting band. These particles are mainly uncharged photons and charged particles like electrons and α-particles.

4.1.1 Interaction of photons with matter

When a photon travels through matter it has a probability to interact and to deposit its energy in different processes. These processes are mainly the photoelectric effect, the incoherent Compton scattering and the pair production. Which process becomes dominant depends on the energy of the photon.
The intensity I at a distance d of an initial γ-ray flux I_0 in matter can be expressed as a function of an attenuation coefficient μ:

$$I(d) = I_0 \cdot e^{-\mu\rho d},$$

Where μ is the sum of the single attenuation coefficients of each process $\mu = \mu_{PE} + \mu_C + \mu_{PP}$. The different attenuation coefficients for germanium are shown in figure 4.1. At low energies ($E < 200\,\text{keV}$) the photoelectric effect dominates the energy loss. In the medium energy range below 10 MeV, the energy transfer happens mainly via Compton scattering until the pair production becomes the dominant process.

- **The photoelectric effect :** In the photoelectric effect an incoming photon transfers all of its energy E_γ to a shell electron. The electron is being ejected with the energy of the initial γ reduced by the energy of the atomic shell from which the electron was ejected.

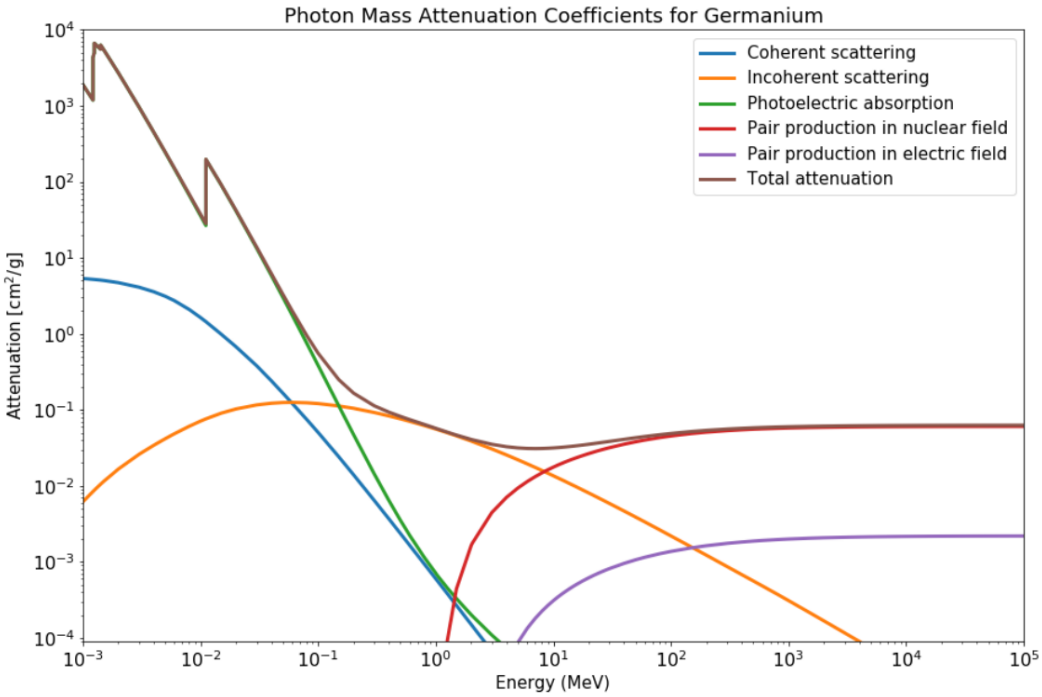

Figure 4.1: Attenuation coefficients for germanium in dependence of the energy. At low energies the total attenuation μ is dominated by the photoelectric effect. The Compton scattering dominates at medium energies until the pair production becomes the dominant effect. Figure taken from [Sch18]

The remaining shell vacancy will be refilled by higher shell electrons under the emission of X-ray photons.

- **Compton scattering :** In the inelastic, incoherent Compton scattering an incoming γ only partially transfers its energy to a free or outer shell electron. After the scattering process, the γ moves on with a reduced energy and a different direction of motion. The amount of transferred energy depends on the scattering angle Θ (i.e. the angle between the incoming γ and the outgoing γ) and is highest for a 180° scattering:

$$E_{trans}(E_\gamma, \Theta) = E_\gamma \left(1 - \frac{1}{1 + \frac{(1-cos\Theta)E_\gamma}{m_e c}}\right)$$

The maximum transferable energy $E_{max}(E, 180°)$ creates the characteristic Compton edge in the energy spectrum.

- **Pair production :** For the pair production the incoming γ must have at least an energy above 1022 keV, since an electron-positron pair with single masses of 511 keV is created.

This process needs an external magnetic field and therefore happens mainly close to the nucleus of a target atom. The created e^- and e^+ share the total energy of the γ minus the 1022 keV needed for the pair production. The electron deposits its energy in a close vicinity of its creation point. The positron almost immediately annihilates under the emission of two γ particles with 511 keV. These γ can again deposit their energy in the detector or one or both can escape the detector without any further interaction. This lead to the characteristic structures of the so-called double escape peak (both γ escaping the detector, DEP), and single escape peak (only one γ escaping the detector, SEP). More details on the DEP and SEP will be given later.

4.1.2 α particles

Radioactive α decays are one of the biggest backgrounds within the GERDA experiment. α particles are ionized ^{4}He nuclei, making them massive and charged by two positive elemental charges.

α particles primarily interact with matter through Coulomb interactions. Therefore the attenuation length and the energy loss per distance of the α particles is highly dependent on the absorbing material.

For high α energies above a few hundreds of keV the energy loss per distance can be described by the Bethe formula:

$$-\frac{dE}{dx} = \frac{4\pi n Z^2}{m_e c^2 \beta^2} \cdot \left(\frac{e^2}{4\pi\epsilon_0}\right)^2 \cdot \left[\ln\left(\frac{2m_e c^2 \beta^2}{I(1-\beta^2)}\right) - \beta^2\right]. \tag{1}$$

In germanium the attenuation length of αs with energies of a few MeV is in the order of $\sim 20\,\mu m$

4.1.3 Beta particles

Electrons can interact with matter via ionization or via bremsstrahlung. The incoming electron can scatter on a shell electron and transmit a fraction or all of its energy. The bremsstrahlung occurs when a charged particle changes its momentum caused by an external electromagnetic field. The Bremsstrahlung is a photon that can carry continuous amounts of energy up to the total initial energy. The fraction of energy loss due to bremsstrahlung is also dependent on the electron energy and the proton number of the target material.

All of the described processes produce electron-hole pairs in a semiconducting germanium

detector. This detector type is well established and its working principle will be described in the following. An extensive description of general radiation detection techniques can be found in [Kno10] and on germanium detectors in [Amm18].

4.2 Semiconductor detectors

Solid state materials have two different energy bands which can be populated by electrons. These bands are the lower valence band and the higher conducting band. In the valence band the electrons are locally bound to a specific lattice site and are not able to move through the material. In the conduction band the electrons are not bound locally and can move freely through the material. The energy gap between those bands and the occupation of the bands determine the conducting properties, i.e. if the material is an insulator, a conductor or a semiconductor. The bands of an insulator are widely separated ($E_{gap} = \mathcal{O}(10\,\mathrm{eV})$) and the conduction band is not populated by electrons. Thermal excitation is not enough to lift electrons from the valence band into the conducting band and hence no electric current can flow. In an conductor the conducting band is partially populated by electrons which can move around and therefore create the electrical conductivity.

A semiconductor is similar to an insulator only with the difference that the band gap is comparably small ($E_{gap} < \mathcal{O}(1\,\mathrm{eV})$) and thus can be overcome only by thermal excitation. In absence of thermal excitation a semiconductor would also behave like an insulator. Therefore, in order to minimize thermal excitation, semiconductor detectors are cooled while in operation.

Germanium is a semiconductor with an energy gap of $E_{gap} = 0.67\,\mathrm{eV}$. When ionizing radiation interacts with the germanium, a high number of electrons is lifted from the valence band to the conducting band leaving vacancies in the valence band, which can be pictured as positively charged holes. The number of electron-hole pairs which are created is directly proportional to the transferred energy of the radiation $n_{e^-,h} = {}^{E_{trans}}/_{\epsilon}$, with ϵ as the energy that is needed to create one electron-hole pair ($\epsilon = 2.96\,\mathrm{eV}$ at $77\,\mathrm{K}$ for germanium). Since the creation of the charge carrier pairs is of statistical nature the uncertainty of the produced number would follow Poisson statistics $\Delta n_{e^-,h} = \sqrt{n_{e^-,h}}$. However, additional phonon excitation accompany the creation of the charge carriers, making the creation process not independent anymore. The difference between the ideal fluctuation and the actual fluctuation can be expressed as the Fano factor. The Fano factor directly influences the energy resolution and should be preferably small.

4.2.1 High purity germanium detectors

An intrinsic semiconductor is purely made out of one element. In reality every material contains at least a small amount of impurities. These impurities can introduce additional electrons or holes (depending of the number of valence electrons of the impurity atom) which lead to net conductivity. Germanium is a member of the group IV of the periodic table, i.e. it has four valence electrons which are part of the covalent bonding in the lattice. If group III atoms are added (doped) into the solid state material, one electron is "missing" in the bonding. Therefore, a net positive hole is introduced into the valence band. This type of doping is called p-type doping. Contrary a doping with group V atoms introduce additional electrons and is called n-type doping. In the case of a heavy doping a "+" is added to the nomenclature, i.e. a heavy p-type doping is called "p+" and a heavy n-type doping is called "n+". These heavily doped materials can be considered conductors and are often used to form the electrodes of the detectors.

When p-type and n-type doped semiconductors are brought together they form a pn-junction. Charge carriers can migrate along the junction such that the electrons from the n-type diffuse into the p-type and the holes from the p-type diffuse into the n-type. This leaves a net space charge at both regions which prevents a further drift of charge carriers. This region is called the depletion region. The effect can be enhanced if a positive voltage is applied on the n-side of the junction. This is called reversed bias and enhances the depletion region. In this case no current flows and the junction is in a steady state. If now particles create electron-hole pairs in the depleted region the electrons will migrate towards the n-region and the holes will migrate towards the p-region creating a net current. This current can be measured and the total amount of created charges is proportional to the deposited energy.

It is favorable to create a large depletion region for the operation of a radiation detector. In a one dimensional pn-junction the depletion region width d can be expressed in terms of the applied voltage $d \approxeq \sqrt{\frac{2\epsilon V}{eN}}$, where N is the dopant concentration. It becomes clear that for a large depletion region a high voltage is needed. For HPGe detectors the applied voltage is in the order of a few kV.

The heavily doped n+ (usually lithium diffused) and p+ (usually boron implanted) contacts are blocking electrodes, preventing the induction of electrons (holes) on the respective contacts and therefore a steady current. These two contacts are on the outer surface of the detector and have to be physically separated from each other. This is usually done via a passivated

inter-layer (PL). This PL consists usually of a few monolayers of amorphous Ge or Si. As it will be shown in this work, the charge collection properties and therefore the signal creation in close vicinity of this PL are different to a normal bulk signal of a HPGe detector, and the pulse shapes can be heavily distorted.

4.2.2 HPGe detector geometries

There are a lot of possibilities to define the geometry of a HPGe detector. All designs have different advantages an disadvantages. In the following, four different detector designs will be presented, that have been used in GERDA or the MJD or will be used in LEGEND.

The Semi-coaxial Germanium detector (COAX): The COAX detector is a Ge-crystal with a borehole on one detector side. This detector type is rather big with masses around 2 kg. The borehole does not reach through the whole detector and hence it is named a semi-coaxial detector type.

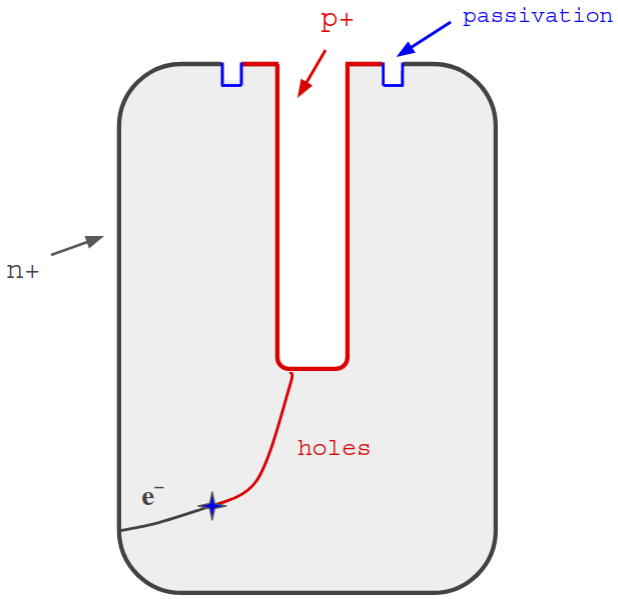

Figure 4.2: The geometry of a semi-coaxial detector design.

The outer surface of the detector is the Lithium diffused n+ contact on which the high voltage is applied. The surface of the borehole is the Boron implanted p+ contact on which the induced signal will be read out. Both surfaces are separated by a passivated surface called the groove.

This detector type has the advantage that it can be made out of a relatively large and therefore massive Ge-crystal. The borehole enables a depletion with large detectors since the distance from n+ to p+ stays the same along the vertical axis of the detector. Figure 4.2 shows a sketch of the detector geometry. When radiation creates electron-hole pairs, the elec-

tron drifts towards the n+ and the hole drift towards the p+ contact.
As it will be described later, the disadvantage compared to the other three detector types is that the COAX does not allow for a good pulse shape discrimination. This detector type has been used in GERDA but will not be further used in the future $0\nu\beta\beta$ experiments.

The Broad Energy germanium detector (BEGe) and the Point Contact detector (PPC): The BEGe and the PPC detectors have a similar design. Both are small compared to the COAX type, with masses usually below 1 kg, but enable a good pulse shape discrimination and an excellent energy resolution. Both detectors are small cylinders with a small p+ contact on the bottom of the detector (see figure 4.3). The small p+ contact leads to a small capacitance and hence an excellent energy resolution can be achieved. The main difference of the two detector types lies in the separation of the two contacts from each other. The BEGe has a passivated groove similar to the COAX while the PPC has no groove and its total bottom side is covered by a passivation layer. This passivation layer is vulnerable to α particle penetration and, as PPC detectors have a bigger PL, they are more affected.
The BEGe detectors have been used in GERDA whereas the PPC detectors have been used in the MJD. Both types will be further used in LEGEND-200.

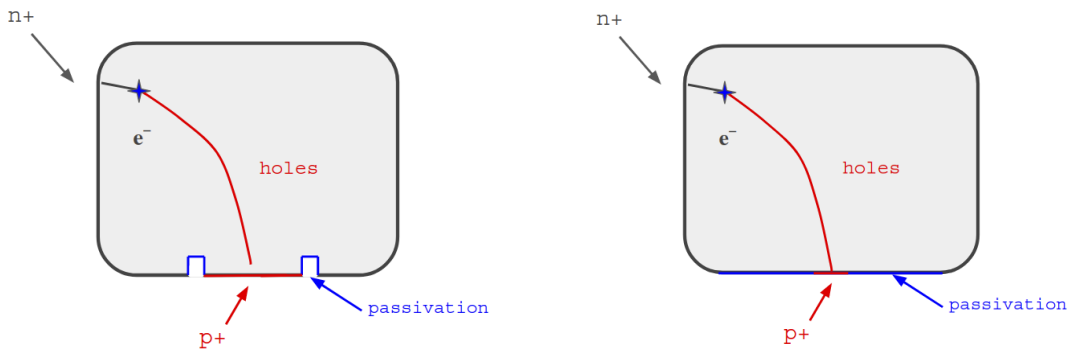

Figure 4.3: The BEGe and the PPC geometry. The main difference is the separation of the two contacts.

The Inverted Coaxial germanium detector (IC): IC detectors are a mixture of a COAX and a BEGe detector. It has the geometry of a COAX detector, with masses that can also be above 2 kg, but the small p+ contact of the BEGe. Most of the surface, also the surface of the borehole, is the n+ contact. IC detectors have the advantage of the large scale and the big mass but still provide a very good energy resolution and enable pulse shape discrimination.

These detectors are the baseline design for the future $0\nu\beta\beta$-decay searches with germanium. Within the IC design there are also two possibilities to manufacture the p+ contact area (see figure 4.4). In one design the p+ contact covers the total area within in the groove. This IC-type has been operated in the last phase of GERDA [coled]. In the other design, the passivated layer extends from the groove further to the detector center, and only a small area is used as the p+ contact. This detector type has therefore a much bigger PL compared to the other and will be called ICPC (Inverted Coaxial Point Contact). As it will be shown in this work, the detector response to α interaction on the PL is different to interactions on the p+ contact. Therefore the difference in design has an impact on the pulse shape analysis.

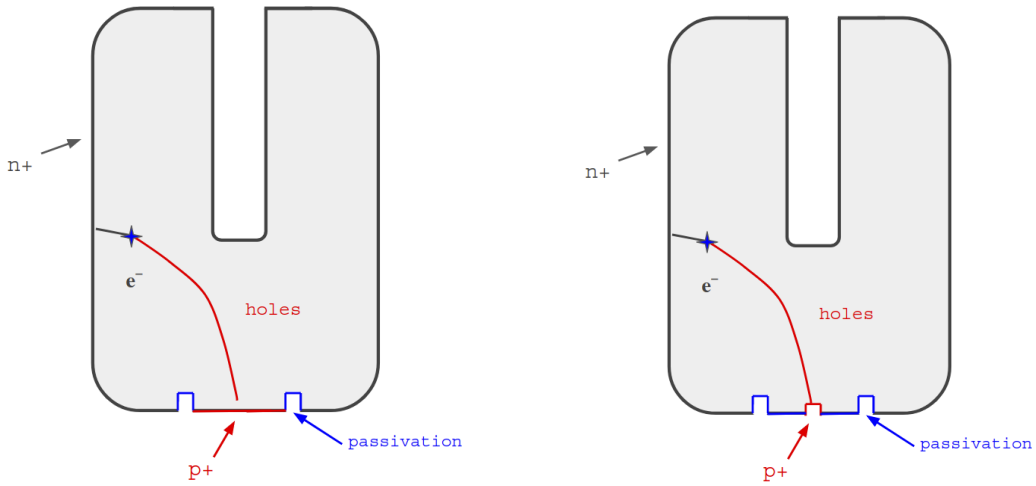

Figure 4.4: Two different ICPC designs. On the left, the p+ covers the total area within the groove whereas on the right, an additional passivated layer is implemented.

4.2.3 The Shockley-Ramo theorem

The pulse shape discrimination plays a crucial role in the success of a $0\nu\beta\beta$ experiment and therefore the mechanisms of the signal formation inside a HPGe detector will be discussed in the following.

The signals of a HPGe detector are formed by charge carriers which move inside the electric field of the detector. The signals are not created when the charge carriers arrive at the electrodes, but rather the movement of the charge carriers itself induces mirror charges and mirror currents in the electrodes. In the late 1930's Shockley and Ramo [Sho38] [Ram39] independently introduced a method to calculate the induced signal by the motion of a charge inside an electric field.

When a particle interacts inside the detector, electron-hole pairs are being created and will start migrating through the detector along the electric field lines. A full calculation of an induced charge at the read out electrode could be solved by integrating the normal component of the instantaneous electric field $\vec{E}$ for each step of the trajectory of the charge q over the surface S that surrounds the electrode:

$$Q = \oint_S \epsilon \vec{E}(\vec{x}) \cdot d\vec{S}.$$

Shockley and Ramo showed that the charge at the electrodes, which is induced by the moving charge q, is independent of the applied potentials on the electrodes as well as of the space charge density ρ inside the detector. It is sufficient to calculate a so called weighting potential ϕ_0 (or weighting field $\vec{E_0} = -\text{grad}\phi_0$) once. The weighting potential is the electric potential that would exist if one electrode was set to unity and the other electrode to 0 and no space charges were present. Then the induced charge at the electrode is simply given by the charge $-q$ times the weighting potential at the position of the charge:

$$Q = -q \cdot \phi_0(\vec{x}).$$

The induced current is determined similar by the weighting field:

$$I = -q \cdot \vec{v} \cdot E_0(\vec{x}),$$

with $\vec{v}$ as the velocity of the charge q.
This means that for the signal calculation only the once calculated weighting potential and the trajectory of the charges are needed. The charges follow the electric field lines, i.e the trajectory is determined by the electric potential inside the detector. In order to determine the trajectory, the electric field inside the detector also needs to be calculated. This field is slightly different from the weighting field and it can be calculated with the Poisson equation:

$$\nabla^2 \phi_E = \frac{-\rho}{\epsilon}.$$

The boundary condition is given by the applied voltage V of the detector. The electric potential is the weighting potential scaled by the applied voltage and under the influence of space charges ρ. These space charges are given by the impurities and influence the electric field and especially

the depletion voltage of the detector. In most cases the impurity concentration can be described by a linear gradient between the top and the bottom of the detector crystal.

The electric field is then given by $E = -\text{grad}\,\phi(\vec{x})$. The charge carriers will follow the electric field lines, which is the direction of the maximum gradient of the potential. Also their drift velocities depend on the electric field. The velocity of the charge carriers is given by the mobility μ time the electric field at the position $\vec{x}$.

$$\vec{v} = \mu \cdot \vec{E}(\vec{x})$$

With the electric field and the weighting field, the induced signal can be calculated for all common detector designs.

4.3 Pulse shapes of HPGe detectors

As already mentioned, the pulse shapes of the HPGe signals play a crucial role in the background rejection and therefore in the success of $0\nu\beta\beta$ experiments. The expected signature of a $0\nu\beta\beta$-decay is the simultaneous emission of two electrons which deposit their energy immediately in a very local area (within 1 mm^3 of the decay site). This type of signal is called a single site event (SSE). The measured signal is created by the movement of the created charges inside the weighting field of the detector. When a charge moves through areas of a high weighting field, high mirror currents are induced. This means that the strength of the measured current can provide information on the trajectory of the charge inside the detector. In a BEGe, PPC or ICPC detector, the weighting field is highly inhomogeneous

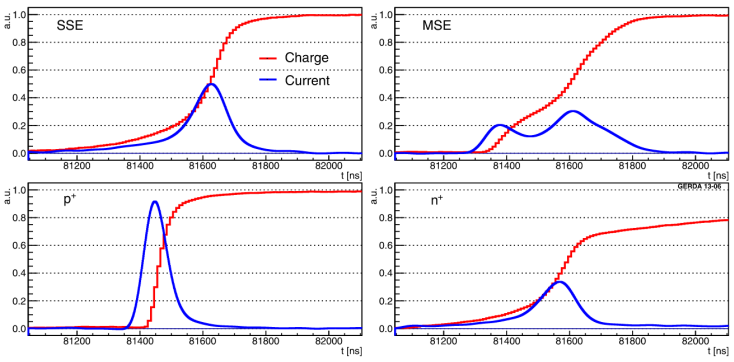

Figure 4.5: An example of different pulse shapes. The induced charge is shown in red and the current in blue. The top panels show the difference between a SSE and a MSE event. The bottom panels show difference between a SSE close to the p+ and a SSE far away. Figure is taken from [AAA+13].

and highest close to the p+ contact. This means that events close to the p+ create a fast rising charge pulse with a high maximum current. Events far away (i.e. close to the n+) create a slowly rising charge pulse with a lower maximum current. The weighting potential of COAX detector has a much lower gradient, i.e. its weighting field is much more homogeneous. This leads to bigger areas in the detector in which the signal is formed, and hence, a pulse shape analysis becomes difficult.

Contrary to intrinsic β-decays, external γ particles can deposit their energy in more than one location. It could for example Compton scatter at one location and undergo a photoelectric effect at another location within the detector. The resulting signal would be a superposition of the two signals with respective maximum currents at slightly different times. These events are called multi site events (MSE). A schematic overview of the difference between the charge and current signals of a SSE and MSE is shown in figure 4.5. In this example, both deposited energies are equal, i.e. the total collected charge is the same. However the maximum current of the SSE is higher since only one event creates the signal. The current of the MSE is separated into two parts making the maximum current lower.

The A/E is the parameter that is received when dividing the maximum current A by the total energy E. This parameter can be used as a pulse shape discriminator between background and SSE events. More details on its calculation and calibration will be given later.

In reality, more effects play a role in the signal formation. When a particle interacts with the Ge atoms, a large number of electron-hole pairs is created and form a charge cloud. When this charge cloud migrates through the detector, its constituents diffuse and the charge cloud size can increase. Also self repulsion effects can play a role as well as the lattice orientation of the Ge-crystal influences the transportation properties. These effects can play a role especially for surface events.

In order to read out the HPGe detector, a dedicated electronic read out system must be implemented. Such a system usually consists of a charge sensitive preamplifier (CSA) that transforms a charge into an amplified voltage signal. The CSA consists typically of a Junction Field-Effect Transistor (JFET) and an amplifier. This CSA is coupled to a RC feedback loop. The capacitor of this RC loop collects the induced charges which creates the rising edge of the voltage pulse until all charges are collected. The parallel connected resistance R restores the voltage to its baseline level.

The resulting voltage signal therefore decays exponentially, whereas its decay constant τ is given by the capacitance times resistance, $\tau = RC$.

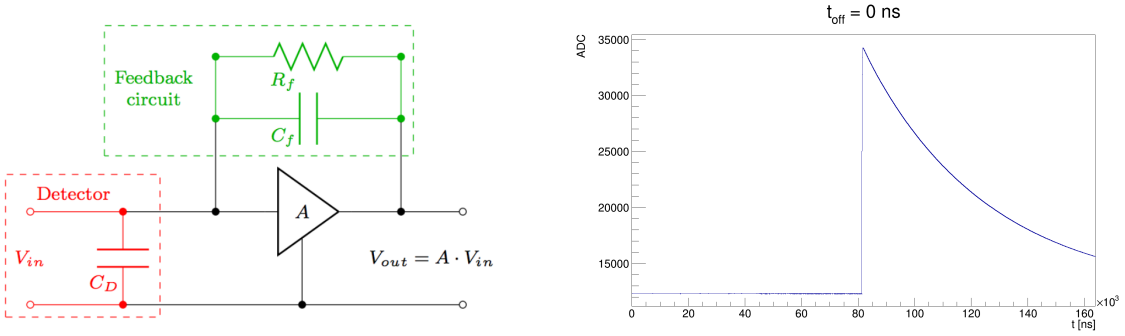

(a) A simplified diagram showing the read out scheme. The RC feedback loop in green integrates the charge and restores the voltage back to its baseline. Figure taken from [Leh15].

(b) An example voltage pulse. The decay of the pulse is determined by the RC feedback loop.

Figure 4.6: The influence of a RC feedback loop.

A diagram of a simplified readout scheme and a resulting voltage signal is shown in figure 4.6. Generally the decay of the signal should be independent of the physics of the signal formation inside the detector. However, as it will be shown in this work, the decay time of a voltage signal can be drastically increased if α particles interact close to the passivated surface of an ICPC detector. In this case, parts of the charges which create the signal are slowed down such that the overall decay time enhances. This effect will be discussed later.

The pulse shape of a HPGe detector signal contains a lot of information on the type of the event and on the event location inside the detector. A detector that is used for $0\nu\beta\beta$ searches needs to have these pulse shape discrimination capabilities while also providing an excellent energy resolution. The ORTEC company builds ICPC detectors that ideally should fulfill all the requirements. In the following the results of an extensive scan of such an ORTEC ICPC detector will be presented.

5 The ORTEC Detector

The LEGEND collaboration decided to take the new Inverted Coaxial detector design as the lead design for the upcoming procurement of Germanium detectors. Several vendors are able to produce detectors that possibly fulfill the high required needs for a large scale $0\nu\beta\beta$ experiment like LEGEND. LEGEND decided to acquire detectors from the two major companies, MIRION and ORTEC. MIRION detectors are already in use in the GERDA experiment in a variety of different designs. The newest Inverted Coaxial detectors, IC-detectors, have been tested and deployed in GERDA in 2018 [coled], and first experiences, in vacuum test stands as well as in full GERDA operation in liquid Argon, could already be gained. ORTEC manufactures IC-detectors with a smaller p+ contact but a bigger PL. The experience with ORTEC Inverted Coaxial detectors however is limited, as GERDA only deploys MIRION IC detectors and only ORTEC Point Contact (PPC) detectors are installed in the Majorana Demonstrator. These PPC detectors have a small read out contact, which is separated from the high voltage contact by a wide passivation layer. [AAIB+20] and [Gru17] showed that α events, which interact in the vicinity of this PL, show a degradation in energy and an altered PSD performance and can introduce a non vanishing source of background.
In comparison to these PPC detectors, the IC-detectors have less passivated surfaces and therefore a lower event rate on the PL. Nevertheless α particles can also enter this surface and introduce background.

One of those ORTEC ICPC type detector has been purchased in 2017 and have been measured extensively over the last years. The goal of the studies presented in this text is to analyze the general performance of the new ICPC type detectors and more important to investigate and analyze the PL surface events and the possibility to identify them. In the following, an overview of the detector itself and of all data taking campaigns will be given. After that, the routines which were developed and applied on the data are explained in detail and the obtained results will be shown at the end of this section.

5.1 Detector geometry and properties

In the following the studied ORTEC ICPC detector will be introduced. The dimensions of this detector will be discussed, whereas the dimensions of the passivation Layer is of special interest. The bottom of the detector is divided into four parts. The p+ contact with a diameter

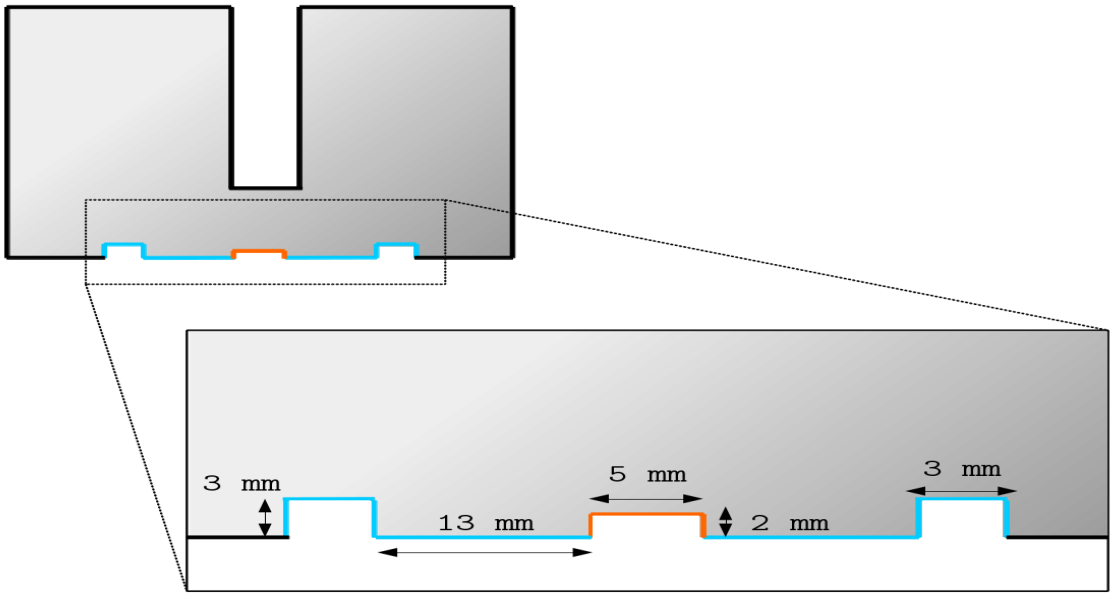

Figure 5.1: Sketch of the ICPC detector and a zoom into the region around the p+ contact. The purpose of this sketch is to provide an overview of the p+ region. The p+ contact is drawn in orange and the passivated surface is drawn in blue.

of 5 mm, the Groove with an inner radius of 13 mm and an outer radius of 16 mm, the region between p+ and groove and the outermost n+ contact. All the area between the end of the p+ contact at 2.5 mm radius to the end of the groove at 16 mm radius is covered by the PL. That gives a total passivated area of 785 mm^2 making up for around 3 % of the total detector surface. Figure 5.1 shows a sketch of the detector bottom up and most important values are listed in table 1.

5.2 Overview of the data taking campaigns

In total, three different measurement setups have been employed in order to characterize this ORTEC ICPC detector and to study its response to α surface events. This section gives an overview of all activities related to this detector and sets the chronological timescale of all data takings.

5.2.1 General scans

The first performance evaluation was done in late 2017 at the Max-Planck-Institute in Heidelberg. The goal of this data taking was to determine general properties of the detector, like the

Dimensions	
Height	67 [mm]
Diameter	76 [mm]
p+ Diameter	5 [mm]
Inner/Outer Groove Diameter	26/32 [mm]
Bore Hole Diameter	10 [mm]
Bore Hole Height	39 [mm]
n+ Thickness	1.5 [mm]
n+ Thickness Bottom	0.7 [mm]
Depletion	3200 [V]

Table 1: Overview of the most important geometry parameters of the investigated ORTEC ICPC.

depletion voltage, the energy resolution, the surface homogeneity and the pulse shape discrimination performance. This has been done on several runs with different radioactive sources at different positions. The detector has been deployed in a vacuum cryostat and was read out was by a Struck FADC. Several source types and source positions have been used for different scans.

An overview of all measurement types is shown in table 2.

Purpose	**Source Type**	**Collimation**
Depletion Voltage	^{60}Co	no
Energy resolution	^{228}Th	no
Pulse shape performance	^{228}Th	no

Table 2: Overview of the analyzed measurement types and used sources for the standard characterization.

5.2.2 Test in liquid Argon in GDL

After the first general scans, the detector has been brought to the Gran Sasso laboratory and was deployed there in the GERDA detector laboratory (GDL), in which a HPGe detector can be operated in liquid Argon.

One goal of this campaign was to measure the pulse shape performance with a ^{228}Th source

in LAr. Another purpose of this measurement was the observation of a the leakage current in LAr with and without radioactive sources irradiating the detector. Earlier studies on BEGe detectors [HBGS10] showed that especially the passivated layer of a HPGe detector could be a source of an increasing leakage current when irradiated in LAr.
Finaly the detector was immersed in liquid Nitrogen (LN_2) in order to test the temperature dependent charge collection and transportation properties. LN_2 with a temperature of 77 K is 10° colder than LAr, hence the temperature dependence of the charge collection properties could be tested.
Unfortunately this measurement failed due to a too high leakage current of the detector while being immersed in LN_2. So far this temperature dependence has not been tested yet.
The results of the GDL campaign will be presented in section 5.7

5.2.3 The TUBE setup

Apart from the general performance, the response of the detector to surface events is of great interest. This special measurements have been performed with the TUBE setup which is located at TU Munich. This setup has been used on two other detectors before. The first campaign has been done in 2013 in order to scan the passivated groove of an MIRION (former CANBARRA) BEGe. As shown in [Ago13], MIRION BEGe detectors showed a degradation of the measured energy of events originating in this PL. Also the pulse shapes of those events were affected but it could be shown that the A/E PSD efficiently removes these event types.
In 2016 the MAJORANA collaboration used the TUBE setup to investigate the α surface events on ORTEC PPC detectors. Since the PPC detectors have a larger passivated surface, these detectors are more vulnerable to these event types.
Prior to this thesis, the investigation of PL response to α particles has not been done on the ICPC detector type. Within this work, the results of this data taking campaign will be presented. As it could be seen for the PPC detector, the measured energy degrades drastically for the α PL events. However, this degradation is complementary to the observation made with the ORTEC PPC detector. The ICPC scan shows a decrease of the energy with an increasing distance to the p+ contact (the farther away the interaction point from the p+, the smaller the measured energy). The PPC scan showed an increase of energy with a increasing distance to the p+ (the farther away the interaction point from the p+, the higher the measured energy). Furthermore, an increase of the decay time of the charge pulse, also in dependence

of the incident radius, could be observed. This effect is named the Delayed Charge Recovery (DCR) and can be measured by a DCR parameter. Details on the performed scan can be found in [Gru17] and [AAIB+20] and more details on the DCR will be given in section 5.4. Details on the analysis will be presented later in chapter 6.

With the ICPC detector and the TUBE setup 17 measurements on 14 different positions have been performed. The collimator with the ^{241}Am source is mounted on a rail with a 66° horizontal angle. This leads to a ellipsoidal illuminated spot on the detector surface with a long diameter of ca. 3.8 mm. The read-out pin at the center of the detector is mounted to a PTFE-bar and is partially blocking the α particles when the collimator passes the detector center. This shadowing effect can be seen in the data. Figure 5.2 shows a schematic view of selected source positions and its illuminated area on the detector surface. This figure does not show the dimension in correct proportions. It should be used just to visualize the direction of the incoming α particles and the shadowing effect around the p+ contact due to the PTFE-bar holder of the read out pin.

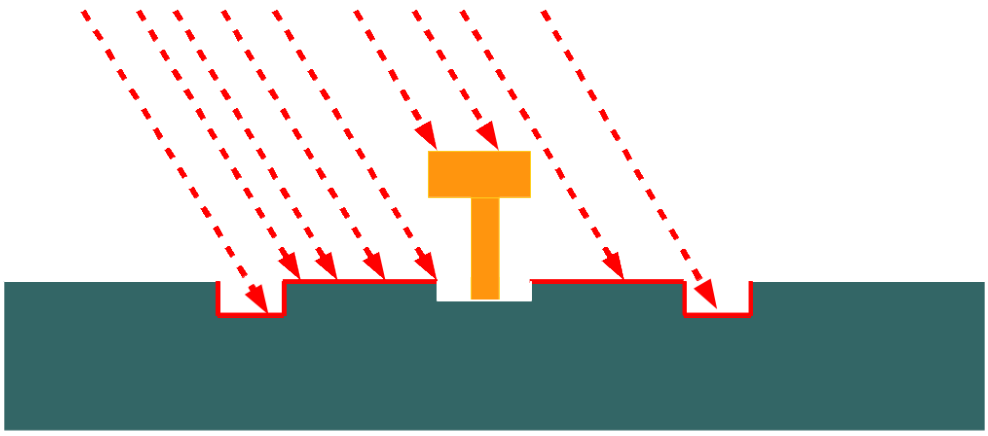

1

Figure 5.2: A sketch of the detector surface. The detector is mounted bottom up inside the TUBE setup and collimated α particles irradiate the surface with an angle of 66°.

During each run the data has been recorded and stored to a local hard-drive. Afterwards the

data has been transmitted to the Max-Planck servers in Heidelberg. All further data processing and data analysis has been performed there. For the transformation of the binary data and the application of digital filters on the recorded waveforms the standard GERDA software GELATIO has been used. Details on the digital signal processing (DSP) and the algorithms and routines which were used for the data analysis are the topic of the following section.

The realization of the data taking at all three scanning setups would not have been possible without the help of colleagues. The work of Yoann Kermaidic shall be acknowledged, who helped setting up and deploying all three setups, and performed most of the measurements at the Heidelberg test setup. Konstantin Gusev mounted the detector into the GDL and TUBE setup and Tommaso Comellato helped with the implementation and the data taking with the TUBE campaign.
The analysis that is presented in this work has been done by the author of this thesis, including the data transformation, the application of the different calibration and analysis routines as well as the development and application of pulse shape parameters and the construction and evaluation of a cut procedure based on the developed PSD parameters. Also the application and evaluation of the Monte Carlo and pulse shape simulations have been performed in this work.

5.3 Data flow and Analysis routines

In all of the three measurement setups the data has been digitized with a Flash Analogue to Digital Converter (FADC). The transformation of the raw, digitized data towards a full analysis involves several different steps at different analysis levels. This section will describe how the data has been prepared and how the data has been selected, what digital signal processing (DSP) modules have been applied in order to generate the parameters of interest and what calibration methods has been applied to scale those parameters. All data which has been taken with this ORTEC detector has been transformed following this analysis flow.

The data is structured into so called tier levels, whereas each level represent a different stage in in the analysis flow and holds different information. Dedicated DSP routines transform the data from one level to another. Overall four analysis levels are used in this work.

- raw level - the raw binary output of the FADC,

- tier1 level - the human readable conversion of the raw data into so called waveforms,
- tier2 level - the output of digital signal processing modules (Energy, Current amplitude, etc.),
- tier3 level - Calibrated data and higher level pulse shape parameters parameters (e.g. A/E, DCR).

In the following, the single transformation steps between the tier levels will be introduced.

5.3.1 Data preparation

At the very beginning, at each measurement, all the raw data is stored in binary format on a local hard drive. Afterwards all data from all setups has been moved to the Max-Planck computing cluster in Heidelberg and all further analysis has been carried on this system.
For this purpose, the raw binary data needs to be transformed into a data format that can be opened and processed by higher level analysis software. The Root software [BRP+03] was chosen for this work, since it is explicitly designed for data analysis and additional GERDA software has been developed and embedded in the Root environment.
One of those additional programs is the software GELATIO which was developed within the GERDA collaboration and which serves two purposes. First it is used to transform the binary data into a "rootified" data set (i.e. into a format that can be opened and processed by Root). After that several DSP modules can be applied by so called GELATIO modules. Further details on the GELATIO software can be found here [APZ12].
GELATIO converts the binary data into an event level structure such that each trigger from the Germanium detector represents an event. This event level structure is the tier1 level. On this level, each event carries the two recorded waveforms (the low frequency and the high frequency waveform) which are associated with the event. These waveforms can be pictured as arrays whose elements represent the amount of charge at the i'th digitized sample of an recorded pulse. An example waveform (low frequency and high frequency of the same event) is shown in figure 5.3. These waveforms serve now as the input for the DSP modules of the GELATIO software. The output of those modules give the parameters of interest like the energy, the rise time of the waveform, the maximum current amplitude and many others as single floating point values and is stored in a new tier2 level file. Details on the most important modules will be discussed in the following.

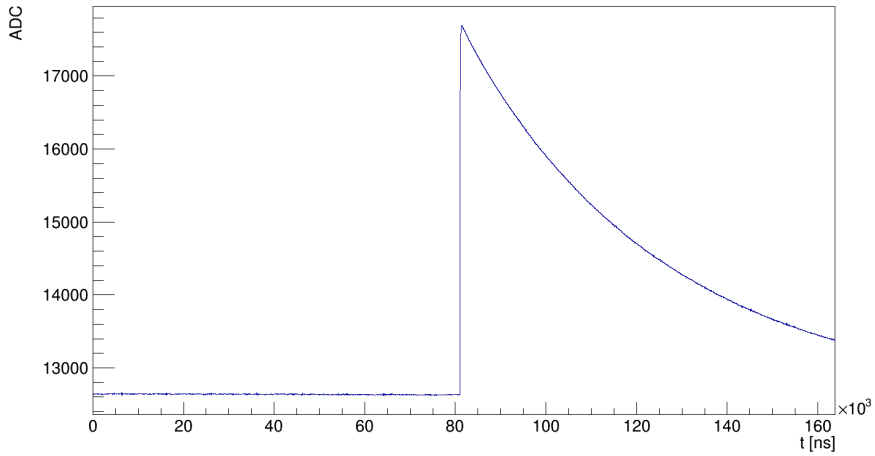

Figure 5.3: The low frequency trace.

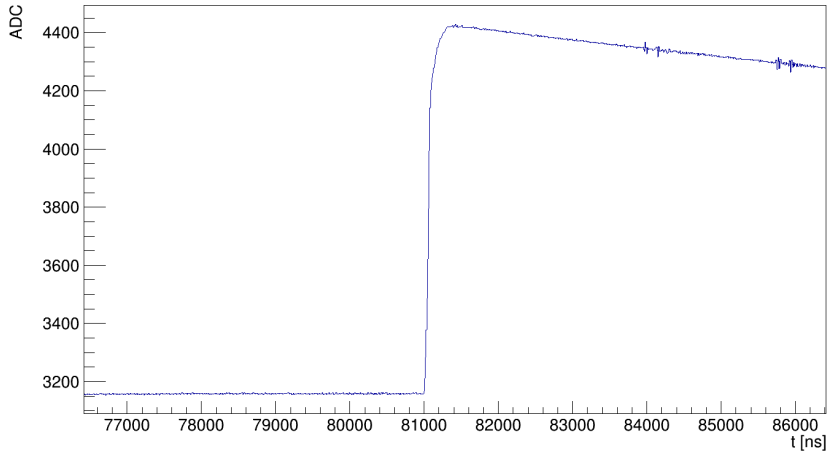

Figure 5.4: The hig frequency trace.

5.3.2 DSP modules and Data selection

Before a high level analysis can be carried out, a check on the validity of the recorded trace needs to be performed. This means that it needs to be ensured that nonphysical or pile up events are not part of of the analysis. These events need to be discarded beforehand such that the actual events of interest can be analysed. To do so, all data has been checked and a pile up rejection has been applied.

In general there are two types of pile up events. Both types lead to an improper energy reconstruction and should be dismissed before the data analysis. This can be done in two ways. The first way is to look at the baseline of the pulses and to identify so called pre-trigger pile

up events. A pre-trigger pile up is an event that sits on top of the decaying tail of a previous event. The previous pulse did not fully recover yet and the new pulse does not start from the baseline, i.e. the baseline is not fully restored. This can lead to an overestimation of the energy and reduces the overall energy resolution. Fortunately these events can be identified by looking at the slope of the baseline prior to the identified trigger of the event. A negative slope of the baseline indicates a not recovered pulse and the event can be dismissed.
The second method is to look the total number of found triggers in a trace, which identifies post-trigger pile ups. Here two or more events happen after the first trigger but within the digitized trace. In this case more then one trigger can be found and it can therefore easily be identified by the trigger module. Figure 5.5 shows the two types of pile up events in the same waveform. Overall three events are stored in one trace.

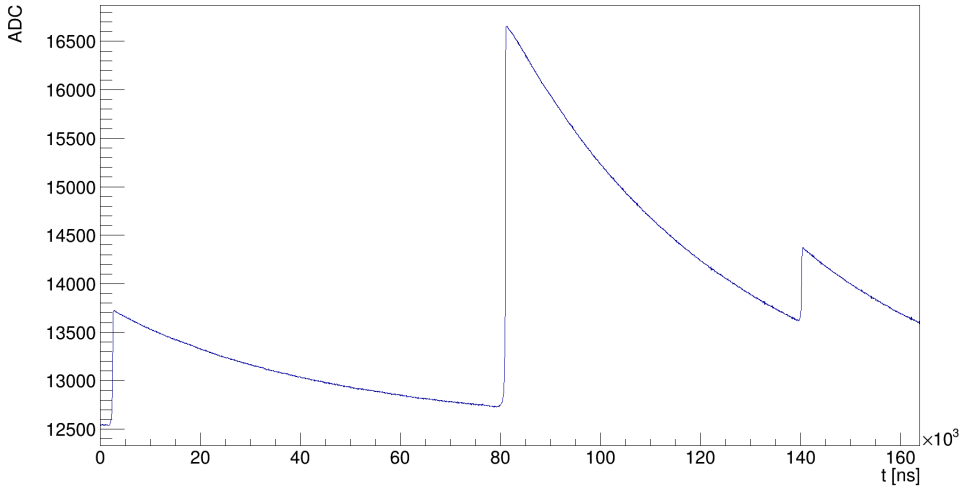

Figure 5.5: An example of pile up events. The identified leading edge trigger is in the middle of the plot around 81 ns. This events sits on top of a tail of a previous event on the left side of the diagram. The third event happened shortly after the main trigger and can be seen in the right part of the figure. An energy reconstruction module would fail on this recorded trace.

It becomes clear that at least two GELATIO modules are needed for this pile up rejection. These two are the trigger module and the baseline module. The trigger module shapes the raw pulse by applying a moving window deconvolution, which deconvolves the pulse with an exponential function, in order to compensate the exponential decay of the pulse, and differentiates the waveform. Then the pulse is integrated by a moving window average. On this shaped pulse the leading edge discriminator is applied, which looks for the first sample above a previous defined

value. If the pulse stays above this threshold for a given amount of samples (i.e. time), the trigger will be stored. Otherwise the trigger will be discarded and the trigger search continues from there on. This module scans the total trace and can store multiple triggers such that the total number of found triggers identifies post-trigger pile ups.
For the pre-trigger pile up identification the so called baseline module is applied. It calculates the mean value and the root mean square (RMS) of a defined window at the beginning of the trace, which is associated with the baseline. Additionally it performs a fit with the first two terms of a Taylor expansion of an exponential decay $f(t) = a + b - {}^{b}/_{\tau} \cdot t$ on the baseline window to estimate its slope and the amplitude of the decay. a and b are free fit parameters and τ is the decay time of the read out system. If this reconstructed amplitude exceeds a given value the pulse is marked as pile up. It is clear that the accepted values for a fitted slope depends on the recorded noise (RMS). For this analysis the fitted amplitude had to be lower then 50 times the RMS to be accepted.

All the events that survive the pile up rejection are regarded as valid events and the analysis modules can be applied. The most important parameter of interest is of course the energy of the detected event. There are several possibilities to reconstruct the energy of a digitized waveform. Different digital filters can give different results and the energy resolution can vary strongly. Overall the energy resolution is highly dependent on the electronic noise and different filters can compensate better for noise than others. Also the shape of the digitized pulse can have an effect on the energy reconstruction. Some pulses show a sharp transition from the rising edge to the decay whereas others transit more smoothly. This shape of the transition can impact the reconstructed energy, depending on the used method. In this work two different energy reconstructions have been tested and compared. The first module is a semi-Gaussian filter ("Gauss") and the second is a trapezoidal filter ("Gast"). In comparison, the Gast filter gives a better energy resolution and its estimated energy will be used throughout this work.
The two different energy estimators rely on different shaping methods. Both filters operate on the longer low frequency trace. The Gaussian filter is based on a moving window average (MWA), whereas the averaging time and the number of averages can be chosen freely. This transforms the waveform into a Gaussian like shape. After this transformation, the maximum of the resulting shape is taken as the energy value. It is clear that the energy resolution depends on the number of MWAs as well as the width of the window. The width influences the noise compensation but also effects the identification of the maximum charge. In this case a 13

times application of a 10 us window width has been chosen. An example of the first 5 MWA operations can be seen in figure 5.6.

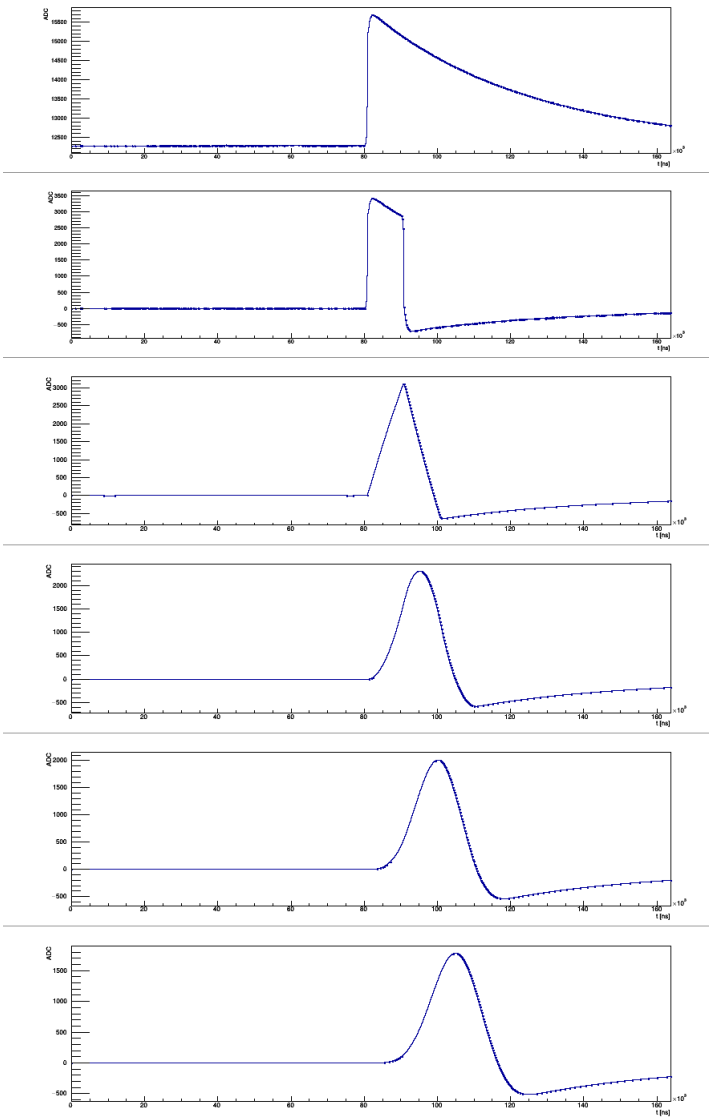

Figure 5.6: This is an example of a five times application of a moving window average on a recorded trace. The averaging window is 10 μs. The maximum of the each trace can be used as energy estimator.

The Gast filter reconstructs the energy by a moving window deconvolution (MWD). This is the equivalent to the application of a differentiation and a deconvolution with an exponential function. After the MWD a moving window average (MWA) is applied with a smaller window than used for the MWD. This shapes the output into a trapezoidal form. The energy information is stored in the amplitude of the output and the energy estimator is taken as the maximum.

A step by step application is visualized in figure 5.7, Overall the Gast filter tends to show a better performance then the Gauss filter. A comparison of the energy resolution curve is shown in figure 5.8. The computation of such a resolution curve will be discussed later in more detail. From now on the standard energy reconstruction will be the Gast energy estimator.

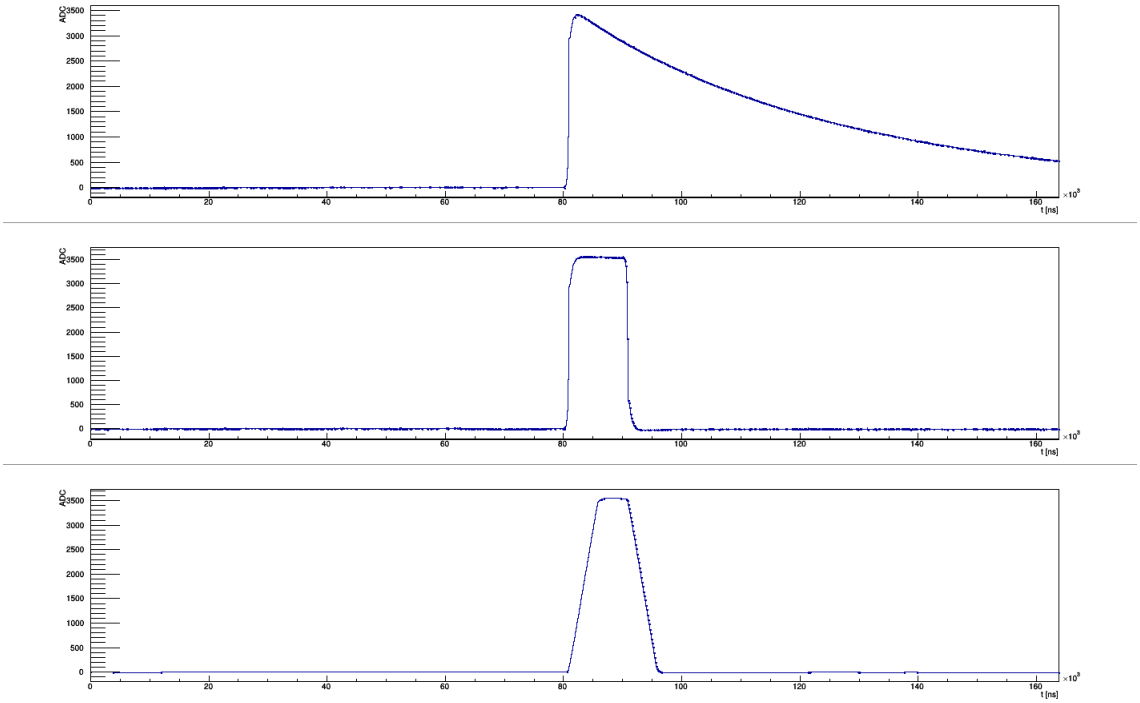

Figure 5.7: An example of the construction of the Gast filter. The low frequency trace (top panel) is shaped by a moving window deconvolution (middle panel) and then averaged by a moving window average. The energy is the maximum of the final trace.

Of course the energy is not the only parameter of interest. The goal of a best possible background classification demands a detailed pulse shape analysis and therefore other parameters needs to be constructed. This includes the maximum current associated with one event, different rise time parameters, providing information on the rising edge of one event, and the decay of the trace.

The term risetime describes hereby the time between two points of the trace that is needed by the pulse to reach a certain voltage value. These two points can be set individually and freely. Only the noise level sets restrictions on the identification of the time points. If the noise is too high, the low value point can already be reached before the actual pulse starts. This would lead to miscalculated, way too long rise time. In this analysis, different rise time parameters

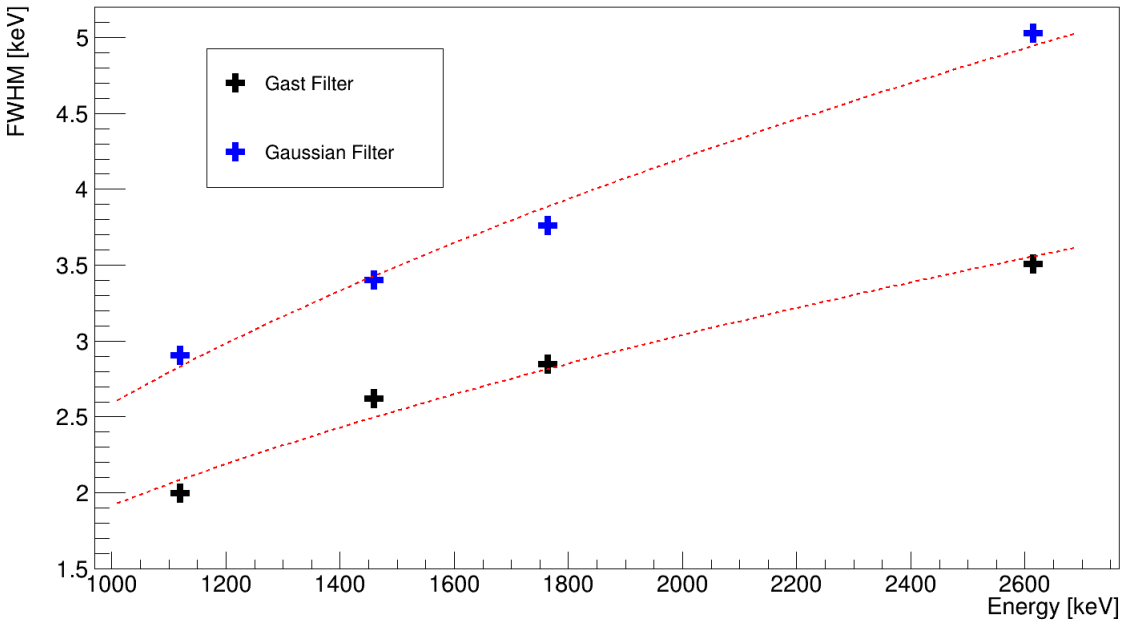

Figure 5.8: A comparison between the Gaussian energy reconstruction and a Trapezoidal (Gast) energy reconstruction.

have been calculated and analyzed. The most important for this work is the rise time between 0.5% and 90% of the maximum of the trace. The risetime provides information on the origin of the pulse inside the detector. The charge collection time of charge carriers close to the p+ is low, and hence the rise time is low. Contrary, a high risetime is a property of events located far away from the p+.

The computation of the maximum current Amplitude A is done by a moving window differentiation with a given time window. The input is the already averaged high frequency trace of the event. If no averaging is applied beforehand, noise contributions will spoil the output, whereas averaging to much will result in a loss of information. The differentiation will give an approximation of the induced current at the read out electrode and the maximum of the current, as well as its position, are the output for the further pulse shape analysis. Such a current pulse is shown in figure 5.9.

In general, the current is the derivative in time of the measured charge pulse $I(t) = \frac{dQ(t)}{dt}$.

Another parameter that can be calculated with GELATIO is the rise time asymmetry rt_{asy}. This parameter was introduced in 2013 and details can be found here [Ago13]. The basic idea of this parameter is to look at the current pulse of an event and to evaluate its symmetry.

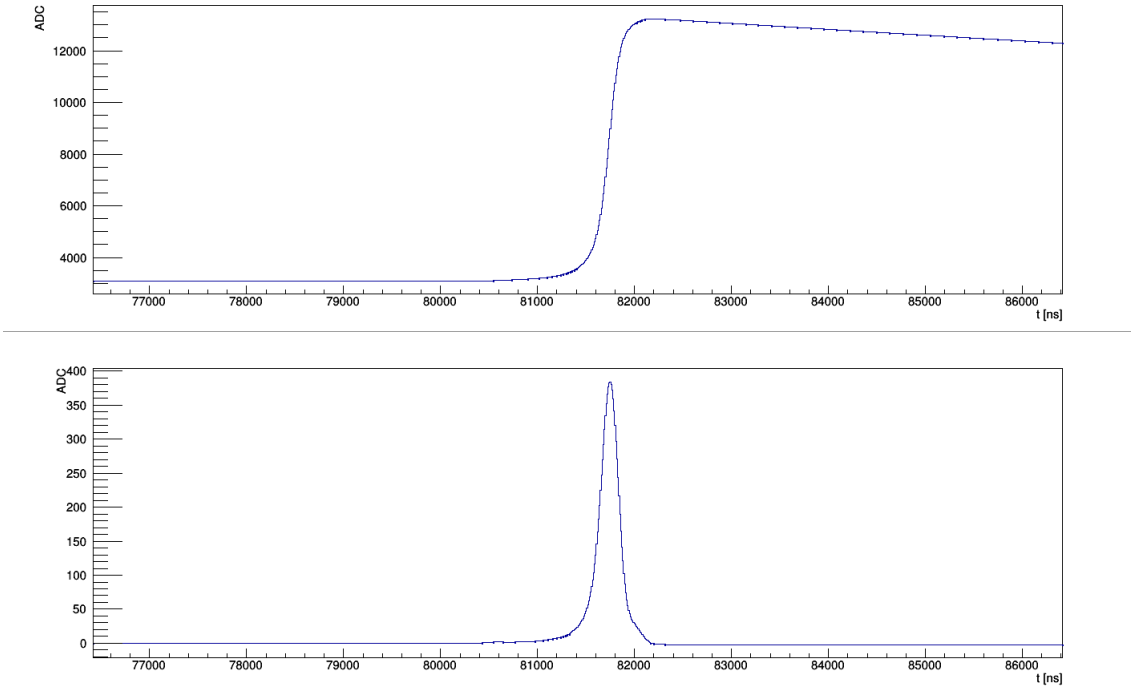

Figure 5.9: The current calculation: The top panel shows the averaged high frequency trace and the bottom panel the differentiated trace. The maximum A of the current pulse serves as input for the pulse shape analysis parameter A/E.

An ideal Gaussian is symmetric around its mean value, which means that the time between one defined point of the left side to the mean value is the same as for the right side. If the symmetry is broken, these times differ and the ratio between them gives the asymmetry parameter. This means a perfect Gaussian shape would have an asymmetry parameter equal to 1. The computation is given by:

$$\mathrm{rt}_{\mathrm{asy}} = \frac{\mathrm{rt}_{\mathrm{R}} - \mathrm{rt}_{\mathrm{L}}}{\mathrm{rt}_{\mathrm{R}} + \mathrm{rt}_{\mathrm{L}}}$$

If the right side of the current pulse is wider than the left side, the current stays high (closer to its maximum value A) for a longer time. This means the charge pulse shows a softer edge in the transition between the rising and the decay.

Contrary, when the right side is smaller than the left side, the current becomes smaller in a shorter time and the charge pulse shows a sharper edge. Therefore, the asymmetry parameter provides a measure on the sharpness of the charge pulse. An example of this parameter construction is drawn in figure 5.10. The corresponding module is already included in the

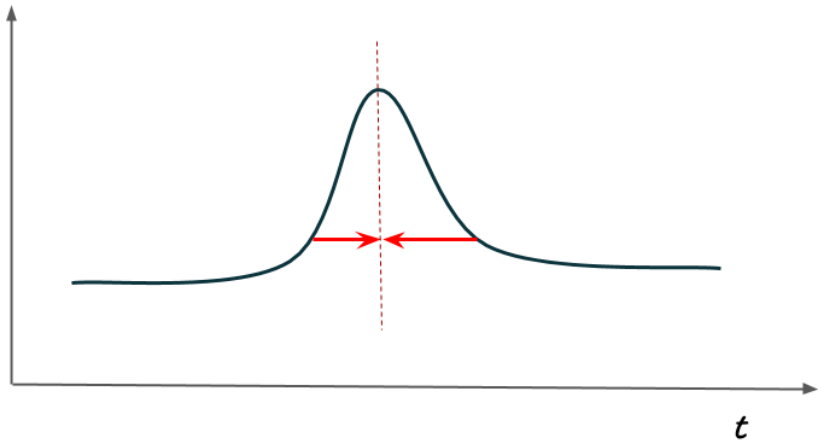

Figure 5.10: A sketch of the asymmetry Parameter. The ratio of the rising edge of the current pulse is compared to its fall.

GELATIO software within the current amplitude calculation.
The output of all applied modules are now stored in separate tier2 level files.

5.3.3 Calibration

Once the tier2 level is created, calibration routines can be applied. The first step is the energy calibration, which is customized for each setup. The calibration is based on the identification of one or multiple lines which are either prominent in the background spectrum or are part of the spectrum of the used source itself. Also explicit calibration sources can be used additionally.
In any case, the identification of at least one raw mean value of a given line is needed. This can be for example the 2614.5 keV line of the ^{208}Tl decay. If the line position in the raw spectrum is roughly identified, an energetic region around its raw position is chosen and the line is fitted with a simple Gaussian function $f(x) = \frac{a}{2\pi\sigma} \cdot \exp\left(\frac{b-\mu}{\sigma}\right)$. The extracted mean μ of the fit (referred as Tl_{raw}) serves as the input to a first calibration giving the new energy values as $E_{new} = \left(E_{raw} \cdot \frac{2614.5\,keV}{Tl_{raw}}\right)$.
Nevertheless the gain of the read out electronics is in general energy dependent. This means that a calibration routine based on only one line can lead to deviations in the spectrum, especially when a brought energetic range is investigated. Ideally, the calibration should contain at least

three lines within the spectrum in order to correct for possible non-linear behaviour. Generally, the calibration routine can be divided into three steps:

- Identification of known lines and determination of their means μ_i.
- Calculation of the calibration value c_v for each line.
- Application of an energetic correction on $c_v(E)$.

For the first step, regions around the raw lines are selected and the lines are fitted with a simple Gaussian function. The calibration values $c_v(E)$ for each line is given by the division of the literature value of the lines $\mu_{lit,i}$ by the fitted means μ_i. When plotted against the raw energy, the already mentioned energy dependence can be seen. Ideally this dependence should be linear but in some cases it can show quadratic portions, hence at least three lines should be included in the procedure. Figure 5.11b shows a raw spectrum of a background run from the TUBE setup, the selected lines for the calibration and the linear energy dependence. With the first order polynomial fit, the energy dependence of the calibration value can be modeled as $c_v(E) = E_{raw} \cdot a + b$ and the resulting calibrated energy can then be expressed as

$$\begin{aligned} E_{cal} &= E_{raw} \cdot c_v(E) \\ &= E_{raw} \cdot (E_{raw} \cdot a + b) \end{aligned}$$

The new calibrated energy can now be plotted in a histogram. This is shown in Figure 5.11a. A measure on the goodness of the calibration gives the deviation of the calibrated lines to the literature values.

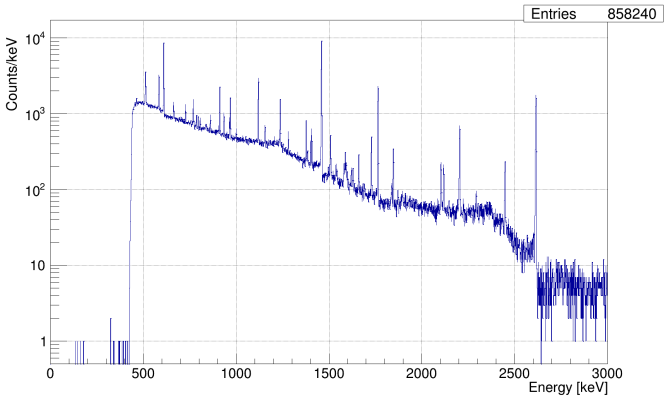

(a) A Background spectrum of the TUBE setup.

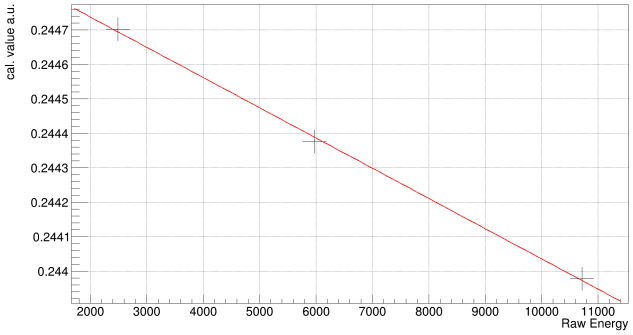

(b) The calibration values $c_{v,i}$ against the energy for the TUBE setup. A linear energy dependence can be observed.

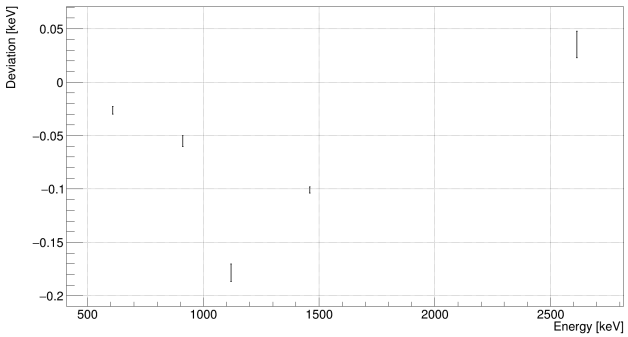

(c) The deviation of calibrated background lines of the TUBE setup against literature values.

Figure 5.11: Overview of the calibration process. First the raw calibration lines have to be identified (a), then the calibration value of each line is calculated (b). The final deviation of the calibrated lines to the literature values are shown in (c).

5.3.4 Energy resolution

One of the most important parameters for the purpose $0\nu\beta\beta$ search is the energy resolution $\Delta E(E)$. Within this work, the energy resolution will be given by the full width at half maximum (FWHM) of a given line. The FWHM is connected to the standard deviation of a Gaussian line by the relation $\mathrm{FWHM} = \sqrt{2 \cdot \ln 2} \cdot \sigma$. As discussed earlier, the resolution of a measured spectrum is energy dependent. It is measured by performing a fit on multiple lines and extracting the Gaussian standard deviation σ in energy dependence. In a real measured spectrum the lines are not pure Gaussian. Especially big detectors can suffer from a ballistic deficit and charge trapping due to their comparable long drift times. Also the background level underlying the gamma lines are different for each side of the line. In order to account for the background level, and the non Gaussian part of the line, the fit function that is used to extract σ has to be adapted. This fit function consist of three parts and is given by equation 2. The first part is a simple Gaussian with its standard deviation σ and represents the pure Gaussian part of the line. Its standard deviation can be transformed to the FWHM and serves as the resolution measure. This fit approach has been taken from [SK16]

The second part of the function covers the low energy tail of the measured lines which can be accounted to the ballistic deficit and charge trapping. The third part accounts for the background which is described as a constant plus a step function, expressed by a Gaussian cumulative distribution. An example of the three components of the fit on a ^{214}Bi line at 609 keV can be seen in figure 5.12.

$$\begin{aligned} y(x) \; = & \frac{S_g}{\sqrt{2\pi}\sigma} \exp\left(\frac{-(x-x_0)^2}{2\sigma^2}\right) \\ & + \frac{S_t}{2\beta} \exp\left(\frac{x-x_0}{\beta} + \frac{\gamma^2}{2\beta^2}\right) \cdot \mathrm{erfc}\left(\frac{x-x_0}{\sqrt{2}\gamma} + \frac{\gamma}{\sqrt{2}\beta}\right) \\ & + \frac{A}{2} \mathrm{erfc}\left(\frac{x-x_0}{\sqrt{2}\sigma}\right) + B \end{aligned} \tag{2}$$

As said, the resolution can be taken directly from the Gaussian part of the fit output and can be determined for different line in the spectrum. Ideally the energy dependence of the resolution is proportional to the square root of the energy $\mathrm{FWHM} = \sqrt{a + b \cdot x}$, with a and b as free fit parameters. For the TUBE setup the resolution curve is calculated on five different background lines and an example of the resulting curve is plotted in figure 5.13.

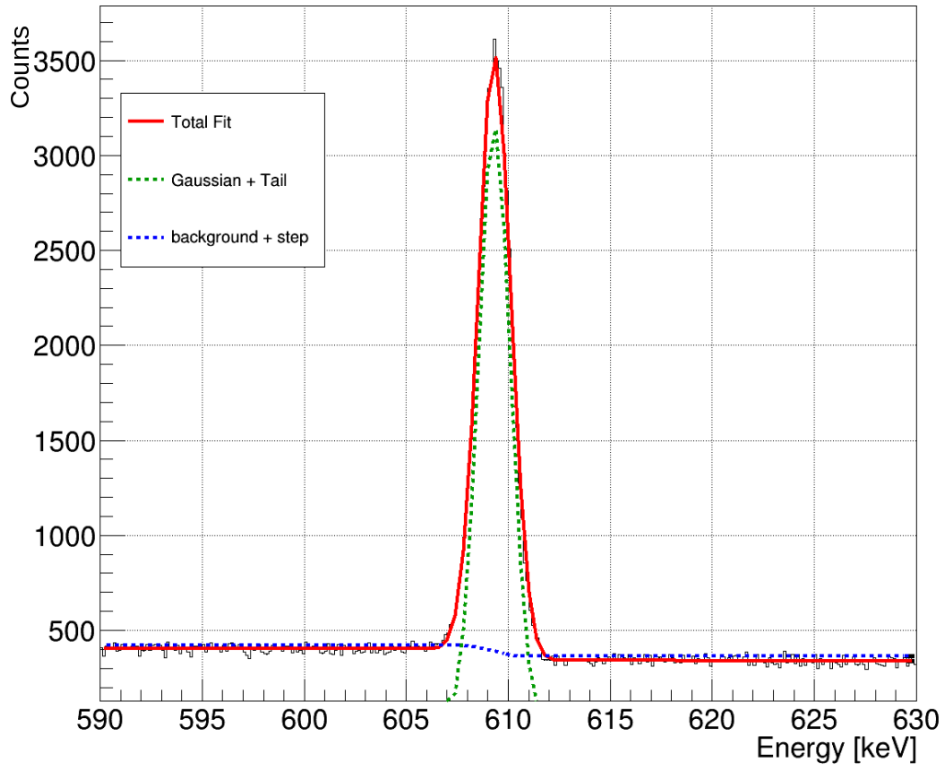

Figure 5.12: An example of he three component fit on a $609\,\mathrm{keV}$ ^{214}Bi Line. The total fit is shown in red, whereas the pure Gaussian part is indicated as the green dashed line. The background level is shown as the blue dashed line.

5.3.5 A/E

One of the most important parameters for the pulse shape determination is the "A over E" (A/E). It is an important parameter in terms of background classification for BEGe and ICPC detector types. This section will describe the calculation of the A/E parameter, its calibration and its efficiency determination. The procedure of the A/E calculation and calibration can be divided into three parts, the reconstruction of the maximum current amplitude A, the calculation of the raw A/E value and the normalization and energy correction of the A/E. This leads to a normalized and calibrated A/E on which the background classification efficiency can then be determined. The procedure to normalize and calibrate the A/E has been taken from [Bud09] and [Wag17].

The first thing that is needed is the current of the measured charge pulse and its calculation has been described before. Then A must be divided either by the calibrated or uncalibrated

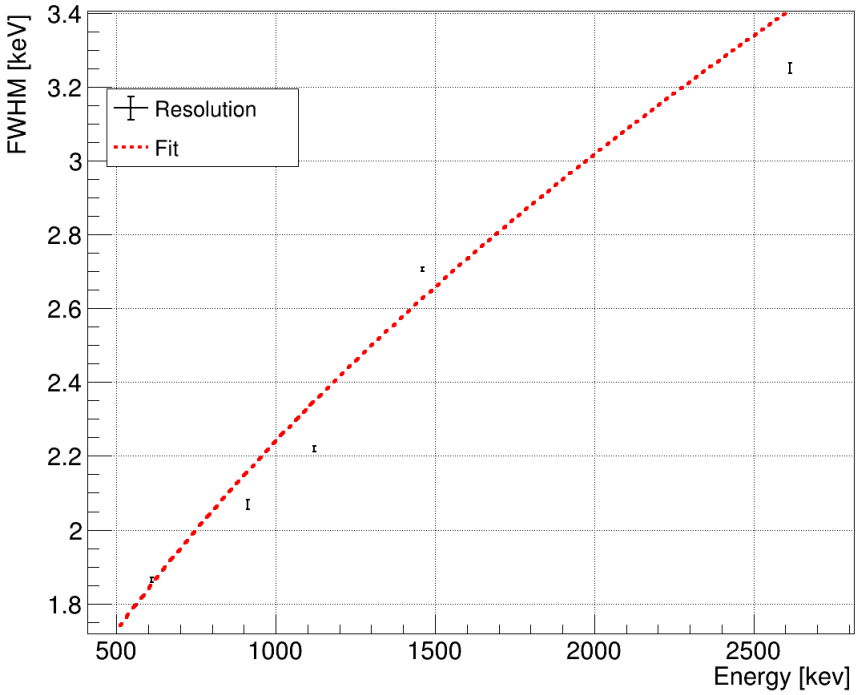

Figure 5.13: The fitted FWHM of five selected lines in a background run from the TUBE setup. The resolution is plotted with its fit uncertainty and the red dashed line gives the fitted energy dependence.

energy. The choice to divide A by the calibrated or uncalibrated energy changes the absolute value and the further correction that is needed.

Nevertheless, both A/E methods show an energy dependence. The method which uses the uncalibrated energy E for the A/E carries this energy dependence in both the value of A as well as in the value of E. If A is divided by the calibrated energy however, the energy dependence is only carried by the A value since the calibration procedure corrects for this energy dependence. An example of a received raw A/E distribution for the calibrated energy is plotted in figure 5.14. When the raw A/E is plotted against the calibrated energy, the slight energy dependence is visible as a negative slope of the single side band. This behaviour is shown in figure 5.15.

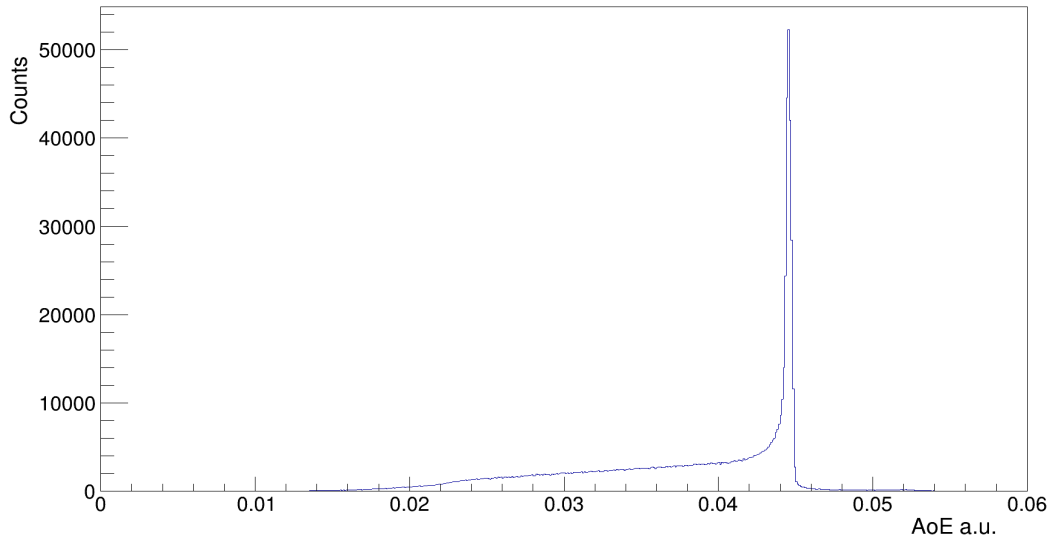

Figure 5.14: The total A/E distribution of a background run from the TUBE setup. Most events are single site interactions and make up for the visible peak. The lower tail covers the multi site events.

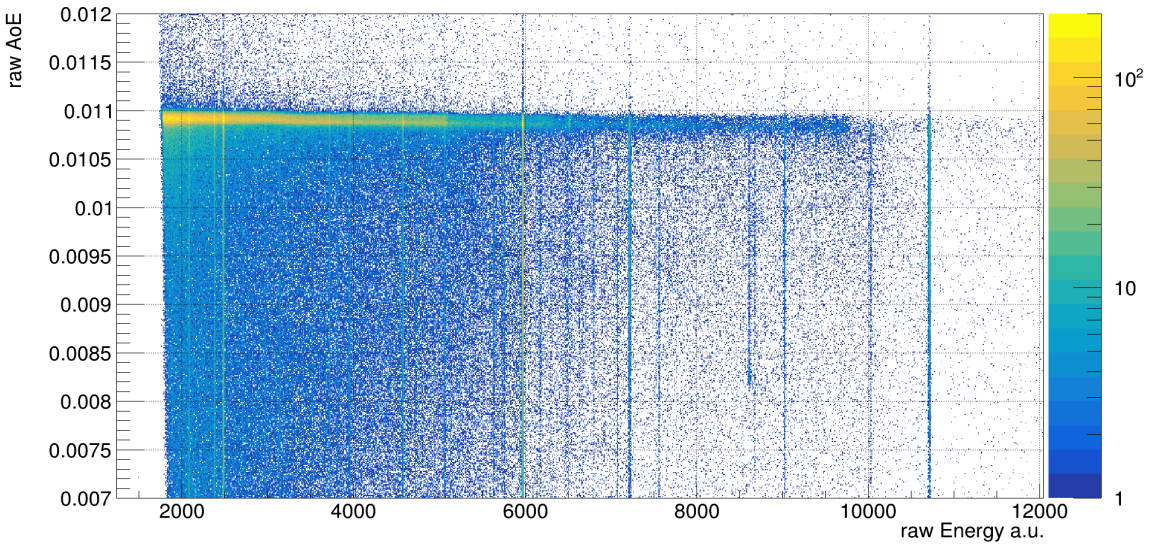

Figure 5.15: The raw A/E distribution against the uncalibrated energy. An energy dependence can be seen as a negative slope of the single site band. The high multi site fraction of the full energy lines is visible as low A/E values.

The next step is to normalize the raw A/E to the single site band and to apply an energy correction. Therefore, it is important to understand how the A/E is distributed at different energy regions and for different events types. The important event types for the A/E analysis are:

- **Full Energy Peak (FEP):** The FEP is a discrete line created by Gammas which originate in a Gamma decay of a radioactive isotope. Its total energy (which is given by the nuclear energy levels of the decaying isotope) is deposited in the Germanium detector.

- **Double Escape Peak (DEP):** The DEP is created when a γ photon undergoes a pair production inside the Germanium. The Gamma is transformed into an electron positron pair. The electron deposits its energy promptly whereas the positron decays into two 511 keV annihilation photons again. These two Gammas are emitted in opposite direction to each other. If both Gammas escape the detector without any further interaction only the created electron deposits its energy. The resulting DEP is therefore a sharp line with a small FWHM at energies exactly $2 \cdot 511\,\text{keV}$ below the initial energy of the incoming γ. The energy deposition of the DEP is highly localised and hence the DEP serves as a good proxy for single site events.

- **Single Escape Peak (SEP):** The SEP is similar to the DEP with the difference that one of the created annihilation deposits its energy in the detector. This means that the measured SEP is exactly 511 keV below the initial energy of the incoming γ and its event topology is dominated by multi site events.

- **Compton Continuum (CC):** CC events are event types in which the incoming γ undergoes one or multiple Compton scatter processes but do not deposit its total energy in the detector. The possible deposited energy ranges hereby from close to 0 up to the Compton edge of the initial γ line which gives the maximum energy that can be deposited in a single Compton scattering.

These different event types show different fractions of SSE and MSE. The expected SSE fraction can be derived from Monte Carlo simulations. Again the reader may be referred to [Bud09] and [Wag17] for more details.
For a BEGe detector the DEP, as a proxy for SSE, is expected to show a SSE fraction of above 90 %. In the SEP only a very low SSE fraction of below 5% is expected. The FEP SSE fraction

should be below 10% and the CC SSE fraction in the order of 45%. The SSE fractions are expected to be lower for ICPC detectors, since the bigger geometry provides a higher change for the photons to deposit energy, e.g. a photon has a bigger chance to Compton scatter more than once compared to BEGe detectors.

An example of a normalized and calibrated A/E distribution of a ^{228}Th scan and the four highlighted event type regions can be seen in figure 5.16.

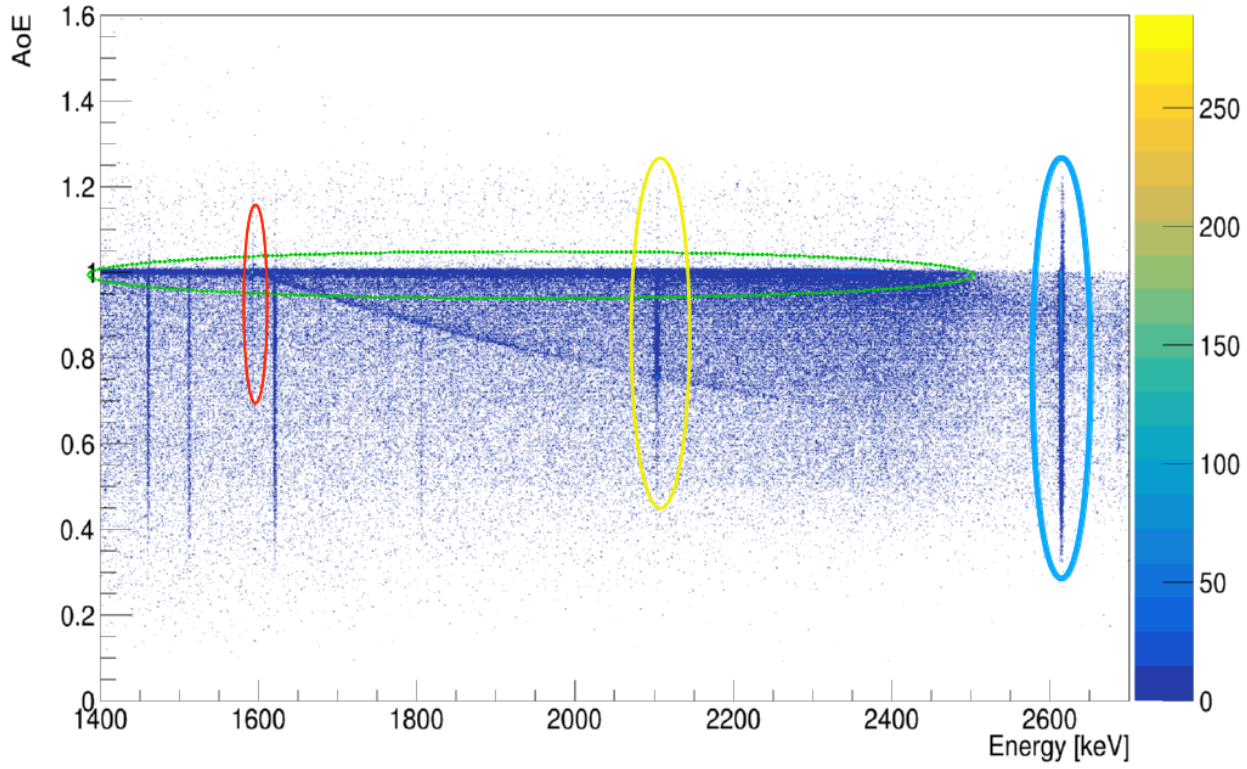

Figure 5.16: Example of an calibrated A/E distribution of a ^{228}Th scan. The colored ellipses indicate the four different event type regions.
In blue the FEP, in yellow the SEP, in red the DEP and the green dashed line indicates the CC region which has to be subtracted by the peak regions.

The single site band normalization is then done by extracting the events from several CC regions. A great portion of photons which undergo a Compton scattering is expected to only interact once and then leave the detector without any further energy deposition.

When the raw A/E distributions of different CC regions are stacked into a histogram, they can be fitted with a Gaussian plus a tail and a background as described in equation 2. In this analysis the exact spectral shape of the raw A/E distribution is only of minor interest since only the position of the Gaussian mean is needed for the energy correction. An example fit is shown in 5.17. For each selected energy region the Gaussian mean is computed and the result is plotted against the energy. A linear energy dependence can be seen (figure 5.18).

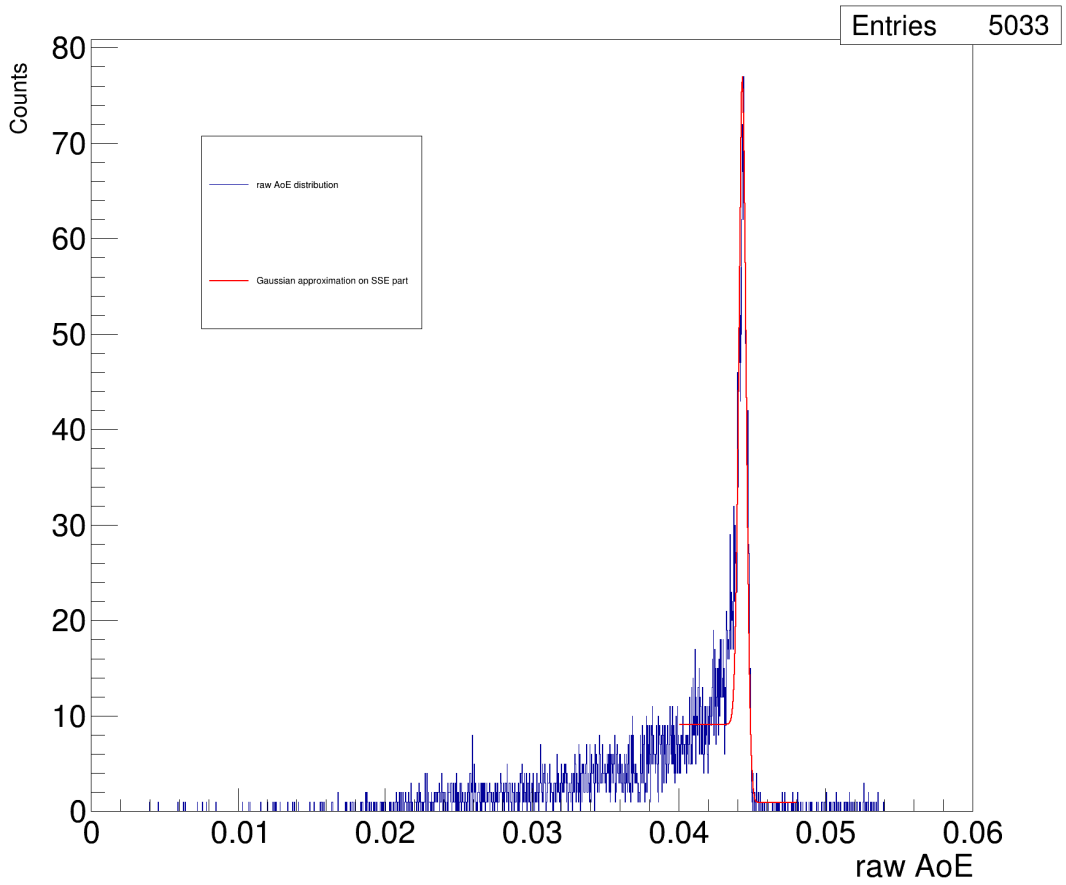

Figure 5.17: Example fit on one CC events in the energetic region around 2350 keV.

The final A/E is then normalized and corrected for this energy dependence.

$$\mathrm{A/E(E)} = \frac{\mathrm{A/E_{raw}}}{\mathrm{a} - \frac{\mathrm{b}}{\sqrt{E_{cal}}}}$$

The resulting A/E against the calibrated energy has been shown in figure 5.16. This calibrated and normalized A/E distribution can now be used to determine single site events. The efficiency of its identification power can be estimated upon the double escape peak (DEP) of the ^{208}Tl

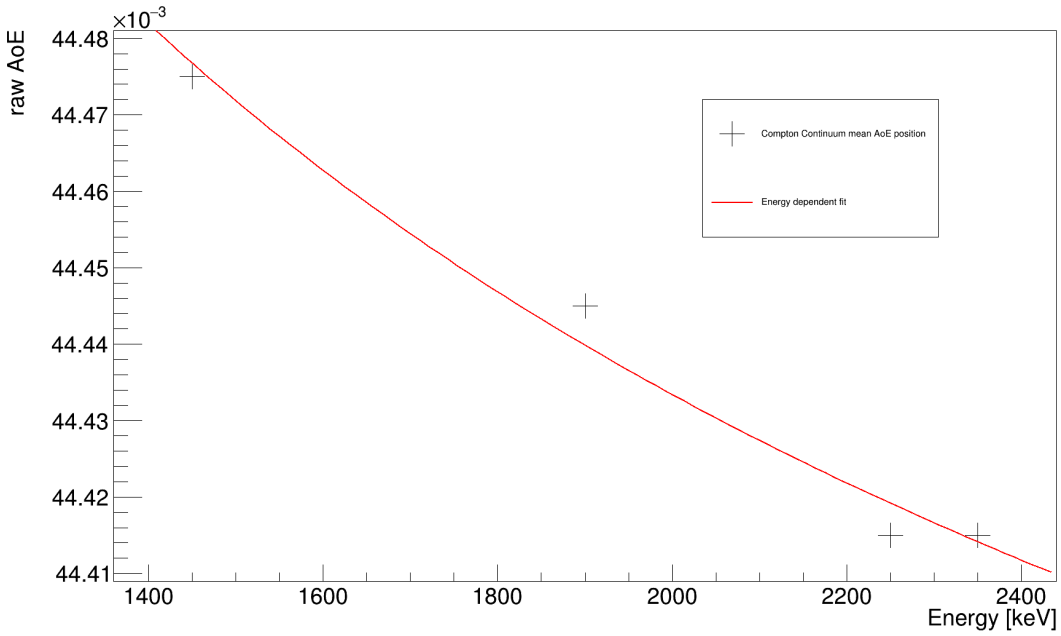

Figure 5.18: The energy dependence of the A/E for a background run from the TUBE setup.

line.

From MC-Simulations, the amount of SSE events within the DEP is expected to be around 90%. The non SSE portion comes from Bremsstrahlung of the detected electron as well as from underlying multiple Compton scattered events falling accidentally in the DEP energy region. A simple A/E cut is a one sided cut of the low A/E values. This means that events with a A/E value lower then the cut value will be dismissed. This procedure can be repeated with a shrinking acceptance window, i.e the cut value becomes higher each iteration.

5.4 The decay time and the DCR

Usually, the decay of the recorded waveform is only given by the decay time $\tau = RC$ of the feedback circuit of the read out electronics. But as mentioned above, previous measurements of the ORTEC PPC detector PONAMA I showed that the decay of the waveform is enhanced if α particles interact in the vicinity of the passivated surface. For simplicity, these events will be called surface events in the following.

Surface events show an altered behaviour compared to bulk events within the detector volume. The biggest and most obvious difference is the degradation of the measured energy in dependence of the incident radius. The distance to the p+ contact influences the charge collection

and a part of the energy is "missing".
Another visible effect is the increase of the decay time of the pulse in radial dependence. This effect has been studied prior to this work and is called delayed charge recovery (DCR). It is assumed that a fraction of the charge carriers is re-released and part of the lost energy recovers on a longer timescale than the exponential decay time τ. This leads to a recovery of a fraction of the charges when the pulse is already decaying and hence the decay time is shifted to higher values. The origin and the exact mechanisms involved in this charge recovery are not fully understood yet, and therefore, the investigation of the decaying part of the surface events is crucial.

One way to determine the decay time τ of a digitized waveform is by performing an exponential fit. The output of the fit directly gives the decay time parameter τ and its implementation is rather simple. The fit uses the baseline subtracted low frequency trace of the event and is given by:

$$y(x) = A \cdot \exp\left(-\frac{1}{\tau}(x - t_0) \right) + b,$$

where, A is the amplitude, b represents the a possible remaining baseline fluctuation of the trace and t_0 is a fixed offset, depending on the exact turning point between rising edge and decay. Since τ is not dependent on the absolute values of the amplitude, no further energy correction is needed.
One disadvantage of this procedure is that it is computational heavy and a long computation time is needed. Therefore the analysis of the decay will be mostly carried out by the approximate parameters, such as the DCR, that will be introduced in the following.

As it has been reported here [AAIB+20], the parameter that can measure the deviation of the decaying tail of a waveform to the single site bulk events, is the so-called DCR parameter. The basic idea of this parameters is to look at a defined part of the pole-zero corrected tail of the signal (i.e. deconvolved wit an exponential function), and to determine the slope δ of the tail between two points. δ should be distributed around 0 for bulk events, and is greater than 0 for events with an enhanced decay time.
However, δ is still energy dependent, making also the DCR parameter energy dependent. The differences in height between the two points, and therefore the absolute value of δ, is proportional to the amplitude (i.e proportional to the energy). δ is the rate of the recovered charge.

Statements about the strength of the delayed charge recovery cannot be directly made from δ alone. For the determination of the fraction of delayed charges that are recovered, the energy of the event need to be considered as well. However, a cut based on the delayed recovery rate removes the same events as a cut based on the delayed recovery fraction, making both parameters good pulse shape discrimination parameters.
In this work, an alternative DCR parameter will be introduced, that is normalized by the energy of the event, and provides the fraction of delayed charge recovery. In the following an overview of the pole-zero corrected DCR computation will be given. The pole-zero corrected DCR will be called DCRpz from now on. Furthermore the energy normalized DRC parameter (DCRn), which was developed in this work, will be introduced and the differences will be shown.

For both DCR parameters a baseline subtraction is needed. This is done by computing the baseline from the first 1500 values of the low frequency trace and subtracting it from the trace. For the DCRpz calculation a pole-zero correction is now applied. The pole-zero correction is the application of an inverse high-pass filter on the signal with a given decay time τ and a sampling width Δ. τ can be extracted from a single site bulk event by fitting the tail of the signal with an exponential decay. This correction compensates the decay from the RC feedback loop. [SK16] shows that the n'th sample of the PZ-corrected waveform y_n can be calculated from the measured waveform samples x_i as:

$$y_n = \left(g \cdot x_n + \sum_{i=0}^{n} x_i \right) \cdot m,$$

$$\text{with} \quad g = \frac{\exp(\Delta/\tau)}{1 - \exp(\Delta/\tau)} \quad , \quad m = 2 \cdot \frac{1 - \exp(\Delta/\tau)}{1 + \exp(\Delta/\tau)}.$$

The parameter δ can now be defined as the difference between two previously defined time points t1 and t2. The time difference is dependent on the length of the digitized waveform. In this analysis the time difference is set to $20\,\mu s$.

$$\delta = \frac{y2 - y1}{t2 - t1} = \frac{y2 - y1}{20\mu s} \tag{3}$$

.

After the pole-zero correction, all bulk events will have a slope distributed around 0, independent of their energy. An example of the pole-zero corrected signal is shown in figure 5.19.

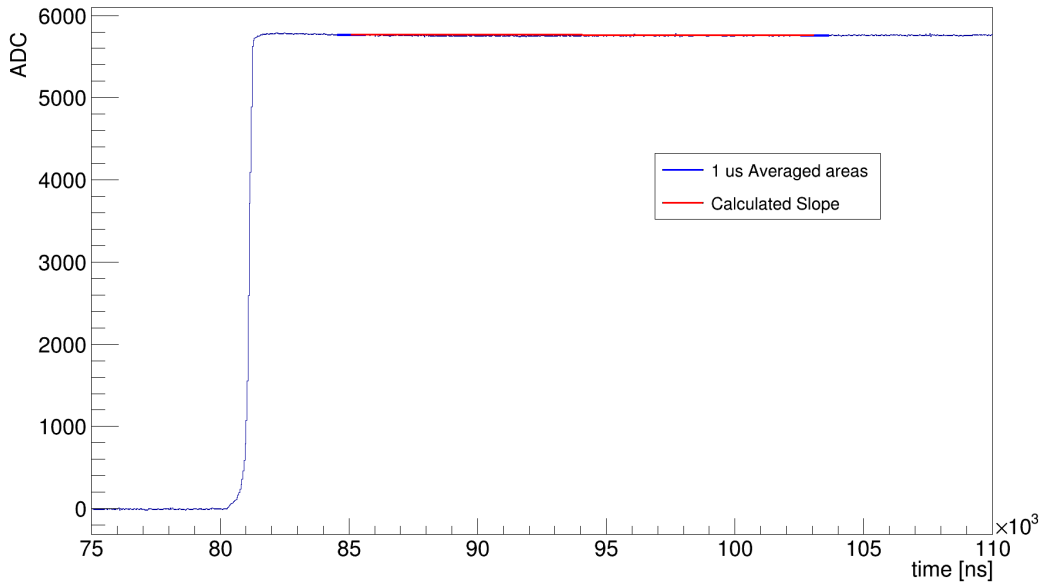

Figure 5.19: This is an example of the approximation of the decaying slope. The green lines indicate areas on which the starting and endpoint of the slope will be calculated. The red line indicates the computed slope.

Events that have an enhanced decay time compared to bulk events, will show a non zero slope after the pole-zero correction. A longer decay time will result in a positive slope. Additionally, the DCRpz parameter can also be calibrated on a given single site event acceptance percentage. Therefore, the slope δ needs to be shifted by the Gaussian mean of the singe site bulk event distribution, and scaled with the e.g. 99% acceptance value for the single site events.

However, the absolute value of the slope is still energy dependent. A smaller initial amplitude will result in a smaller slope, although the decay time difference remains the same. This behaviour is illustrated in figure 5.20. Here four different exponential decays are visualized. The decays differ from each other by their Amplitude and their decay time, whereas two decays have the same Amplitude of 100 and two decays have a higher amplitude of 150. The lower ones differ from each other by their decay time, whereas one function decays with a τ of 40 arbitrary units, while the other decays with a time constant of 42. The same decay times are set for the higher amplitude functions. Now a pole-zero correction with a decay time τ of 40 is applied on all decays and the resulting slope is calculated. As expected, the two decays with a τ of 40 have a slope δ equal to zero that shows no dependence of the amplitude. The δs of the decays with a longer τ are proportional to the amplitude.

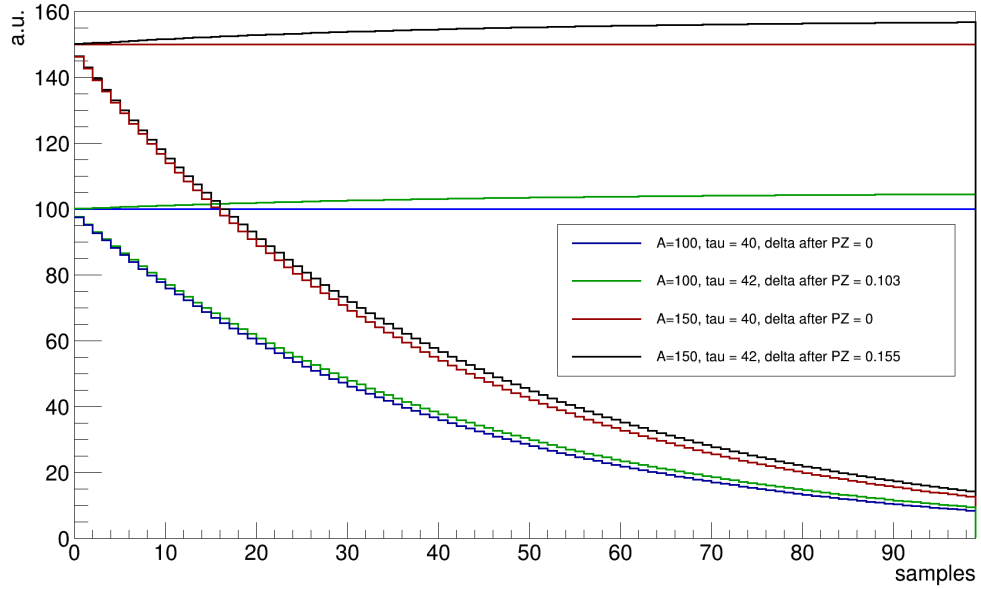

Figure 5.20: An example of energy dependence of the calculated slope δ of a pole-zero corrected waveform. There are two exponential decays with decay times of 40 a.u. and two decays with decay times of 42 a.u. The absolute value of δ depends on the amplitude A, which is proportional to the energy. The δ of a 1.5 times higher amplitude signal is 1.5 times higher.

This DCRpz parameter is a measure of the deviation of the decay time of an event to the mean single site bulk events and the slope δ is the rate of the delayed charge recovery. The multiplication of δ with the calibration constant (in case of a linear calibration) and a time window Δt gives the energy that is recovered within this time window. This rate is dependent on the energy of the event. High energetic events have a higher charge recovery rate, since more charges are involved.

If this energy dependence is uncorrected, a statement about the magnitude of the delayed charge recovery cannot be simply made only considering the slope δ (or the calibrated slope DCRpz) alone. If two events show enhanced DCRpz parameters at different energies (enhanced compared to bulk events, i.e. compared to the time constant the pole-zero correction has been applied with), the lower energy event can have a lower DCRpz value, although it has the same, or even a higher fraction of recovered charges than the higher energetic event. For statements about the fraction of the recovered charge, and therefore the strength of the delayed charge recovery effect, the energy dependence need no be included. This can be done in several ways. In this work the energy correction is done by normalization and will be explained in the following.

Similar to the DCRpz calculation the DCRn needs a baseline subtracted waveform as input, but no pole-zero correction will be applied. The slope δ of the baseline subtracted waveform is calculated similar as for the DCRpz. First the time window on which the slope will be calculated is defined. This is done by using the output of the GAST trapezoidal energy estimator, which is the noise corrected maximum of the baseline reduced waveform, and to find the time point at which the waveform drops to 97% of its maximum. The point t1 is then computed as the point 2.5 μs after this 97% point and t2 is the point 22.5 μs after the 97% point, such that the slope is calculated on a 20 μs window. δ is now the difference of a 1 μs average around the the two time points divided by the time difference between t1 and t2 of 20 μs.

$$\delta = \frac{\mathrm{y2} - \mathrm{y1}}{\mathrm{t2} - \mathrm{t1}} = \frac{\mathrm{y2} - \mathrm{y1}}{20\mu\mathrm{s}} \tag{4}$$

.

An example of a calculated slope is given in figure 5.21.

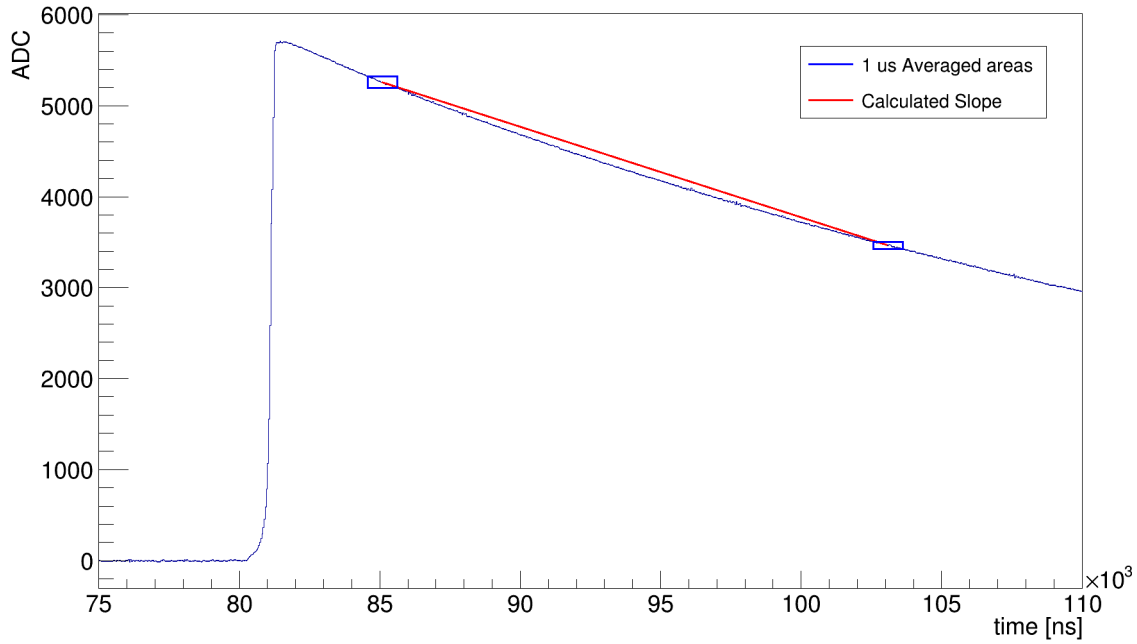

Figure 5.21: This is an example of the approximation of the decaying slope on a baseline subtracted waveform. The blue boxes indicate areas on which the starting and endpoint of the slope will be calculated. The red line is the computed slope between the two boxes.

δ is still energy dependent, as its absolute value depends on the maximum amplitude. The energy dependence can be corrected by normalizing δ by its energy

$$\text{DCRn} = \frac{\delta}{E_{gast}}.$$

This is equal to calculating the slope of the normalized waveform. The received slope is the slope of the normalized waveform and the mean bulk events distribution will center around an arbitrary negative value whereas slower decaying events will have higher values closer to zero. Similar to the DCRpz calibration the DCRn can also be calibrated by shifting it to the 99% acceptance value of single site events.

Both the DCRpz and the DCRn are a measure of the difference of the decay time to single site bulk events. The DCRn however additionally makes a direct statement on the fraction of recovered charges within time window. The DCRn can be directly compared to events with different energies.

A comparison between the two parameters for a background run is shown in figure 5.22.

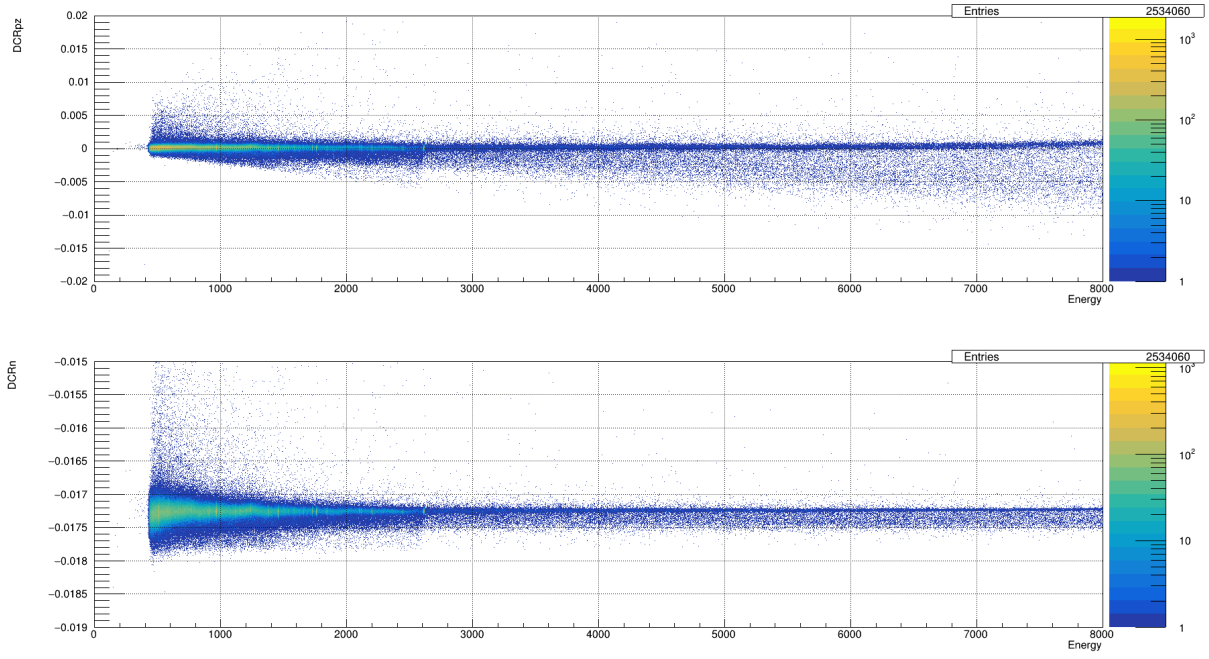

Figure 5.22: A comparison between the DCRpz and the DCRn parameter for a background run. The DCRn (bottom) projects a direct measure of decay time differences, whereas the DCRpz gives differences at higher energies a bigger weight.

However, as it will be shown in 6.4, the discrimination capability is equally strong for both parameters.

5.5 Monte Carlo and Pulse Shape Simulations

In this thesis, the pulses of the ORTEC detector have been analyzed and simulated extensively. For this simulation campaign two separate types of simulation have been performed whereas the output of the first serves as input for the second. In the following both simulation types and their implementation will be discussed.
As the name suggests, a Monte Carlo simulation has an analogy to a game in a Monte Carlo Casino. The outcome of a process (e.g. the player rolling a dice, a particle moving through matter) is dependent on a (previously defined) probability. But, whereas the rolling of a dice only has 6 possible outcomes, the interaction of particles with physical volumes can have way more possibilities and are additionally highly dependent on the environmental settings and physical processes that are considered.

The software that was used in this work is for the Monte Carlo simulation is the software MaGe [BBC+06]. MaGe is an addition on the program Geant4. Geant4 has been developed by the CERN group in the late 90's. MaGe makes use of the simulation functionality of Geant4 and adds geometries, materials and input/output structure, tailored for the needs of the needs of the GERDA and MAJORANA collaborations.

MaGe also provides a template class for Inverted Coaxial detector geometries which can be easily used and adapted. A simplified, but still detailed TUBE-setup geometry has been implemented. The geometry consists of the detector itself, a PTFE bar which is holding the golden read out pin that is pushed on the p+ contact, a Copper encapsulation with an open slit on the bottom side of the detector, a Copper plate that is serving as an infrared shield between the encapsulation and the collimator. The collimator itself is also implemented as a detailed cylinder with a bore hole, composed out of three individual parts, which are stacked together. The top part is used for the source placement, whereas the middle part works as the main collimator body. The bottom part has a worked edge such that the collimator can be moved along the IR shield surface. All materials of these three components can be chosen independently. The whole setup is placed inside a steel tank, which is implemented as a simple steel cylinder. This setup includes the most important geometries for the Monte Carlo simulation. For a more detailed simulation, especially if a more detailed background modulation would be wanted, additional features like cables, screws, the flange of the vacuum pump, etc. could be added. A visual representation of the total volume can be found in figure 5.23

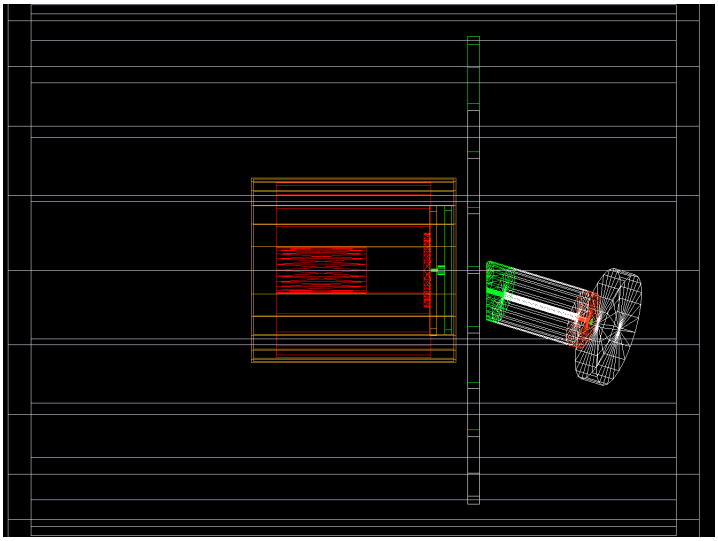

Figure 5.23: MaGe TUBE setup implementation. The collimator length is 50 mm.

The workflow of the simulation is to place a radioactive source, ^{241}Am and ^{90}Sr within this work, into the collimator and to simulate a 100 million radioactive decays. If any particle, that is produced within the whole process of the decay, deposits energy within the detector volume, an event will be created and stored to the output file. The event contains several information, containing the step wise energy deposition, the step wise incident position of the particle, the particle identification number and the total deposited energy.
The output of an example simulation of 100 million ^{241}Am decays is shown in figure 5.24. Here, the first incident position of each event are shown, whereas the color indicates the particle type. An α particle, that reaches the detector surface is marked as a red dot. The black dots are photons that are produced in the deexcitation process of the daughter nucleus.

This output, i.e. the hit positions with their corresponding energies, can now serve as an input for a pulse shape simulation program. There are different programs available and two of them has been tested within this thesis. This work will focus on one of them, the open source mjd_siggen program, developed by David Radford et. al [Rad]. This program is widely used within the GERDA, Majorana and LEGEND collaboration, which makes the produced results comparable. In the following a brief introduction to the pulse shape simulation and the processing of the Monte Carlo output will be given.

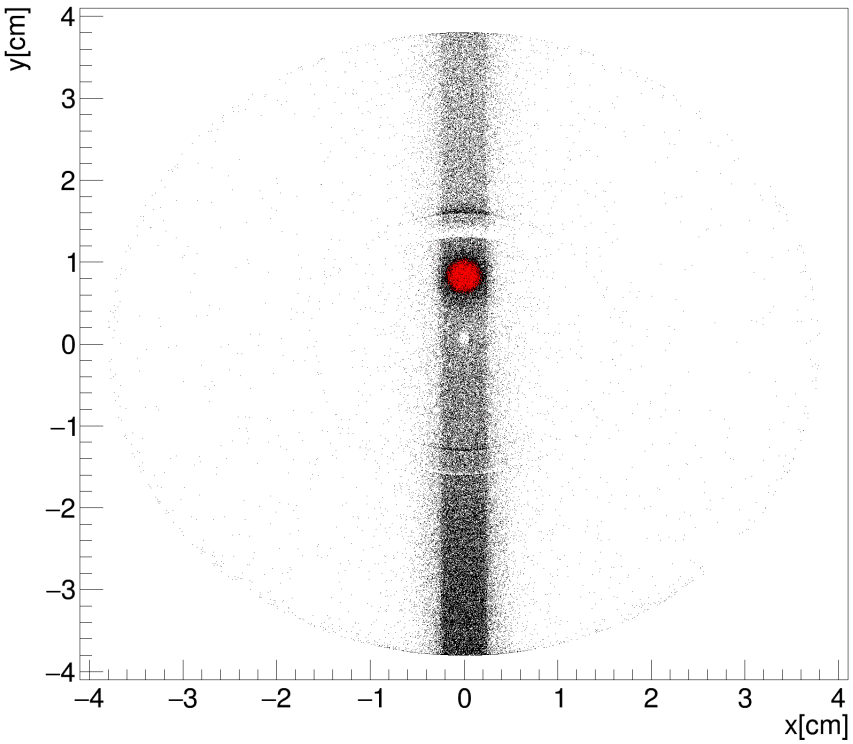

Figure 5.24: The output of an example MaGe simulation. Left: The event distribution along the xy-plane of the detector. In red the α particles, in black the photons. Right: The deposited energy in the detector.

5.5.1 The Pulse Shape Simulation

A Pulse Shape Simulation (PSS) relies on two individual calculations. First, a field simulation needs to be performed, which means that the Poisson equation has to be solved for a given detector geometry. Hereby a simulation program can make use of the geometric symmetry of an Germanium detector, such that only one plane through the detector volume needs to be calculated. mjd_siggen nevertheless would also be capable of performing a full 3D-Simulation. However, this is computational very heavy and not needed for the purpose of this work.
When the detector geometry is set it is to split into a given number of grid points. The higher the number of grid points, the more precise is the calculated field. But the precision comes with the price of computing time. For this work a grid size of 0.01 mm has been used, which means that every 0.01 mm one grid point is set. Now a high voltage can be applied to the detector electrode which sets the boundary condition to the Poisson equation. With these

condition a Runge-Cutta simulation ca be performed which calculates the field on each grid point recursively, depending on the surrounding grid points. mjd _siggen can also calculate the depletion voltage and can simulate undepleted detectors. The weighting potential is calculated in the same way, which will produce the actual signal simulation later.
Once the fields are calculated, a charge carrier pair can be placed inside the detector volume according to the positions from the output of the previous Monte Carlo simulation, and the charges start to move along the electric field lines. The induced charge at the electrode will be given by the movement of the charges through the weighting potential until they reach the corresponding electrodes. In addition, a cloud size and the corresponding effects like diffusion and self repulsion can be added to the signal calculation. An example of a simulated electric potential and weighting potential is shown in figure 5.25. Figure 5.26 show a simulated SSE and a MSE. The MSE is hereby a superposition of more than one SSE.

In addition a modeling of the actual electronic noise can be performed in order to better match the measured pulses. Different models of varying complexity can hereby be applied. The simplest way to add electronic noise is to add a Gaussian noise on the waveform. From the data the noise parameters can be calculated. Each sample of the waveform will be shifted according to a Gaussian distribution with the data RMS as the standard deviation.
The decay of the trace due to the RC chain can also be modeled rather easy by applying a convolution of a function with the parameter $\tau = \mathrm{R} \cdot \mathrm{C}$. This parameter τ can be extracted by an exponential fit on selected SSE.
A bit more complex is the modeling of the rising edge. In reality, the limited speed of the charge sensitive preamplifier causes a limitation on the bandwidth of the measured pulse and serves as a band pass. This band pass smooths the rising edge of the pulse and it can be modeled sufficiently by a 2-pole response function [Pan18]. Unlike for the exponential decay, this response is not easy to extract by a fit on the data, hence the input parameters for the 2-pole convolution have been optimized by variation for several pulses and a comparison to the data. If the simulated pulse matches the data to a sufficient amount, the input parameters are frozen.
With this model, a more accurate pulse can be simulated. An example of such a full pulse with electronic model is shown in figure 5.27.

The output of a Monte Carlo simulation can now be used as the input for the pulse shape simulation. Each individual step of each event will be simulated and the resulting pulse is

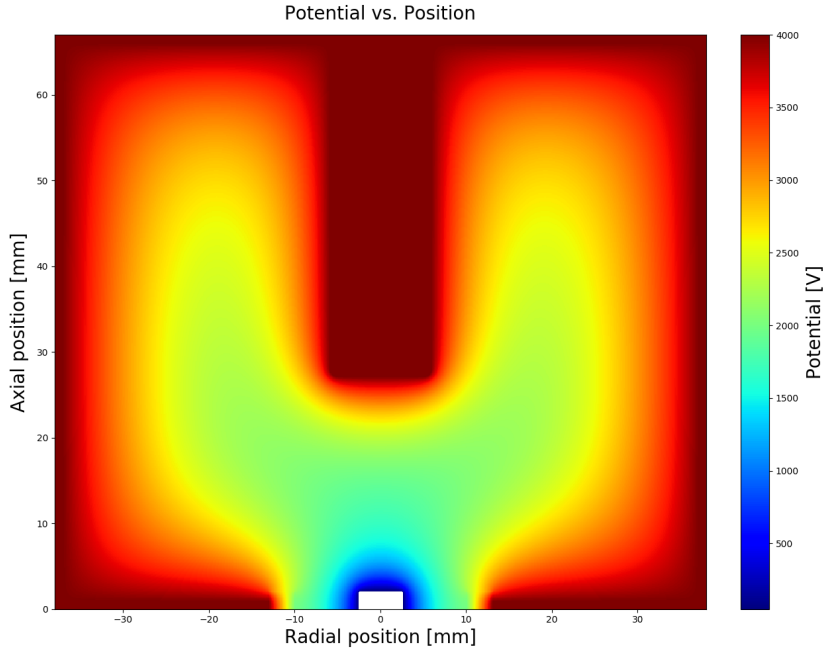

(a) Simulated electric potential inside the ICPC detector.

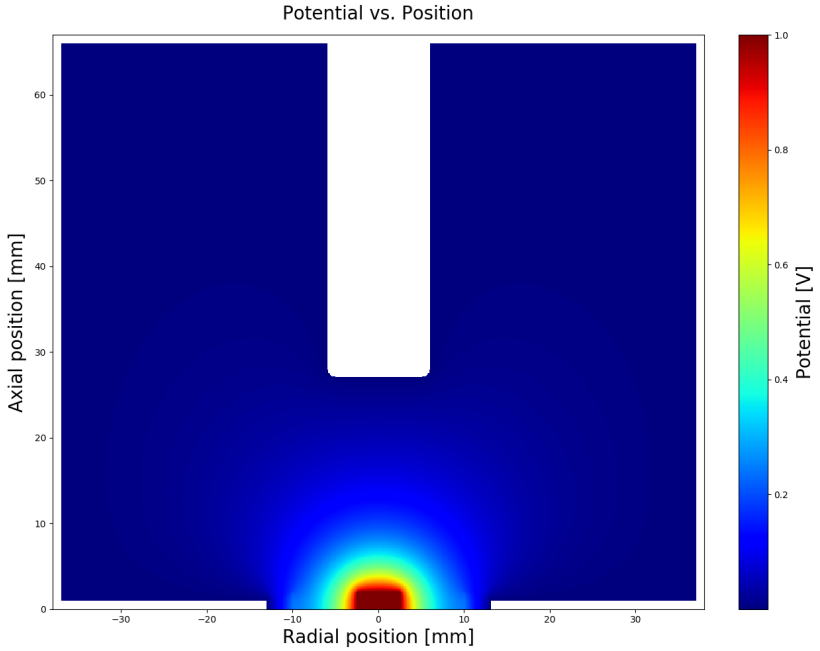

(b) Simulated weighting potential inside the ICPC detector.

Figure 5.25: mjd_siggen simulations of the potentials inside the ORTEC ICPC detector.

weighted by its energy deposition. The final pulse is then the superposition of all individual, weighted pulses. All pulses are stored in a separate file, which serves as input for the application of the electronic response. There, also the conversion to an MGDO-type event structure, that can be read and processed by GELATIO, is performed, leaving a tier1-like file that can be processed with the exact same tools as the actual data.

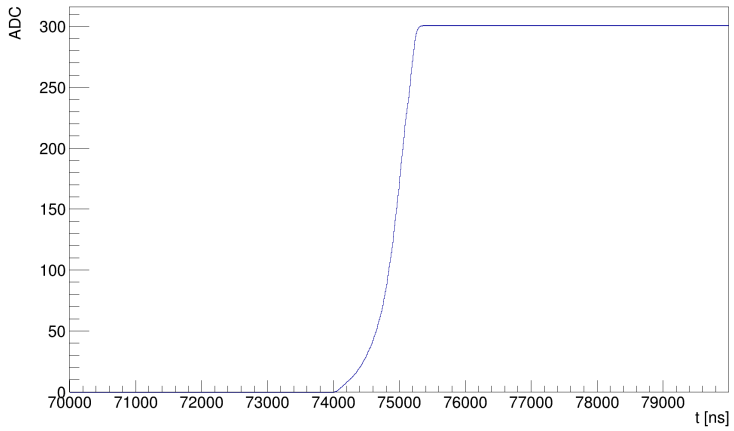

(a) Simulated single site event.

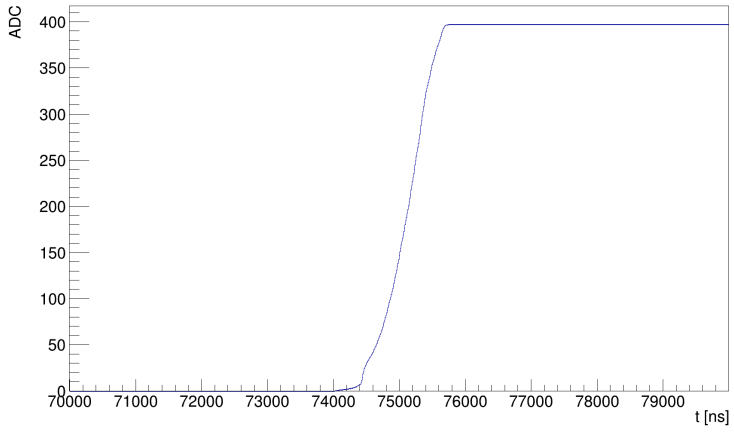

(b) Simulated multi site event.

Figure 5.26: mjd_siggen simulations different pulses inside the ORTEC ICPC detector.

5.6 First Data at HD

The first data taking with this detector has been performed in October 2017 at the Max-Planck Institute in Heidelberg. The goal of this campaign was to perform a general test and to validate the detector performance.

Therefore the detector has been irradiated with different radioactive sources, depending on which detector properties is being examined. In this work the analysis of two measurement types will be discussed. The types that have been analysed are:

- **High Voltage Scan:** In this measurement a ^{228}Th source is used to irradiate the detector while its voltage is being varied. This scan has the purpose to find the depletion voltage of the detector.

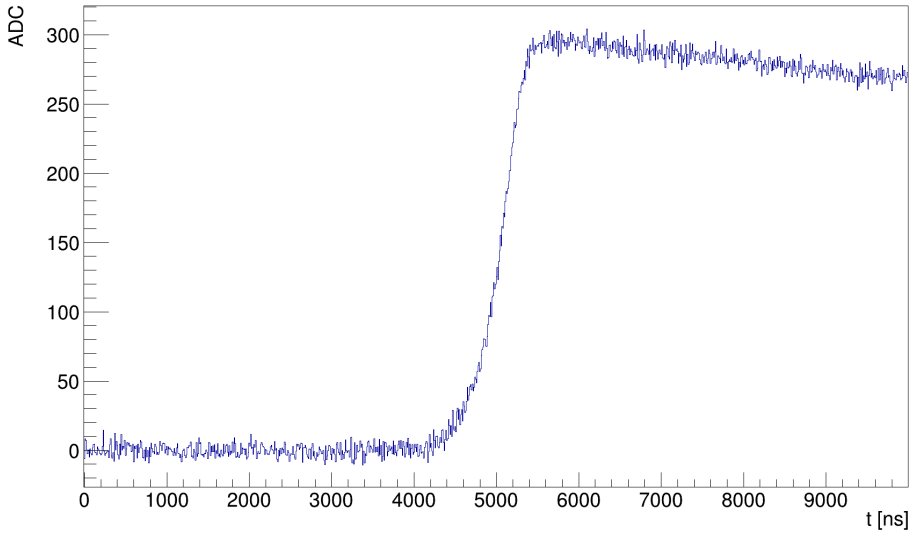

Figure 5.27: A simulated pulse with an additional Gaussian noise, a rising edge band pass and an exponential decay.

- **Pulse Shape Discrimination Performance:** Again a ^{228}Th is used. This time however a pulse shape analysis is carried out and the detector discrimination performance will be tested.

The detector output has been amplified with a Genius amplifier and and has been digitized by a Struck Flash ADC.

5.6.1 High Voltage Scan

The first step was to identify the depletion voltage of this detector and to observe its behaviour in dependence on the applied voltage. For this purpose the detector has been irradiated with ^{288}Th source while its applied voltage was ramped up from 1000 V to 3500 V in 250 V steps and ramped down to 1000 V afterwards again. In general the depletion of the detector is reached when all free charge carriers are evacuated towards the electrodes and the detector volume remains totally depleted. This voltage is of course dependent on the geometry and the size of the detector but also on the impurity concentration. Hence a measurement of the depletion voltage can give insides on the impurity concentration.
If the depletion is reached the capacity of the detector saturates at a constant level. Also the energy resolution, the peak position and the peak integral (or the count rate) saturate when

depletion is reached.
For this analysis the estimation of the depletion voltage is done by monitoring the energy resolution and the raw peak position during the ramp down of the voltage (i.e from 3500 V to 1000 V in mostly 250 V steps). A complete depletion is considered when these parameters show a stable behaviour. The first observable which was investigated is the energy resolution. Three prominent lines in the measured spectrum have been selected and their FWHM have been plotted against the applied voltage to the detector. The lines are:

- The 2614.5 keV line of the ^{208}Tl decay.
- The 581 keV line of the ^{208}Tl decay.
- The 1461 keV line of the ^{40}K decay.

The received FWHM for voltages between applied voltages of 1500 V and 3500 V is shown in figure 5.28. It has to be noted that the lines showed such a strong deformation for the 1000 V run, that a sufficient fit on the resolution was possible. Nevertheless, the slope of the resolution in dependence of the applied voltage shows nicely the saturation of the energy resolution for voltages above 2000 V. For a detailed determination, a finer scan in this voltage area would be needed. However, the full depletion and a stable performance of the detector can be considered at voltages above 2250 V.
Also the raw peak position of these lines show a stable behaviour for voltages above 2000 V. In the bottom plot of figure 5.28 this normalized peak position is plotted against the applied voltage. The normalization has been applied in reference to the highest voltage value.

Additionally the obtained results can be compared to simulations of the electric field inside the detector. For this purpose the software mjd_fieldgen by David Radford has been used. The software takes a configuration file as input in which all essential parameters have to be set. This include the exact geometry, dimensions and the impurity concentration of the detector as well as parameters defining the verbosity and level of detail of the calculation. An example electric potential and weighting potential can be seen in figure 5.25. The grid size of the field calculation was set to 0.1.

The depletion voltage is mainly driven by the geometry of the detector and also by the impurity concentration of the detector. For this simulation an impurity concentration of $-0.75 \cdot {}^{10^{10}}/_{\mathrm{cm}^3}$

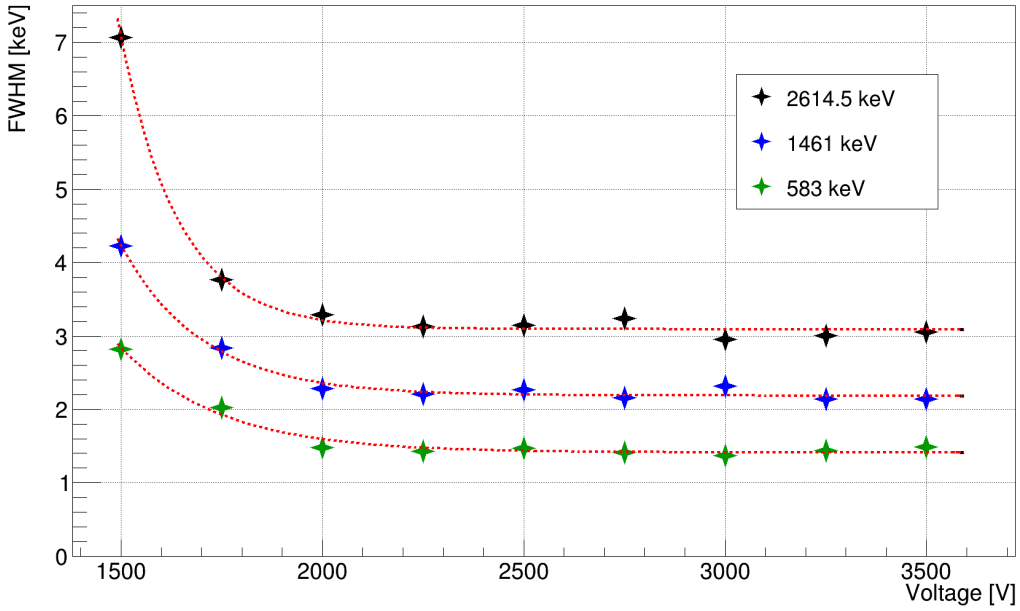

Figure 5.28: The FWHM of three different lines in dependence of the applied voltage. The depletion is reached for voltages above $2000\,\mathrm{keV}$.

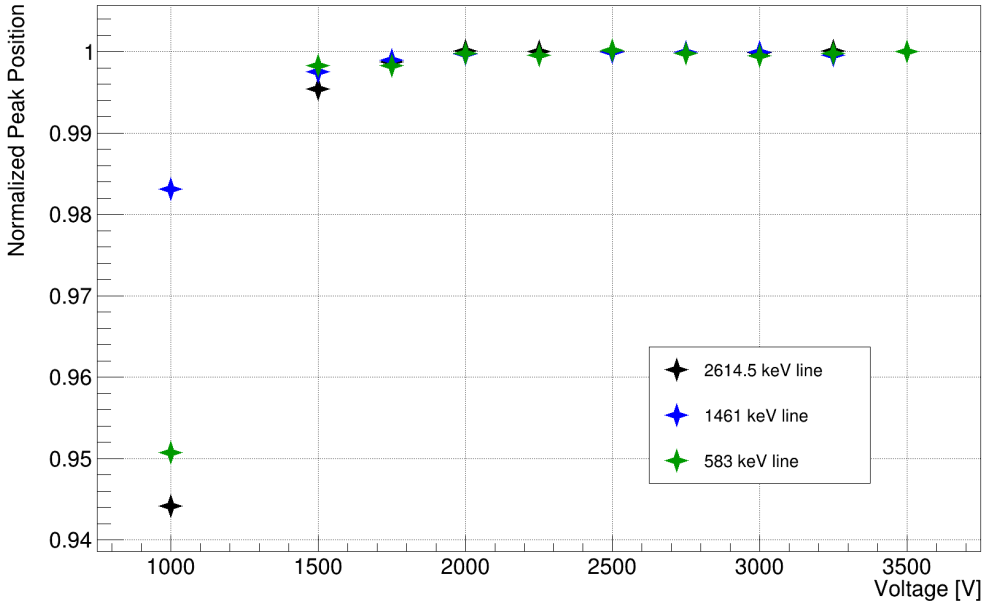

Figure 5.29: The normalized peak position of three different lines in dependence of the applied voltage. The depletion is reached for voltages above $2000\,\mathrm{keV}$.

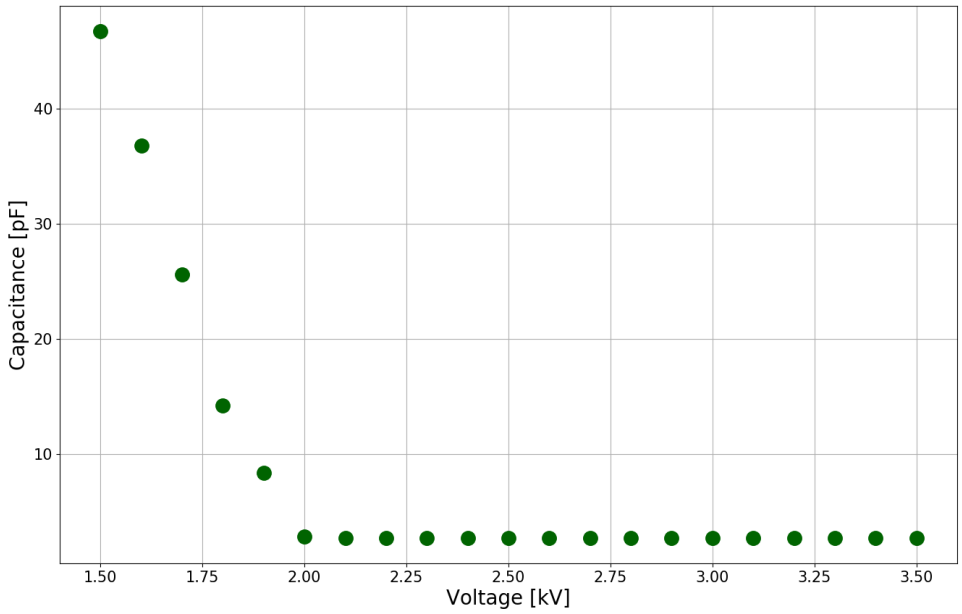

Figure 5.30: The simulated capacitance of the ICPC detector. The simulated depletion around 2 kV matches very well the measured depletion voltage.

at the top and $-1.4 \cdot {}^{10^{10}}/_{\mathrm{cm}^3}$ at the bottom has been used.
With these values the electric field inside the detector can be simulated in dependence of the applied voltage. With increasing voltage the detector capacitance will decrease until it reaches a constant level when the detector is totally depleted. This capacitance can be monitored during a simulated high voltage scan. Such an output can be seen in figure 5.30. A depletion is reached at around 2000 V when the capacitance reaches a constant level of around 2.6 pF. The simulation calculates a depletion voltage in good agreement to the measurement.

5.6.2 Pulse Shape Discrimination Performance

One of the most important performance characteristics is the pulse shape discrimination performance. For the BEGe detectors in GERDA background rejection technique based on the A/E pulse shape parameter has been developed. This technique can also be applied on ICPC detectors and hence the PSD performance is of great interest.
The PSD performance is measured in terms of the survival fraction of events at different energy regions after the A/E cut is applied. This PSD cut is based on the A/E parameter and its computation, calibration and normalization has been performed following the description in

section 5.3.5.

The computation of the A/E survival efficiency is now performed as a counting analysis. The A/E value of each event is checked if it is inside a given A/E acceptance window and the number of accepted events determine the survival fraction.

Energy region	Surv. Efficiency [%]
FEP	90.1
SEP	9.7
CC	33.1
DEP	5.8

Table 3: Survival fraction of the different energy regions after the A/E cut. These efficiencies show that the ICPC detector has a very MSE rejection capability.

First the borders of the window (i.e. the lower cut value and the higher cut value) will be set loosely, allowing for a high MSE fraction in the acceptance region. Now the cut window is being reduced successively and the survival fraction of the different regions will be determined. The high cut value is hereby twice as loose as the low cut value. If the DEP acceptance reaches 90% the corresponding survival fraction of the other regions will be frozen. The cut value is finally transformed into numbers of standard deviations σ of the DEP A/E distribution (i.e. how many σ of the DEP A/E distribution will be accepted).

For the measurement, a ^{228}Th source has been placed on top and later also on the side of the detector. The ^{228}Th provides a FEP, a SEP and a DEP and is therefore a good choice for a pulse shape discrimination test.
Additional the energy resolution is needed in order to set the proper ranges around the γ lines. The fit of the resolution has been done according to the procedure described earlier and the resulting resolution curve can be seen in figure 5.31. Overall a decent resolution could be achieved in the order of 3 keV FWHM at 2000 keV. The resulting survival fractions for the top run can be seen in figure 5.32 and are stated in table 3. The x-axis is here the cut value in terms of $1-\sigma$ of the A/E distribution at the DEP. Overall, the detector shows a good MSE rejection.

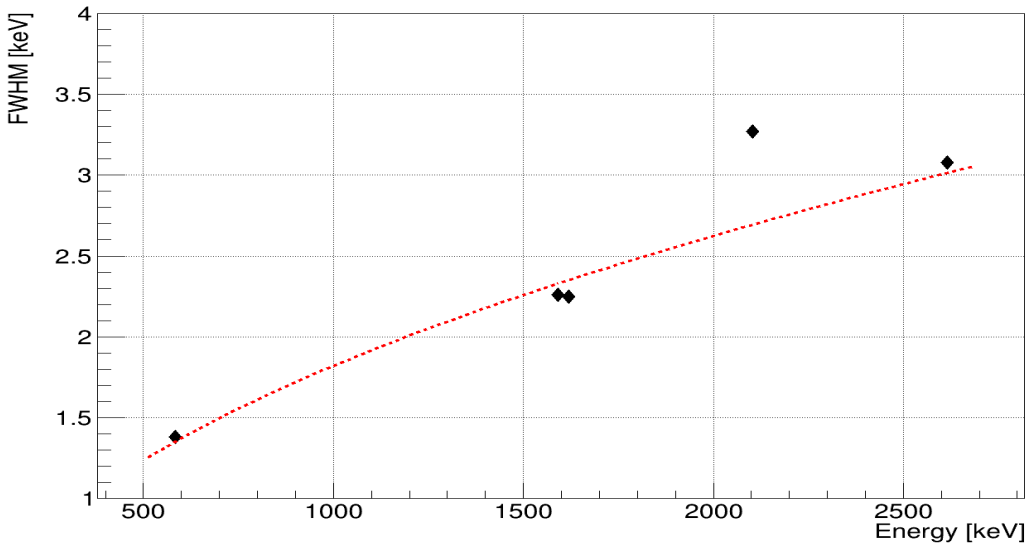

Figure 5.31: Fitted resolution curve for the ^{228}Th source run. The energy resolution is in the order of 3 keV FWHM at 2000 keV.

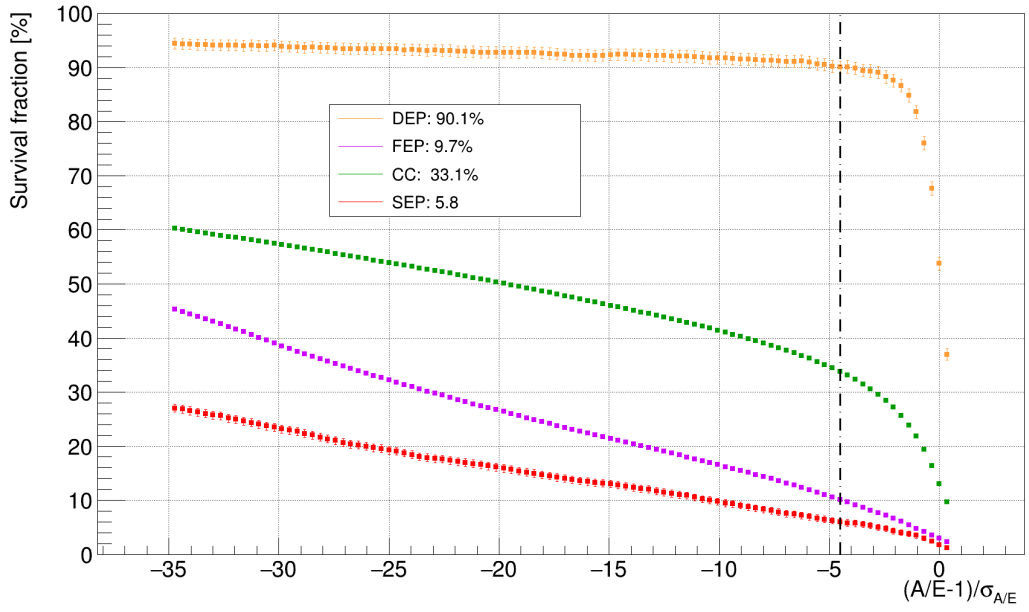

Figure 5.32: The PSD survival fractions for the top scan with a ^{228}Th source.

As it can be seen in figure 5.33, the DEP region on the side measurement shows an additional background line of the ^{228} Ac decay at 1588.2 keV. This line makes the survival fraction calculation of the DEP difficult and increases the number of rejected events. Hence, as seen in figure 5.34 the survival fraction suffers compared to the top measurement.

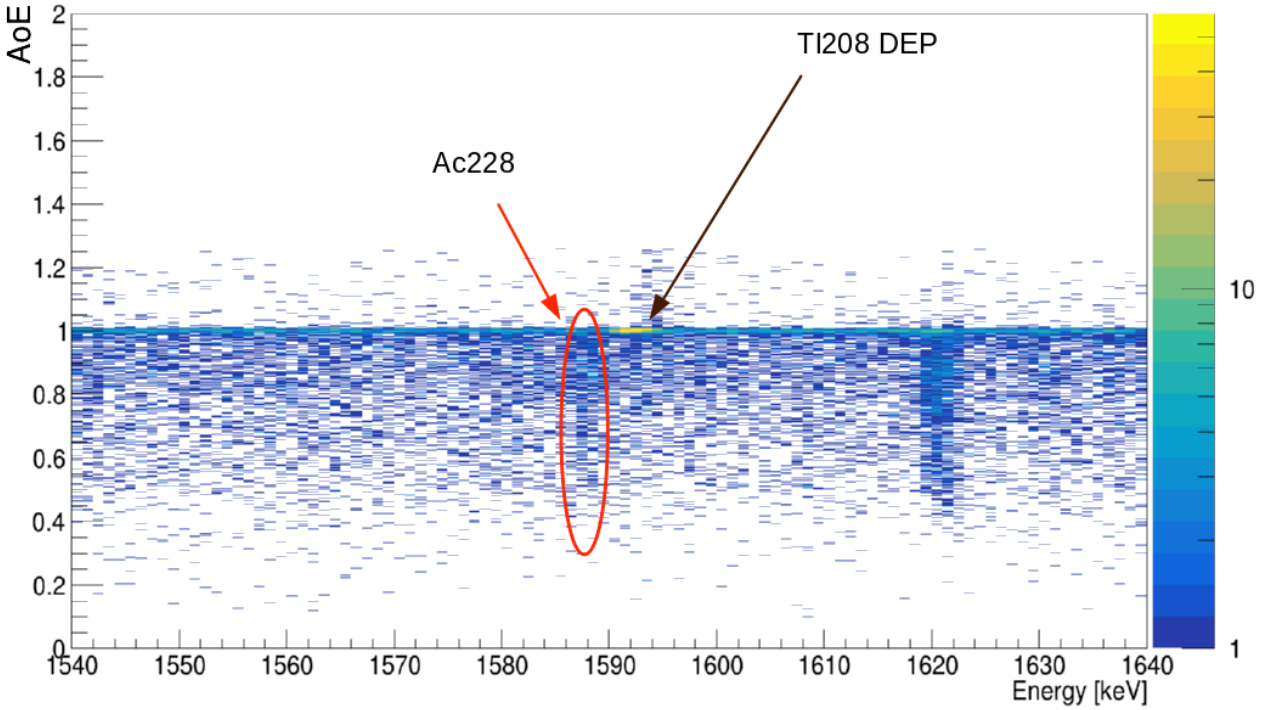

Figure 5.33: The DEP energy region for a side scan with a ^{228}Th source. A background line from the ^{228}Ac decay at $1588.2\,\mathrm{keV}$ can be seen, indicated by the red ellipse.

However, the overall PSD performance is good for this ICPC detector type and a MSE rejection based on the A/E parameter can be applied.

The side scan with a ^{228} Th reveals another feature of the ICPC detector pulse shapes.
In figure 5.35 the A/E in dependence of the risetime of events with $4.5\,\sigma$ of the DEP is shown for the top and for the side measurement.
Two distinct populations at different risetime regions can be seen. The events with the lower risetime have a slightly bigger A/E value compared to higher risetime events. These populations are associated with the lower or the upper detector region respectively. If a SSE originates in the lower region closer to the p+ contact, the risetime is lower. These events migrate through a slightly different weighting potential compared to top events, resulting in an increased A/E. This shift in A/E could be potentially dangerous for $0\nu\beta\beta$ searches since the MSE rejection

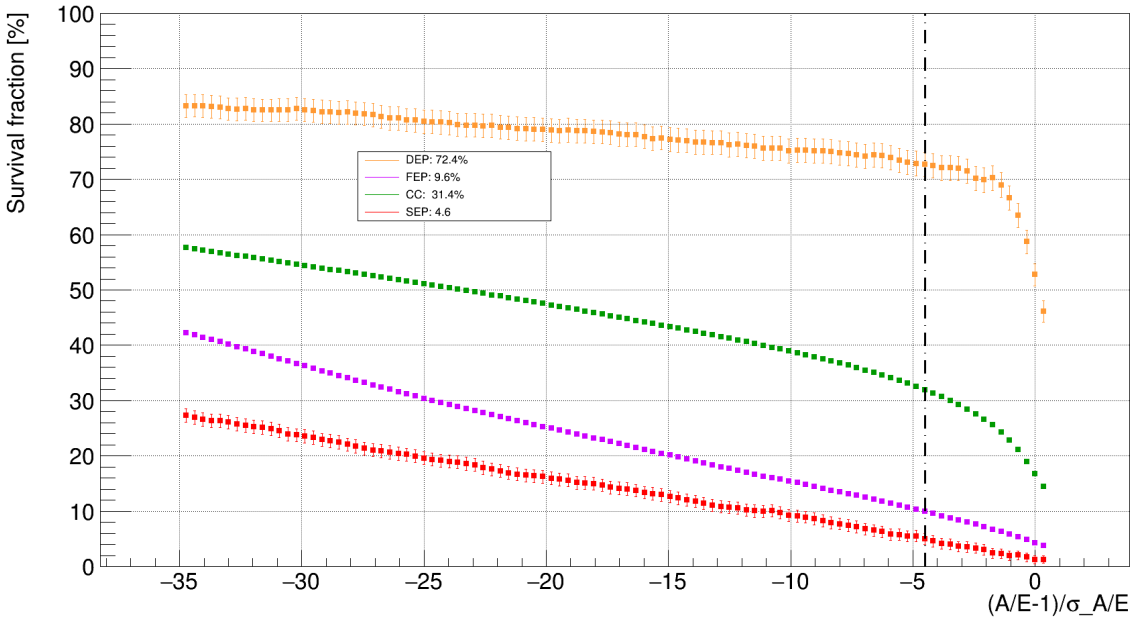

Figure 5.34: The PSD survival fractions for the side scan with a ^{228}Th source.

performance could suffer. An event which would be discarded if it originated in the upper detector part could be accepted if it originated in the lower part. The PSD acceptance is therefore risetime dependent.

This risetime dependence has not been observed with BEGe detectors. Their smaller geometry and the non existent bore hole make the risetime distribution more homogeneous. This effect is unique for ICPC detectors and has also been observed in detector models of other vendors. More details on this effect can be found in [CAS20]. One approach in order to correct for this effect is to perform a drift time correction. The drift time is the actual time of the charge carrier drift. It is the time difference between 0% and 100% of the measured charge pulse. If this drift time can be computed, the A/E value can be corrected by a factor inversely proportional to the drift time. This also implies that this correction is highly dependent on the noise level. If the noise is to high, an accurate drift time estimation is not possible. On the other hand is a high noise level reducing this drift time dependent A/E shift, since the A/E uncertainty is also dependent on the noise level. This effect will be covered if the noise is to high.

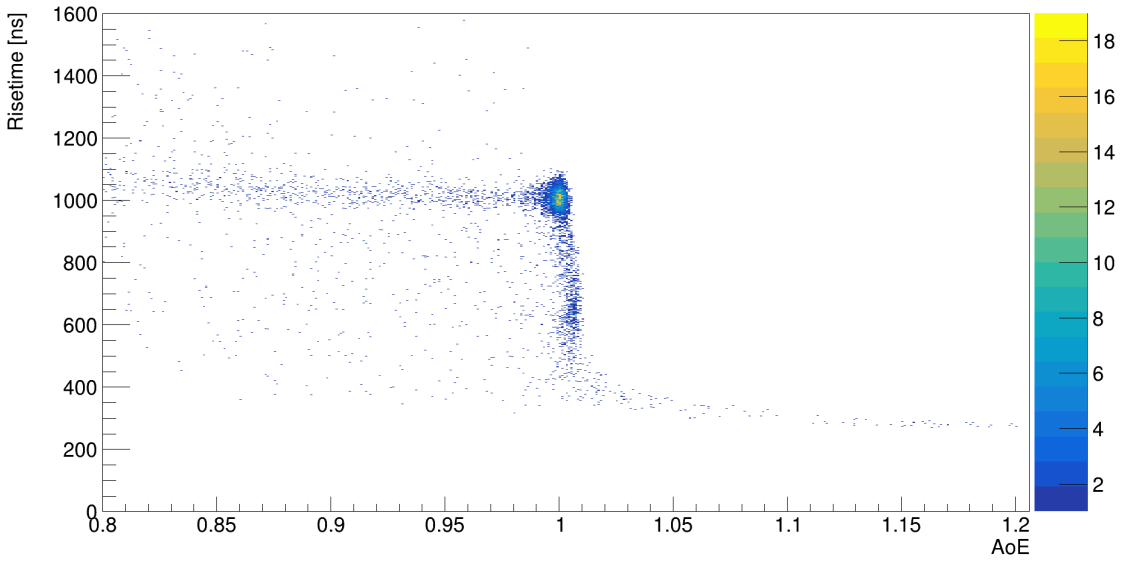

(a) Top scan.

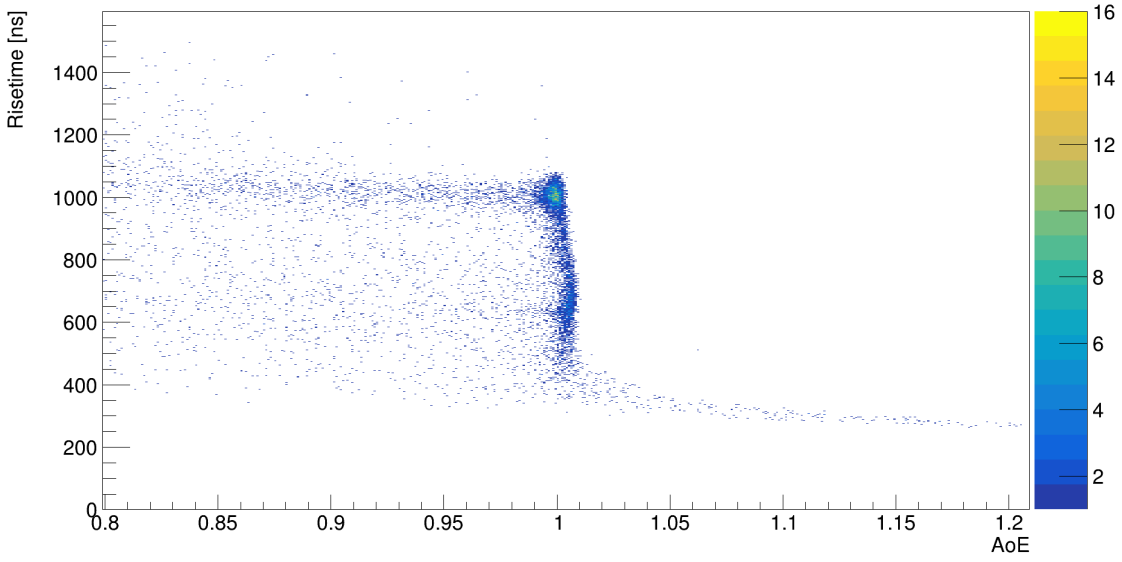

(b) Side scan.

Figure 5.35: Risetime dependence of the A/E distribution. It can be seen that the A/E are slightly higher for shorter risetimes.

5.7 Data from GDL

In February 2018 the ORTEC ICPC detector has been brought to the Gran Sasso laboratory and has been installed into the GDL facility. The first measurements depicted the monitoring of the leakage current (LC) over a time period of 8 days in total. After the LC measurements a PSD performance test in LAr with a ^{228}Th source has been performed.

5.7.1 LC measurements

Before a high voltage has been applied to the detector a reference LC has been measured. After that the LC has than be measured repeatedly with and without a radioactive source and before and after refills of the Dewar with LAr. The measured values for the LC are listed in table 4

Date [2018]	**Before Refill**		**After Refill**	
	U [V]	I [pA]	U [V]	I [pA]
05.02	-0.15	-75.0	-0.01	-5.0
08.02	-0.194	-97.0	-0.028	-14.0
09.02	-0.183	-91.5	-0.03	-15.0
12.02	-0.163	-81.5	0.002	0.1
12.02 With Source	-	-	-0.039	-19.5
12.02 Without Source	-	-	-0.027	-13.5
13.02	-0.171	-85.5	-	-
13.02 Without Dewar pipe	-0.174	-87.0	-	-

Table 4: The Leakage current measurement.

The goal of this LC measurement was to observe if the detector suffers from an increasing LC when deployed in LAr. Especially the irradiation of the detector with a radioactive source could possibly lead to an increased LC as this effect has been observed with BEGe detectors before [HBGS10]. From this data a the effect of a nearby source on the LC is in the order of 5 pA. The thermal effect due to the steady loss of evaporating Argon has in contrast a much higher effect in the order of 80 pA. The deviation in LC also kept rather stable over the course of the measurement. From this small time period no increase in LC could be observed over time.

5.7.2 PSD Performance

After the LC measurements the detector has been further deployed in LAr while being irradiated with a ^{228} Th source and its performance has been analyzed. Again, of special interest is hereby the energy resolution and the PSD performance. Both analysis have been done using the same algorithms as described above. Overall a decent energy resolution of ca. 3.3 keV at 2000 keV could be achieved. This is a little worse compared to the data discussed above. This difference

could originate in the different read out settings. Figure 5.36 shows the resolution curve of a trapezoidal energy estimator.

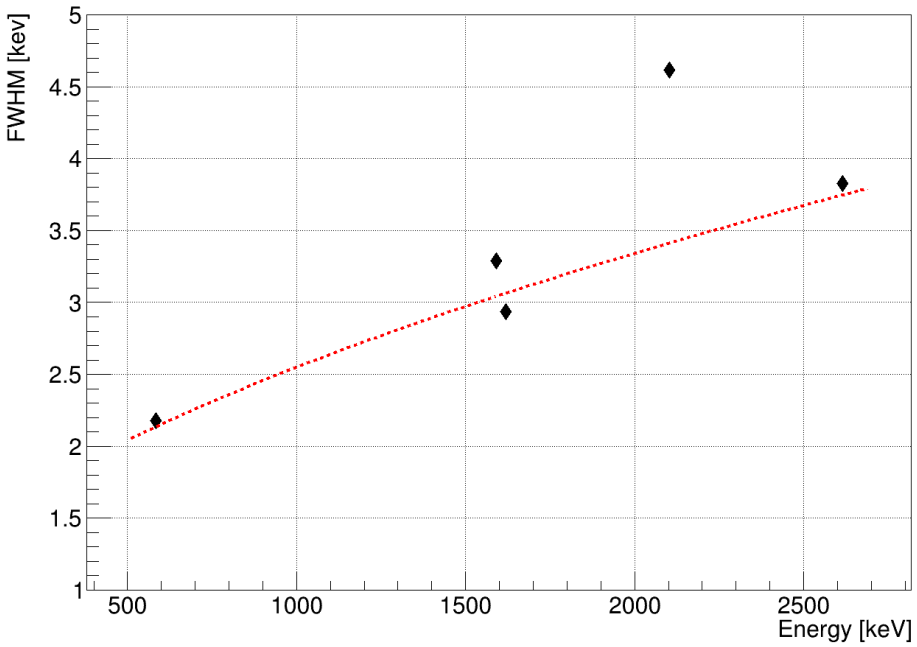

Figure 5.36: The energy resolution curve for the GDL run in LAr.

The A/E has also been calculated and the corresponding PSD survival efficiencies have been determined. Figure 5.37 shows the resulting A/E spectrum and 5.38 shows the received PSD survival efficiencies. It can be seen that the A/E distribution is smaller compared to the previous, first run in vacuum.

Originally it was also planed to perform a dedicated measurement in LN_2. Especially the temperature dependence of the charge collection would be of interest. This measurements unfortunately suffered from a too high LC and an analysis could not be done.

5.8 Conclusion

In this chapter, the analysis routines that have been used for the detector performance test as well as for the α surface event analysis have been introduced.
First performance tests of an ORTEC ICPC detector have been successfully carried out and evaluated. Overall, the ORTEC ICPC detector showed a very good performance. The energy resolution is not outstanding, but still can be improved by the optimization of the energy

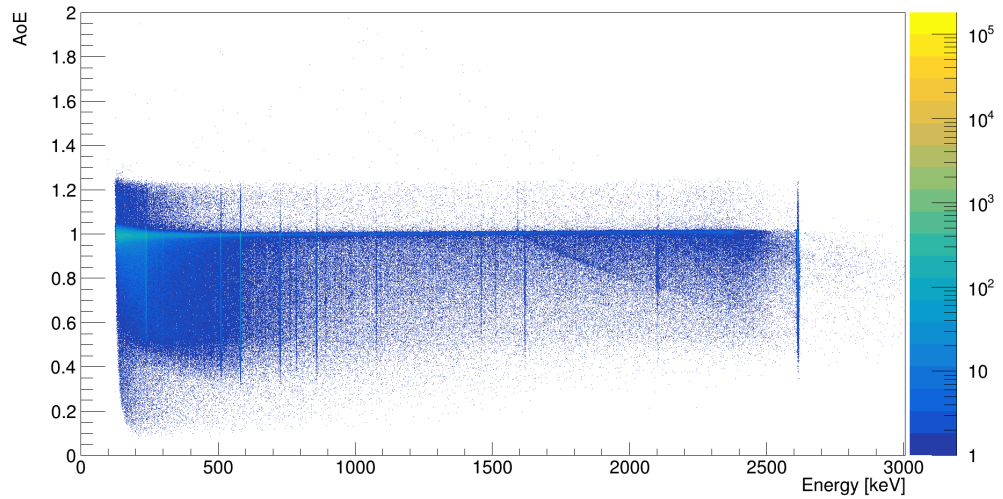

Figure 5.37: The A/E spectrum for the GDL run in LAr.

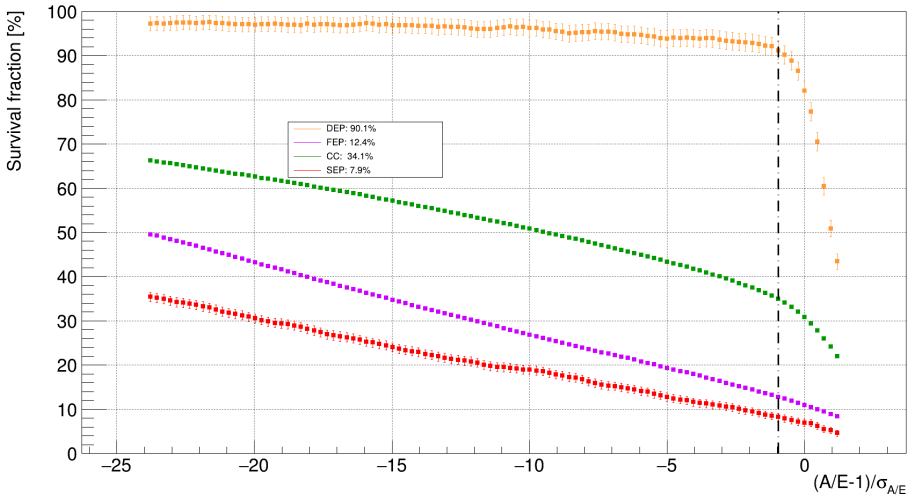

Figure 5.38: The survival efficiencies for the GDL run in LAr.

estimators and especially by the application of a drift time correction to the energy. The A/E MSE rejection also showed a very good performance, making the ORTEC ICPC detector design promising for $0\nu\beta\beta$ experiments.

Furthermore, the existing DCR PSD parameter has been refined in order to include an energy correction. Therefore the slope of the waveform tail has been calculated and normalized by the energy of the event. This makes the resulting DCRn parameter independent of the energy and a direct comparison of the fraction of the delayed charge recovery can be made.

6 The TUBE Campaign

The previous characterization tests focused on the general performance of the detector in terms of energy resolution, dead layer homogeneity and gamma background discrimination. Another background source within the LEGEND-200 setup will originate from external α sources. The Passivation Layer (PL), a only few monolayers thick layer dividing the p+ read out contact from the n+ high voltage contact, is a vulnerable surface to α penetration and the response of the new Inverted Coaxial detector type has not been investigated prior to this work.

In this chapter, the special α surface characterization measurements, carried out with the TUBE setup located at the Technische Universität München (TUM), will be introduced and the response of the detector, as well as its pulse shape discrimination ability to α events will be analyzed. It will be shown that the α particles, which penetrate the PL, show a radial dependent behaviour. The measured energy decreases with increasing distance to the p+ contact and the decay time of these pulses increase with increasing distance. Also the A/E PSD behaves differently compared to gamma events interacting in the bulk of the detector. This may introduce background at the $Q_{\beta\beta}$, that is insensitive to the established A/E PSD based background rejection. However, the analysis of the pulse shape of the α events, and especially the decay of the signal, will show that a complementary PSD parameter, the so-called DCRn parameter (see section 5.4), provides additional information and enables the application of a multivariate cut procedure to remove these event types. This procedure has been developed in this work.

The origin of the delayed charge recovery effect and the energy degradation is however still not fully understood yet. Within this work, different models of possible energy degradation mechanisms and delayed charge recovery will be tested. It will be shown that the current approaches to model the DCR effect are insufficient and a deeper understanding is needed.

It will also be shown, that the response of the detector to the α events is highly dependent on the incident position of the α event. This dependency effects the measured energy and the pulse shape of the α events. The energy can degrade down below the energy threshold of this measurements, depending on the radial incident position. The bigger the distance to the p+ contact (detector center), the higher the degradation, i.e. the lower the measured energy. Also the decay time (and therefore the DCRn) of the measured current pulse shows a radial

dependence. The bigger the incident radius, the longer the decay time of the signal pulse. This behaviour has not been observed in previous measurements so far. As discussed in chapter 5.4 the response of the PPC detector PONAMA I in the TUBE setup showed an increasing DCRpz with increasing radius, and a decreasing energy close to the p+. The observed energy dependence is contrary to what has been observed wit the ICPC detector, as it will be shown in this chapter. First models of this effect use surface charges, that are localized on the PL, as the source of this delayed charge recovery and the different signs of the charges create the different radial dependencies. However, the distorted pulse shapes have not yet been fully understood and further surface measurement setups are being built at different institutes at the time of this writing.

6.1 The TUBE Setup

In the following the TUBE setup will be introduced in detail. The TUBE setup is a custom build surface scanning system, made by the workshop of the TU Munich. This setup has been used on two measurement campaigns with two other detectors of different type before. The first campaign has been done in 2013 in order to scan and investigate the passivated groove of an CANBARRA (now MIRION) BEGe detector. As shown in [Ago13], also MIRION BEGe detectors show a degradation of the measured pulses for events, that originate in the PL of the groove. In 2016 the MAJORANA collaboration used the TUBE setup to investigate the α response on the ORTEC PPC detector PONAMA I. The results of the 2016 scan are reported here [Gru17] and [AAIB+20], Compared to the previous campaigns, the TUBE setup has been slightly modified. A schematic diagram can be seen in figure 6.3. First the collimator diameter has been enlarged from 1mm to 2mm in

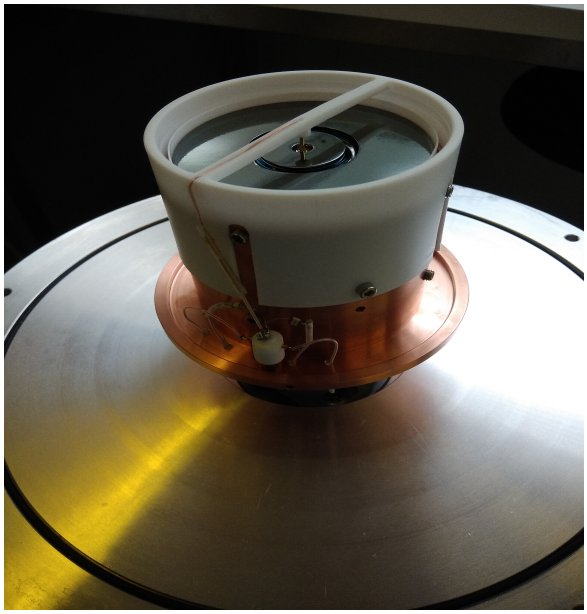

Figure 6.1: Picture of the detector inside the holder.

order to achieve a higher count rate. As a trade-off the incident position deviation enlarges as the collimator diameter enlarges. On the other hand the detector holder needed to be adjusted, since an ICPC detector is in general bigger then a PPC or BEGe detector. The other parts of the setup remained unchanged. Figure 6.3 shows a drawing of the TUBE setup. In general the TUBE setup is a vacuum vessel made out of stainless steel in which a bare detector can be mounted upside down (i.e the p+ contact is facing upwards) and a collimated radioactive source can be moved along the upwards facing detector surface. The detector is connected to a cryostat with a cold finger which goes, together with the readout and high voltage cables, through a feedthrough at the bottom flange of the vessel. Another feedthrough is located on the side of the vessel for the source holding and moving system.

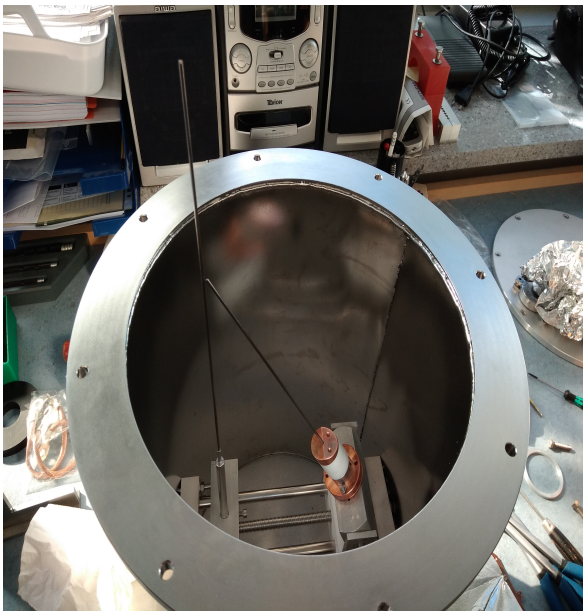

Figure 6.2: Picture of the TUBE outer vessel and the collimator inside.

The rail on which the source is mounted can be rotated by a spindle outside of the vessel, such that the source can move horizontally along the detector axis. One turn of the spindle outside corresponds to a horizontal movement of 1.5 mm. This way the source position can be calculated in numbers of turns of the spindle. The vessel is also connected to a vacuum pump such that pressures of as low as 10^{-6} mbar can be achieved. The detector holder is made out of Copper and encapsulates most of the detector except for the bottom surface. A Teflon spacer is set between the detector and the holder. On top of the holder there is a Teflon bar that serves as a holder for the golden, spring mounted readout pin and also guides the read out cable around the detector housing. The whole holding setup is again encapsulated by a Copper cup which has a 3 mm wide slit for the incoming α particles.

The used collimator is a 50 mm long cylinder with a 2 mm collimation diameter and it consist out of three components. It is mounted to the rail system and is tilted by an angle of 66°. The

top part of the collimator is made out of Copper and encapsulates the source. It is is connected to the middle part, a 35 mm long Teflon collimator with the same diameter. The end of the collimator is again made out of Copper. The last part shows a beveled edge according to the collimator angle such that the collimator can be aligned tightly to the infrared shield between the holder and the collimator. The source that has been used in this campaign is a ^{241}Am α emitter with a nominal activity of 40 kBq. This collimator design and the tilt of 66° leads to an ellipsoidal illumination on the detector surface with a diameter of around 3.8 mm along the detector axis. The read-out pin and the the Teflon bar, that it is mounted at the center of the detector, is partially blocking the line of sight of the incoming α particles. This shadowing effect can be seen in the data.

The preamplified output signal is digitized with a sampling rate of 100 MHz by a Struck FADC. The data acquisition software is a c-based software stack written by T.Kihm. In addition there is a plastic scintillator panel positioned on top of the TUBE vessel that serves as a Muon veto. It is also connected to the FADC and is read out for each Germanium trigger. A time coincident plastic scintillator trigger can be used as a Veto in the offline analysis, reducing the rate of Muon induced background. For each run the data has been recorded and stored to a local hard-drive. Afterwards the data has been transmitted to the Max-Planck servers in Heidelberg and all further data processing and data analysis has been performed there. The data processing, data selection and data analysis has then been carried out following the procedures described in the methods chapter 5.3

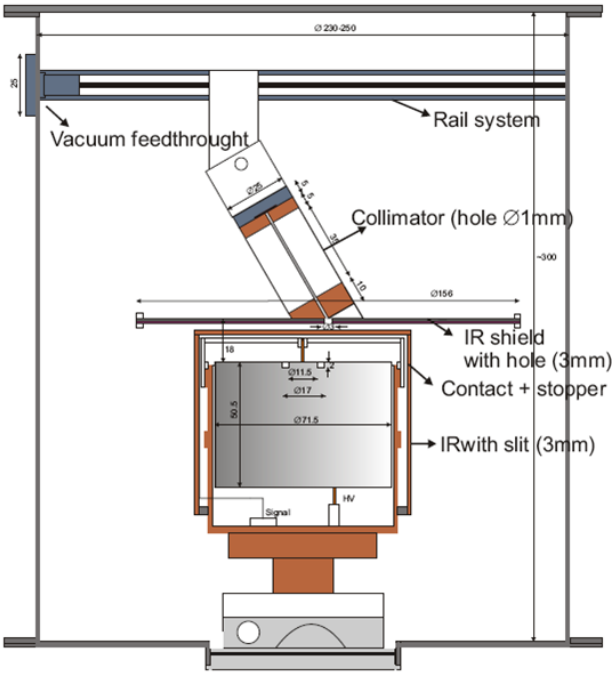

Figure 6.3: Schematic view of the TUBE setup, taken from [Ago13].

During the campaign it turned out that the correct alignment of the collimator and the shielding plates is not trivial. After the first runs an inconsistent response to the α radiation between the two sides of the detector has been measured. Therefore the TUBE setup has been reopened and the copper plate on which the collimator stands was found to be tilted. Due to this tilt one screw (which is fixing the reflective Mylar foil) had contact to the holder of the detector. When the collimator is moved forward, the screw exceeds the detector holder and loses contact and the plate tilts further. If the collimator is turned back, the screw jumps back and the collimator tilts back. This led to different angles and an inconsistent position determination. The setup has been realigned afterwards and further scans has been taken. This work will focus on the data taken after the realignment, especially the scans on one detector side between the p+ contact and the groove. Here the source position can be validated directly on the detector response, as it will be discussed in the next section.

6.2 Data Taking

The first intermediate goal in this campaign was to measure the p+ contact response to α radiation and therefore also to crosscheck the correct alignment. With the thickness of the p+ contact of 0.3 μm (value provided by the vendor), serving as a small dead layer, the measured α peak is expected to have a reduced energy of ca. 100 kev. From geometrical projections (i.e. giving the collimator diameter of 2 mm, the length of the collimator of 50 mm) and the nominal activity of 40 kBq of the source and the source geometry, a count rate in the order of around 0.3 mHz (ca. 1000 events per hour) is expected to reach the detector surface. However, the count rate is expected to be slightly lower for source positions close to the p+ contact since the Teflon bar that holds the readout pin is blocking a part of the α particles. On the n+ surface the count rate is expected to vanish since the n+ surface with an estimated thickness of 0.7 mm blocks the α particles entirely.
The validation of a correct alignment of the setup can been done by analyzing and comparing a dedicated background run, i.e a run on which the source was pointed on the n+ surface, and a dedicated α run on which the source was pointing on the p+ contact. The spectra of both runs are then compared to the expectation of runs with and without an α source. These expectations can be summarized as follows:

alpha p+ run: The run with the α source aiming on the p+ contact is expected to show a measurable α peak, since the 0.3 μm thin p+ contact is not thick enough to block the α

particles efficiently. The emission spectrum of the ^{241}Am decay consists mainly out of three lines with different intensities. Table 8 gives an overview of these lines.

Also, since the α particles interact on or very close to the p+ contact, a sharp and fast rise of the rising edge of the pulse is expected. This pulse shape should be different from bulk events and a narrow, high A/E distribution for the α should appear well above the SSE line. Overall the α events are expected to be highly visible and distinguishable in terms of energy, A/E and risetime.

Energy [keV]	Intensity [%]
5388	1.66
5222.8	13.1
5485.6	84.6

Table 5: Nominal energies and intensities of the strongest ^{241}Am emission lines.

The background run: Contrary, the background run is expected to only show gamma lines and their Compton Continuum over a linear muonic background. A comparison of the energy spectra and the A/E distribution of the two dedicated runs can be seen in figure 6.4 and figure 6.5. As expected, the α events are clearly visible and the distributions follow the expectations.

Before the investigation of the α surface events will be carried on, the background inside the TUBE setup should be discussed a bit more detailed. The view on the background spectrum in the top panel of figure 6.4 reveals that there is a large amount of radioactive background sources within the TUBE setup, visible as a forest of gamma lines in the energy range below 2.6 MeV. This high background event rate was not anticipated and not wanted and makes an analysis of the α events harder then expected. Additionally a large fraction of the muonic background remains even after the Muon veto cut. This can be seen in figure 6.6. The muon veto cuts a fraction of $\sim 11\%$ of all events that survive a pile up rejection. Especially at high energies it can be seem that there is still a high fraction of muonic events surviving the muon cut. This can be explained on the one hand by the small solid angle that the one plastic scintillator panel covers, leaving a large area vulnerable, and on the other hand by a not optimized read out setup of the panel signals. The measured panel signals show a very fast rise and decay in the order of ns which makes an offline analysis of the signals difficult. In future campaigns the amplification of the panel signals could be optimized and especially the decay of the muon panel pulses should be extended.

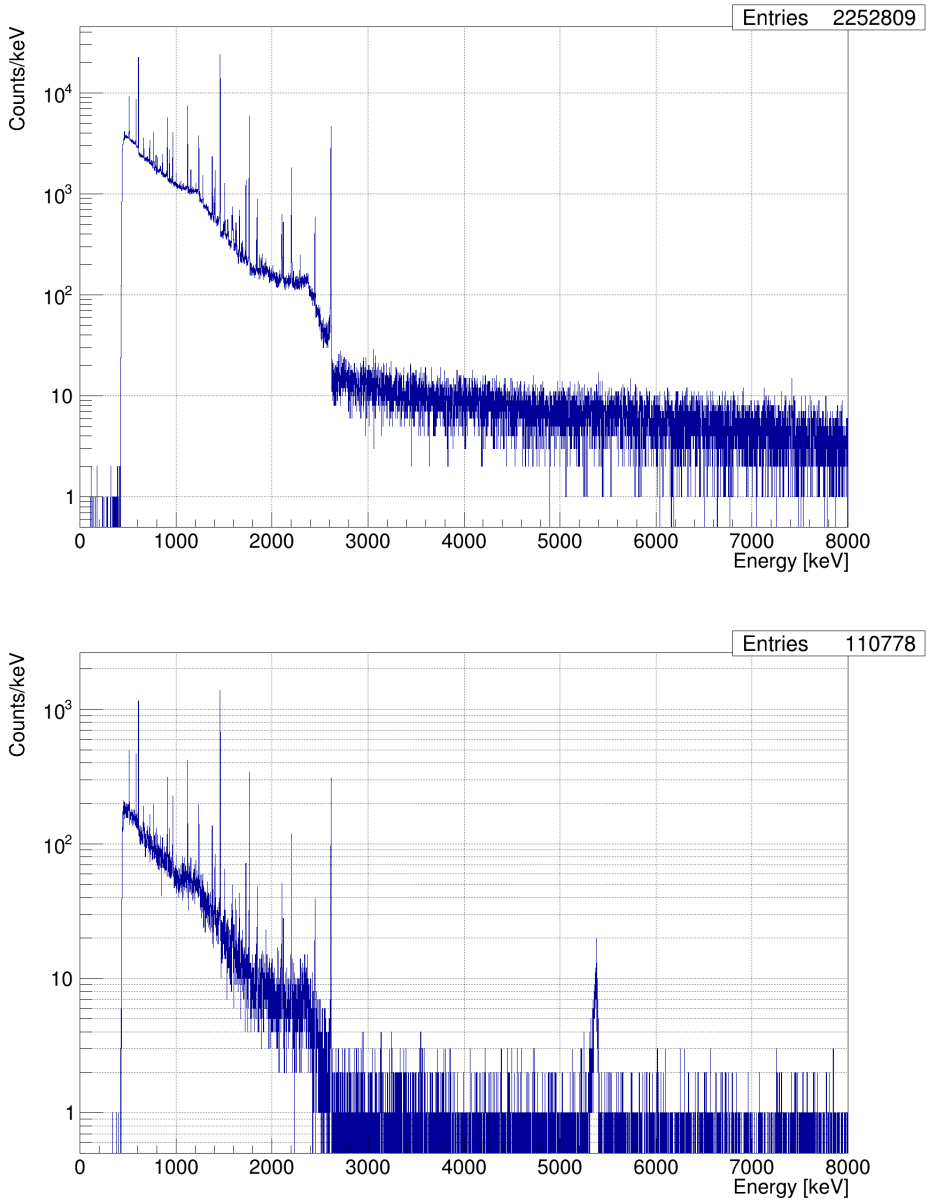

Figure 6.4: The energy spectrum of a background run (top panel) and an α run aimed at the p+ contact (bottom panel). The α distribution is clearly visible as a peak within the continuous energy spectrum above the 2614.5 keV line.

The comparable high background rate makes an identification of α particles below the gamma line of 2614.5 keV very difficult. Excess α particles in this energy region are fully covered and an identification by spectral analysis becomes impossible. Only above the highest line of the ^{208}Tl decay α particles are visible as an excess above the linear background.

Of special interest for the PSD parameters are the DEP and SEP regions from the ^{208}Tl decay at

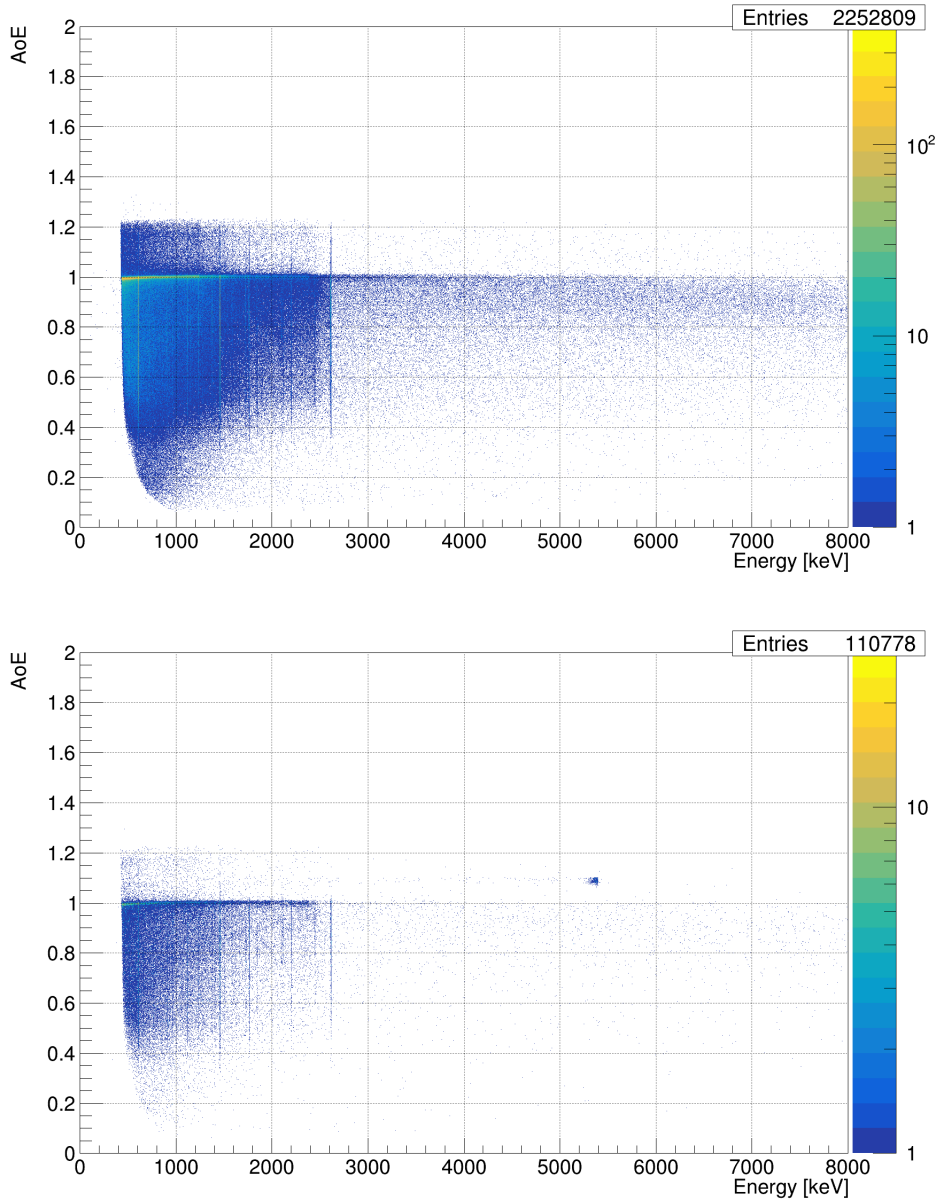

Figure 6.5: The A/E distribution against the energy of a background run (top panel) and an α run aimed at the p+ contact (bottom panel). The α distribution is clearly visible as a population with a high A/E above the Single Site Band at 5.3 MeV.

1592 keV and 2103 keV respectively. The evaluation of the pulse shape performance is usually carried out on these lines (see chapter 5.3.5), since the DEP serves as a proxy for SSE events and the SEP, as its antagonist, as a proxy for MSE events. In figure 6.7 a closer look on the DEP region is shown. Unfortunately, the DEP is covered by several background lines, which makes a proper evaluation of the cut values impossible. Therefore, the MSE rejection efficiency of the A/E cannot be determined out of this data. Fortunately though, the efficiency is not

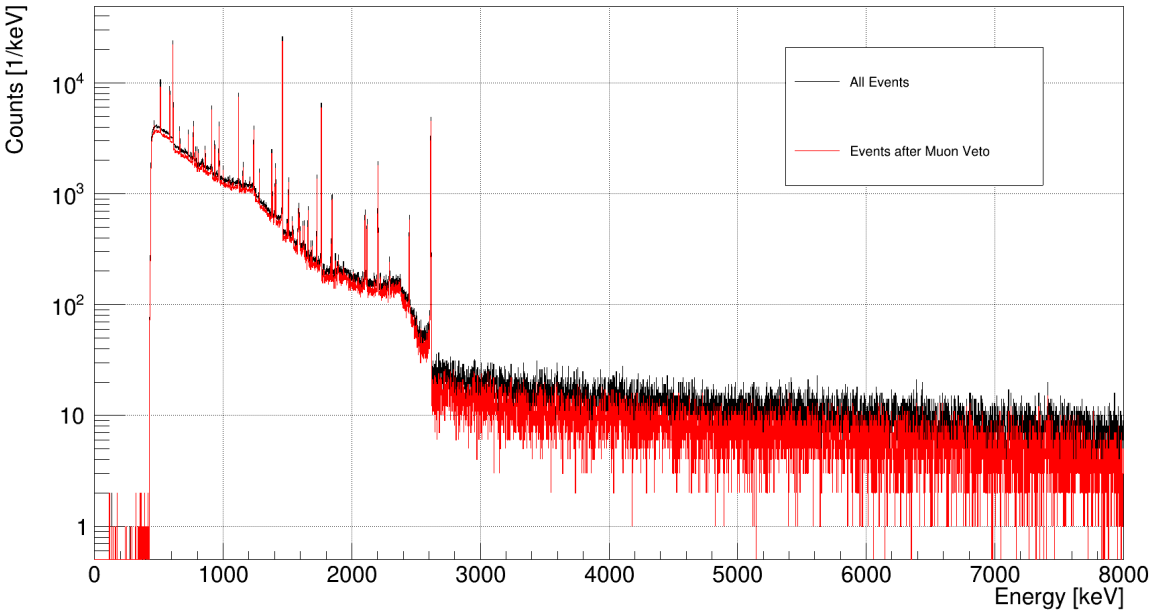

Figure 6.6: The measured background spectrum before (black) and after (red) the application of a muon cut. A high fraction of muonic indcued events survive the muon cut.

needed for the analysis of the α events on the PL and the A/E will be only used as a crosscheck.

6.3 The Passivation Layer Scan

It has been shown, that α particles emitted by the ^{241}Am source are able to penetrate the detector surface inside the TUBE setup. The next step is to perform a detailed, radial scan along the PL. In this section the detector response to the α particles between the p+ contact and the groove will be discussed and evaluated. This discussion will be structured in three different parts; **The observation** and the detailed description of the measurement and the detector response, **the evaluation** of the old and new PSD parameters on the collected data and finally **the comparison** of the collected data to different models.

6.3.1 Observation

The PL-scan is a collection of individual runs at different source positions on the detector surface, i.e the α source is moved for each run separately. On the first run, the source has been moved to a position such that the n+ contact close to the groove will be illuminated. This means that the detector should not see any α particles and the first appearance of α events in

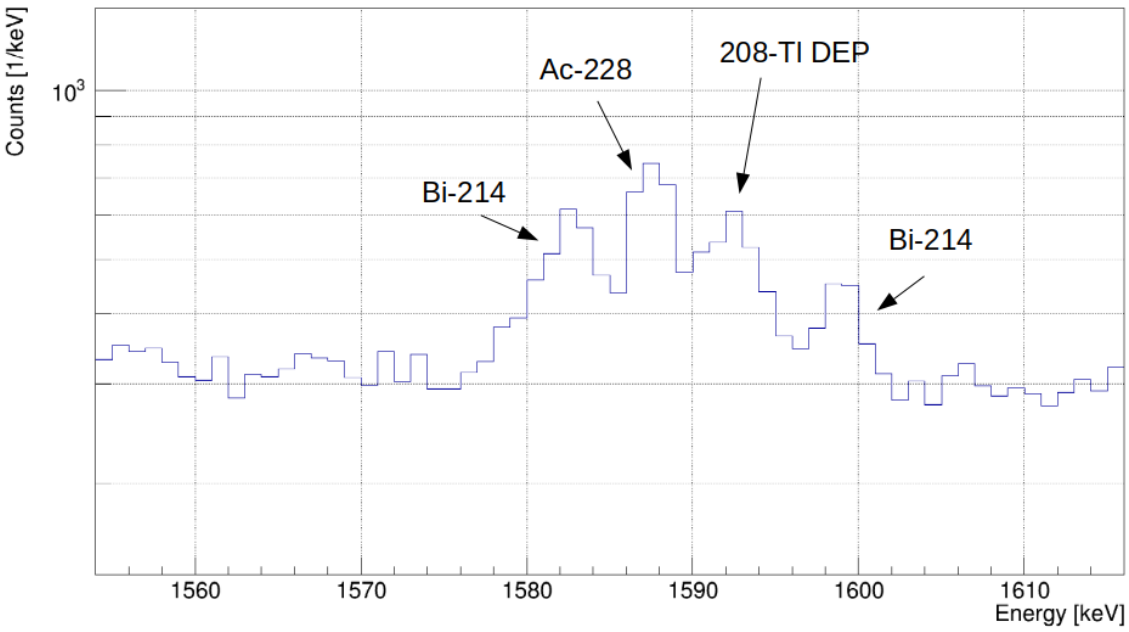

Figure 6.7: The energy spectrum around the DEP. It can be seen that the DEP is covered by several background lines, hence a PSD efficiency determination based on the DEP is not possible.

later runs can be used as a position validation. On all following runs the source is moved in 1.5 mm steps along the detector axis. The lifetime of the individual runs can vary depending on the daytime at which the run was taken (over night runs have higher lifetime of usually $>$ 12 h). Otherwise it was tried the keep the lifetime at around two hours for each run.

The runs can be split into two separate groups which illuminate the left and right side of the detector. The main difference between the detector sides is the incident angle of the incoming α particle in relation to the p+ contact. On the left side the incoming beam is oriented towards the p+ contact whereas the on right side the α particles move away from the p+. This also leads to the already mentioned shadowing effect of the read out pin on the right detector side, i.e. the area on the right side on and close to the p+ contact is covered by the pin and no α particles are expected to be measured here. As it will be shown later, this effect is visible in the data.

However, the reappearance of the α signals comes later than it was expected from simulations. This discrepancy between expectation and data can either originate in an underestimation of the shadowing effect, or from a shift of the collimator when the setup passes the middle of the

detector. The latter options appears to be more likely since the collimation setup is susceptible for shifts when the setup passes the Copper detector shield.

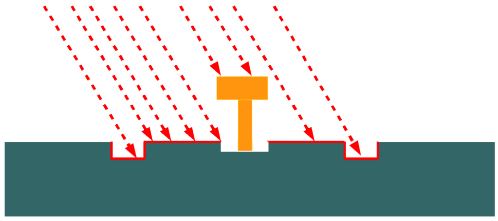

Figure 6.8: Visualization of the expected α interaction positions for an intermediate run between the p+ contact (yellow) and the PL (red). The blue cone represents the incoming, collimated αs. This is only for visualization purposes, i.e. all dimensions are not correctly scaled.

The left side of the detector however matches very well the expectation from the geometrical projections and no shadowing effect disturbs the detection of the α particles. The left side provides a reliable position dependence whereas the right side can only be analyzed qualitatively, especially in terms of the incident angle. A sketch trying to visualize the incoming α particles and the surface structures of the detector can be seen in figure 6.8. This sketch also emphasizes the sharp transition between the p+ contact and the PL and the readout pin and its holding structure that blocks the αs partially or totally especially on the right side of the detector.

A third distinct run type are the runs on which the source is pointed on the groove. It will be shown that the pulse shape of the groove events experience a chaotic behaviour especially for the A/E distribution. This behaviour is expected to occur due to the strong deformation of the electric field in the surrounding of the groove. Events interacting in the walls of the groove will behave differently than events at the bottom and in the corners and, due to the big spot size of the collimation (the spot size is bigger than the groove width) the incident position inside the groove cannot be resolved. A more detailed analysis would need higher collimated scans and therefore a different collimator. This could be done in future campaigns at different scanning setups.

In the following, the focus of the analysis lies upon the left side PL runs, without the groove runs. All these runs can be compared by several parameters like their energy spectrum, their A/E distribution, their decay time and DCR distribution and the Asymmetry parameter. For each run the α population can be clearly seen as it migrates within the corresponding parameter

space. Exceptions are the energy spectra of the runs in which the α population degrades below the 2614.5 ^{208}Tl gamma line. In these runs the α events are covered by the high background and are not distinguishable due of their low count rate. However, they are still visible in the other pulse shape parameters, since they differ from the mean bulk event characteristic.

Perhaps the most important observation that can be made is the position dependent energy degradation of the α particles proportional to the distance to the p+. The energy degrades the most for incident position far away from the p+ contact. Simultaneously the decay time rises proportional to the distance to the p+.

In the following overview diagrams (figure 6.9 until figure 6.12), the evolution of the detector response to the α particles in dependence of the incident position will be documented. All figures show the different pulse shape parameters or digital filter outputs for each run on the PL, starting from the p+ contact in the top left panels and moving 1.5 mm consecutively each following run until the groove is reached. Each of the five following figures show a different parameter, starting with the energy distribution at figure 6.9, moving to the A/E, the DCRpz, the DCRn at figures 6.10, 6.11 and 6.12 and closing with the asymmetry parameter $\mathrm{rt_a sy}$ distributions in figure 6.13.

Based on the following observations, a highly effective cut procedure could be developed which is sensitive to the α surface events. This cut procedure will be introduced in detail in section 6.4. The result of the cut, i.e. the separated α events however will already be taken to demonstrate and quantify the observed behaviour, such that the mean and the deviation of the different pulse shape parameters can be drawn as a function of distance to the p+ contact. These diagrams are shown in figure 6.14.

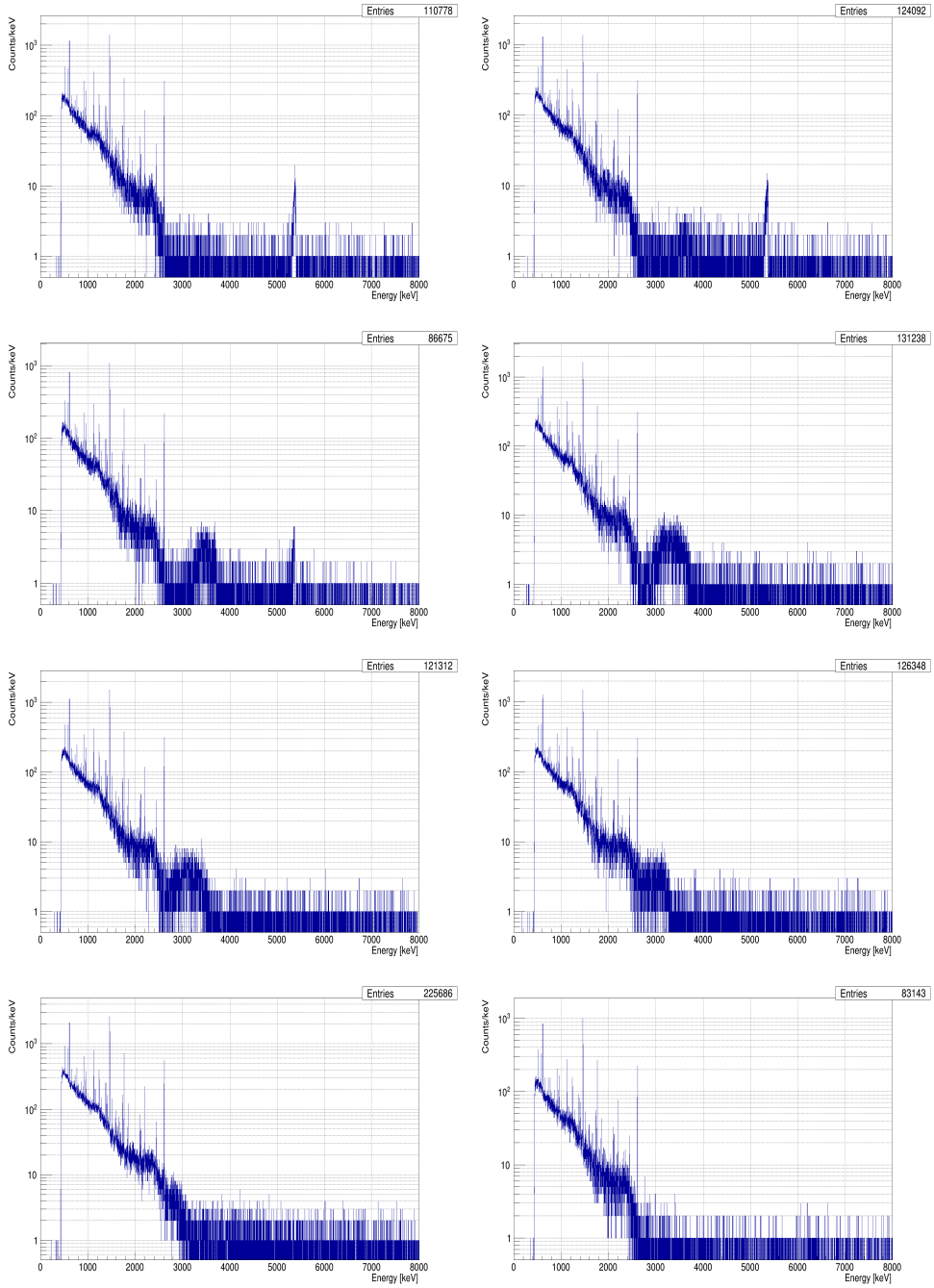

Figure 6.9: This is an overview of all spectra for each scan position between the p+ contact and the groove. It starts at the top left panel with the p+ run that was already shown before and moving towards the groove in 1.5 mm steps. The α population is visible in the energy spectrum above the gamma background of $2614.5\,\mathrm{keV}$. Below, the population is there, but covered by the background at not visible anymore.

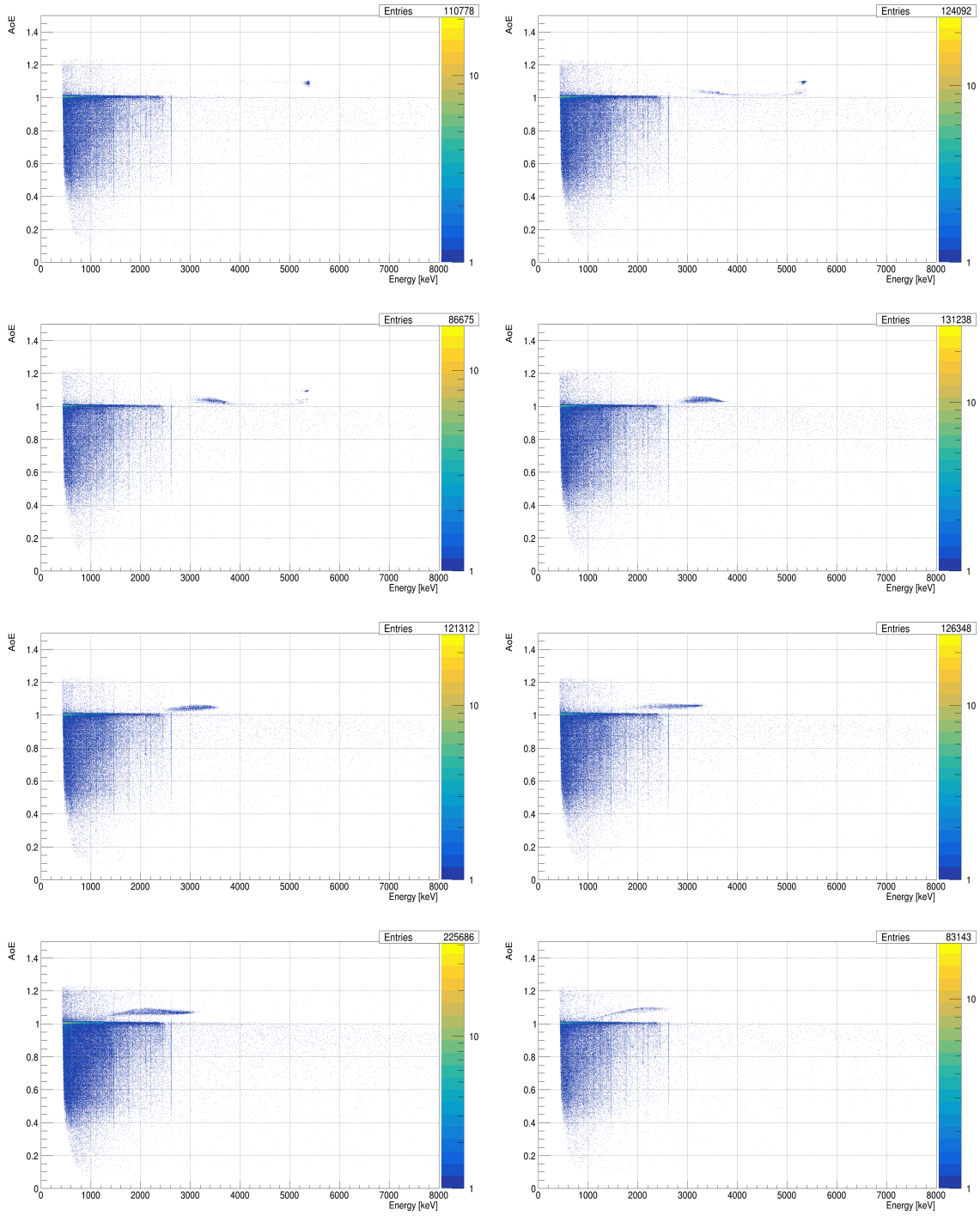

Figure 6.10: The A/E distribution for each scan position between the p+ contact and the groove. It starts at the top left panel with the p+ run that was already shown before and moving towards the groove in 1.5 mm steps. The αs are visible as a population above the Single Site Event Band for all the runs. They can be distinguished from the gamma background.

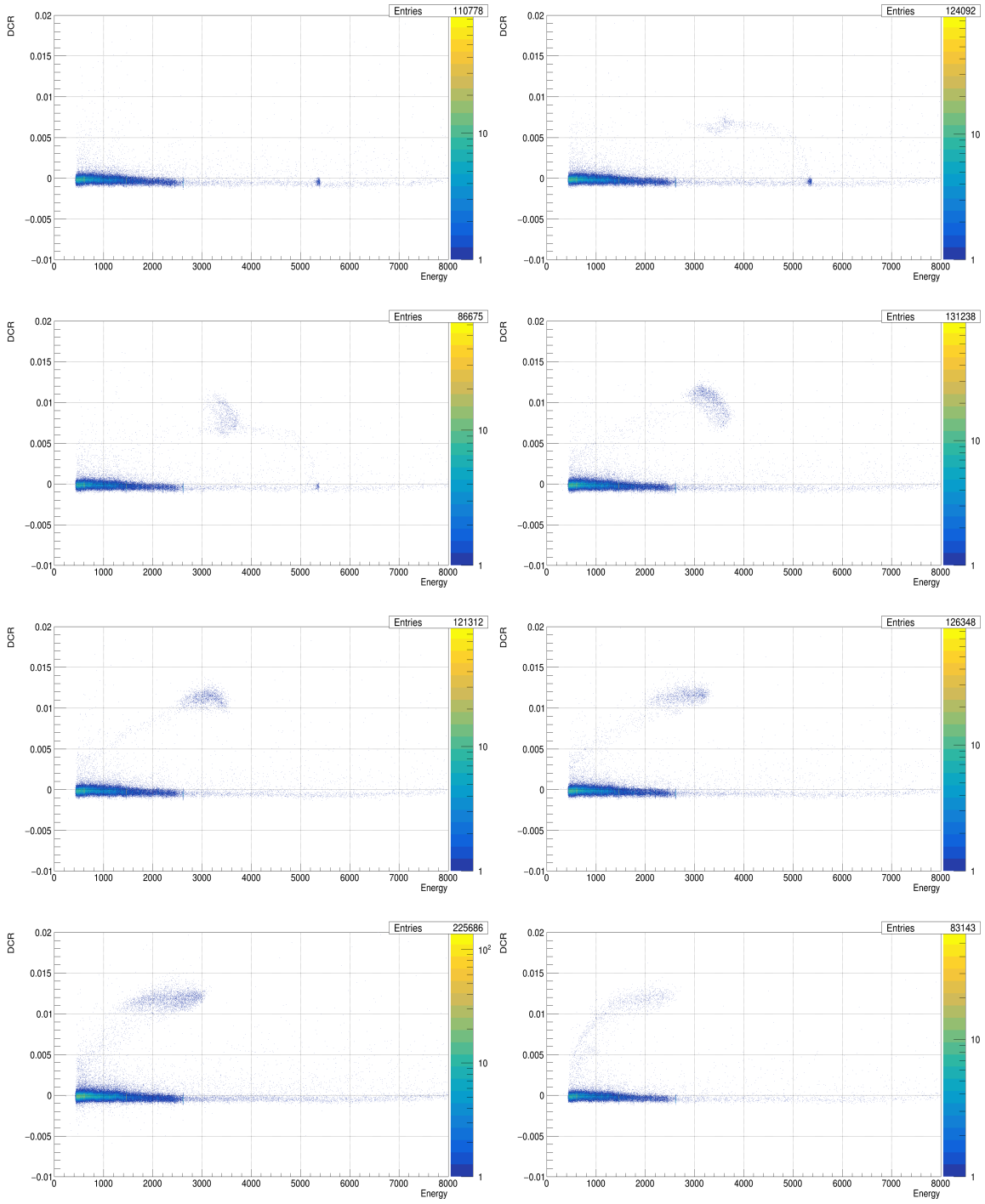

Figure 6.11: The DCRpz distribution for each scan position between the p+ contact and the groove. It starts at the top left panel with the p+ run that was already shown before and moving towards the groove in 1.5 mm steps. The αs are visible as a population above the Bulk Event Band for all the runs. They can be distinguished from the gamma background.

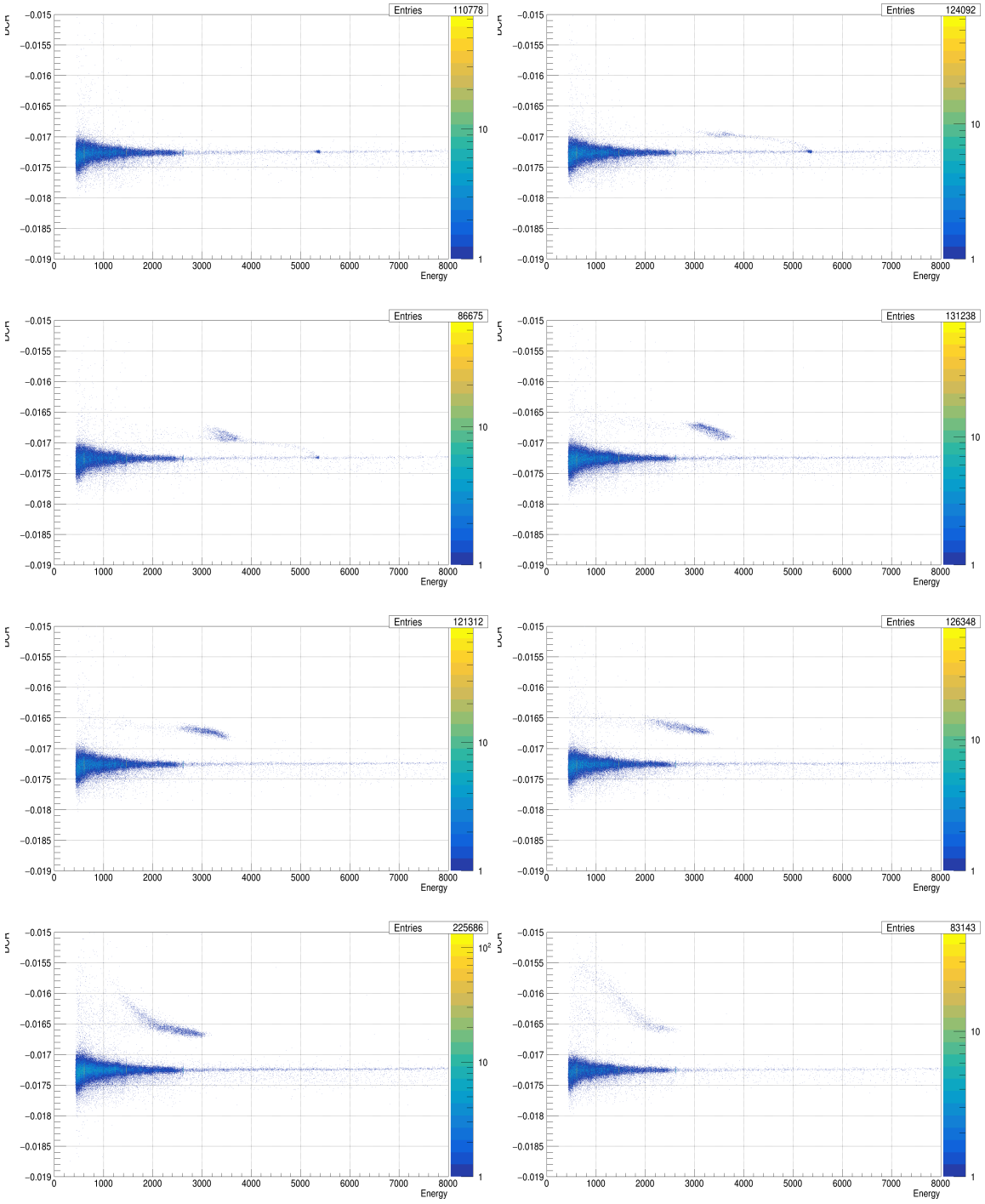

Figure 6.12: The DCRn distribution for each scan position between the p+ contact and the groove. It starts at the top left panel with the p+ run that was already shown before and moving towards the groove in 1.5 mm steps. The αs are visible as a population above the Single Site Event Band for all the runs. They can be distinguished from the gamma background.

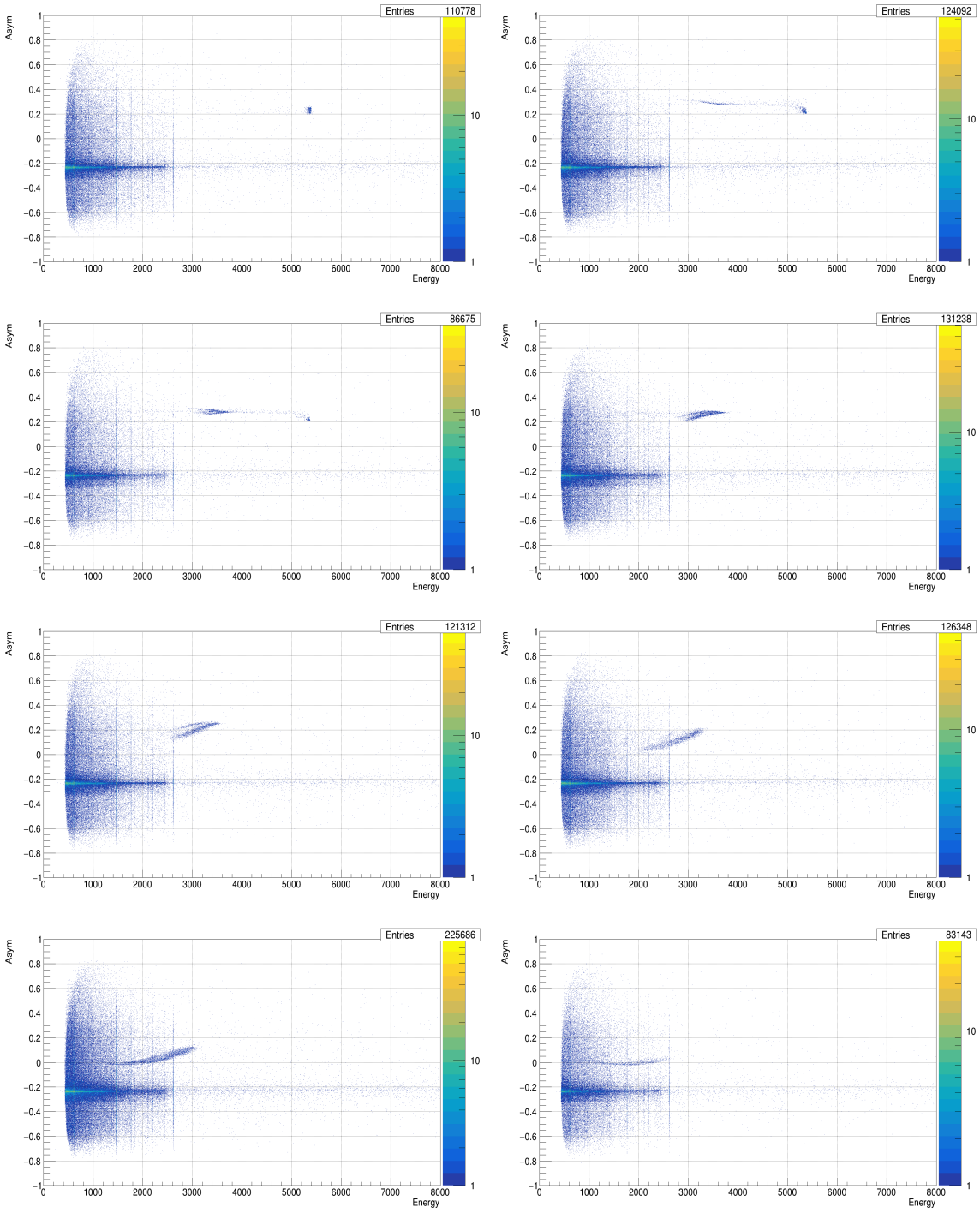

Figure 6.13: The Asymmetry parameter distribution for each scan position between the p+ contact and the groove. It starts at the top left panel with the p+ run that was already shown before and moving towards the groove in 1.5 mm steps. The αs are visible as a population above the Bulk Event Band for all the runs. They can be distinguished from the gamma background.

p+ Events:

All plots of the p+ run show a clearly distinguishable, full energy α distribution which is visible as a narrow population around 5400 keV. Overall the response to p+ α events follows the expectation and the following properties of p+ events can be observed:

- The measured energy is close to the emitted energy and is only reduced due to small dead layer effects of the boron implanted 0.3 μm contact.
- The A/E shows high, narrow distributed values since all events origin in high weighting potentials, making them easy distinguishable from bulk events.
- The DCR value and the DCRn are not distinguishable from bulk events. For p+ events there is no delayed charge recovery effect observable.
- The asymmetry parameter shows a narrow distribution at positive values. This means the rising side of the current pulse is wider then the falling side. However, these positive values can also be observed for gamma interactions and give more information about the incident position of the event than the particle type.

Interface between p+ and PL:

On panel 2 and 3 of each figure (top right and second row left) the source has been moved 1.5 mm respectively 3 mm farther away. On both run positions the α source illuminated the intersection between p+ and PL such that both surfaces were penetrated by the α particles simultaneously. Three event types can be identified. First, there are the remaining p+ events which show the same characteristic as described before. Then there is a population at a drastically reduced energy of around 3400 keV, which is associated with the PL events. The third group is a small fraction of events connecting those two populations. These events are associated with intermediate events that origin at the PL but also penetrate the p+ contact. The PL event class shows the following properties:

- The measured energy is drastically reduced by around 30 %. As soon as the α particles interact with the PL an energy degradation takes place.
- the A/E is slightly reduced but still well above the SSE line.

- The DCRpz value and the DCRn suddenly increase as the α particles interact with PL. The delayed charge recovery effect occurs and the decay of the signal gets enhanced.
- The asymmetry parameter shifts slightly to bigger, positive values. This means the asymmetry of the current pulse grows on the falling side.

The instantaneous energy loss as soon as the α particles interact with the PL is hereby remarkable. As soon as the α particles penetrate the PL a sudden drop in energy can be observed. This drop is not expected to originate from a dead layer effect of the PL, since the PL is usually formed by just a few monolayers and its blocking capability is therefore much less compared to the p+. Hence almost no energy loss is expected from a dead layer effect.

Further increasing distance:

It becomes clear that the PL events show a unique event topology and its evolution in dependence of the distance to the p+ contact can be seen in the last five panels of the figures. For each of the last panels the distance of the source to the p+ contact has been increased by 1.5 mm each. At the last panel, the edge of the PL and the groove is reached. Further runs show another variation of the detector response, which is associated with groove events and will be shown later on.

- The measured energy decreases continuously as the distance to p+ increases.
- The A/E stays above the SSE band for all the PL runs
- The DCRz parameter rises to a maximum value until it falls back again towards the bulk event distribution as the distance to the p+ increases further and the DCRpz value decreases back to the normal value.
- The DCRn parameter shows a continuous rise as the distance to the p+ increases. The values do not come back to the normal bulk distribution. This difference results from the different ways of the energy correction of those two parameters.
- The asymmetry parameter migrates towards 0 as the distance to p+ increases. The current pulse becomes very symmetrical.

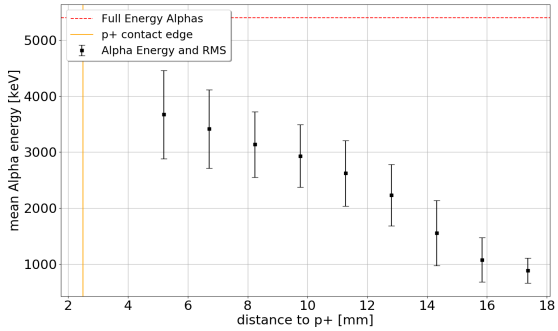

(a) The mean energy of the α PL events in dependence of the incident position. The yellow line indicate the edges of the p+. The red line indicates the mean energy of full energy α events.

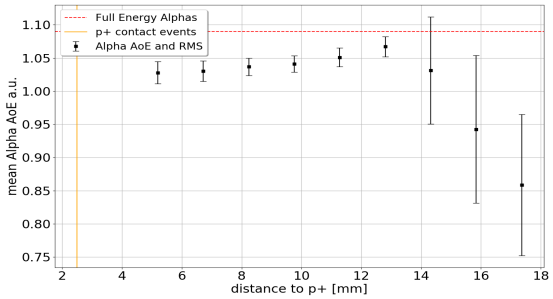

(b) The mean A/E values in dependence of the incident position. The red line indicates the mean A/E of the full energy α events. The A/E drops as soon as the PL is reached and stays constant again until the edge of the groove.

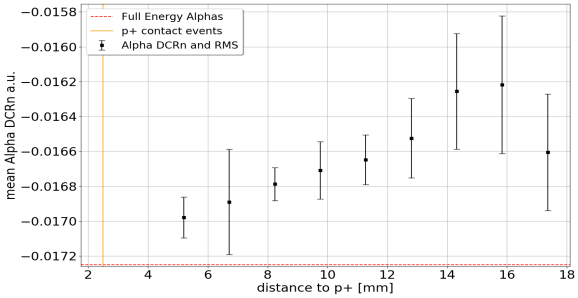

(c) The normalized mean DCRn in dependence of the incident position. The DCRn values rise constantly until the groove is reached.

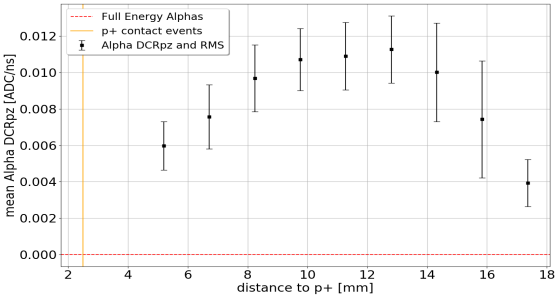

(d) The normalized mean DCRpz in dependence of the incident position. The DCRpz values rise until a maximum value is reached and decreases afterwards.

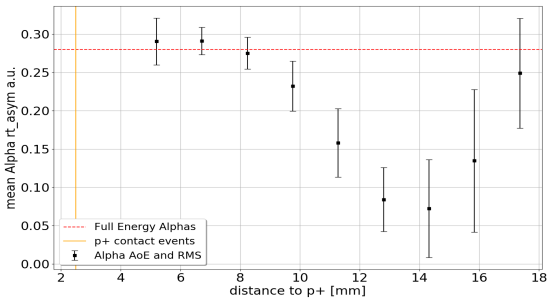

(e) The asymmetry parameter as a function of the distance to the p+.

Figure 6.14: The evolution of different pulse shape parameters as a function of the distance to the p+ contact on the left detector side. The orange line indicates the edge of the p+ contact. The red dashed line indicates the mean value of full energy α events.

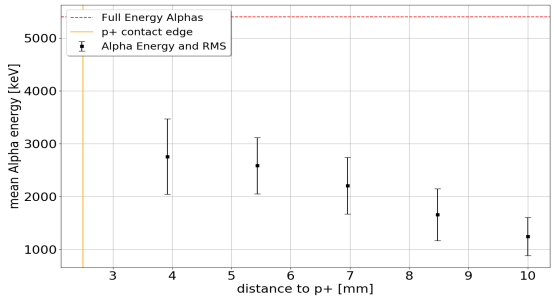

(a) The mean energy of the α PL events in dependence of the incident position. The yellow line indicate the edges of the p+. The red line indicates the mean energy of full energy α events.

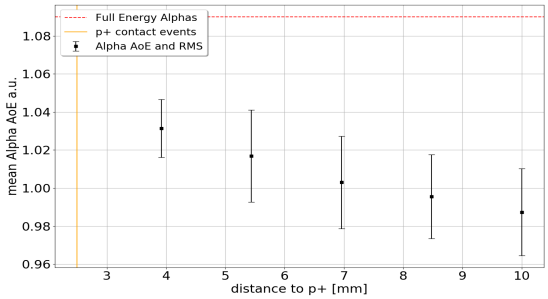

(b) The mean A/E values in dependence of the incident position. The red line indicates the mean A/E of the full energy α events. The A/E drops as soon as the PL is reached and decreases constantly, even below the SSE band.

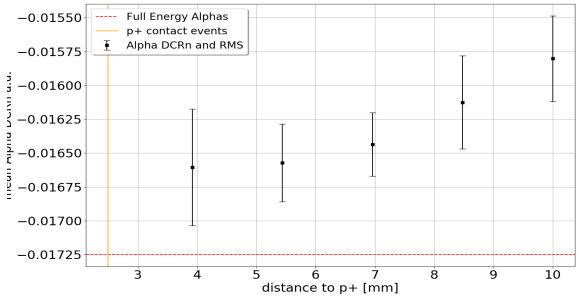

(c) The normalized mean DCRn in dependence of the incident position. The DCRn values rise constantly until the groove is reached.

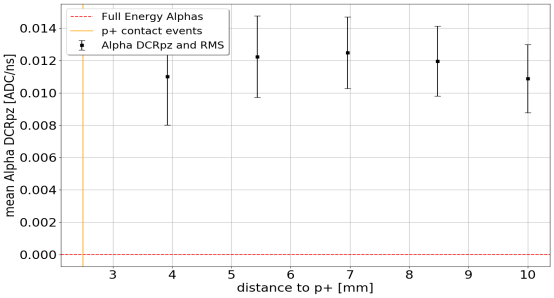

(d) The normalized mean DCRpz in dependence of the incident position. The DCRpz values rise until a maximum value is reached and decreases afterwards.

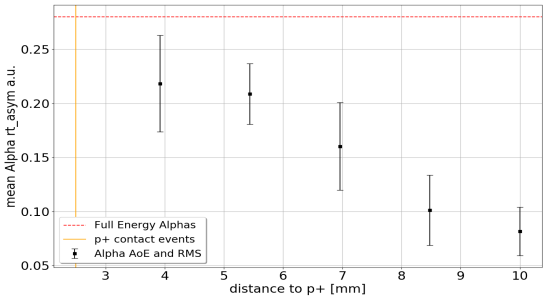

(e) The asymmetry parameter as a function of the distance to the p+

Figure 6.15: The evolution of different pulse shape parameters as a function of the distance to the p+ contact on the right detector side. The orange line indicates the edge of the p+ contact. The red dashed line indicates the mean value of full energy α events.

The groove events:

The groove region has a special geometry, which can influence the field configuration inside the detector. The electric and the weighting field may be distorted at the corners and also may be different at the walls than at its bottom. The incident area, i.e. the spot size of the α cone on the detector surface is bigger than total groove width of 3 mm and a discrimination between wall and bottom events cannot be made. Therefore, an analysis of the groove events becomes complicated. Figure 6.16 shows the A/E distribution of the groove run. A chaotic distribution can be seen at the low energy values. Here the A/E of the α events is widely spread below and above the SSE-band. A clear correspondence to the walls or the bottom of the groove cannot be made. Therefore, a much narrower collimation would be needed in order to distinguish between them.

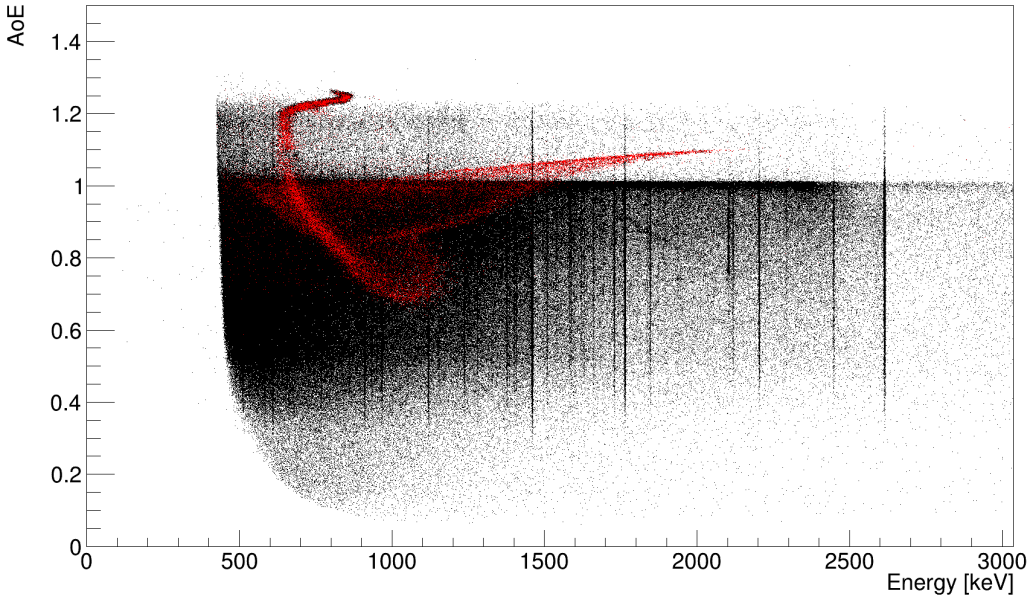

Figure 6.16: The A/E distribution of the groove run. The A/E is widely spread above and below the SSE-band. This behaviour might be attributed to the field configuration close to the groove.

Summary of the radial dependence:

Figure 6.14 contains the overall radial dependence of the different pulse shape parameters of the α events of the left detector side and figure 6.15 the summary of the right detector side. Again, the position information of the right side suffers from a uncertainty, but general statements in radial dependence can still be derived.
The groove events will not be discussed since their pulse shapes can be distorted by complex field configurations due to the groove geometry.

- **Energy:** The energy degrades in radial dependence. The farther the incident position the lesser the measured charge. The energy even decreases down to the threshold of the setup, leading to an energy loss of more than 80 %.
  The first measured α events on the right side are already highly degraded. This is due to the shadowing effect that prevents the αs to interact with the PL close to the p+ contact. The measured α distribution is a broad, highly non-Gaussian peak, correlating to the spot size of the incoming α beam.

- **A/E:** On the left side the A/E decreases compared to p+ runs but remains above the SSE band and slightly rises again.
  On the right side however, the A/E constantly decreases and even falls within the SSE band. This could be potentially dangerous since the main α rejection is based on the A/E parameter.
  The difference between the two sides could originate from the different incident angles in relation to the p+ contact. This could be studied more detailed with future scanning setups that are capable of an angular variation.

- **DCRn:** The DCRn constantly increases with increasing distance. This means that also the decay time of the charge pulse increases.
  There are delayed charges contributing over a much longer timescale (bigger then the waveform length) which slow down the decay of the pulse. However, this DCR effect includes only a few percent within the ca. 80 μs long decay. This delayed energy is directly proportional to the DCRn parameter.
  This also means that the not measured energy is either truly lost (i.e. recombination) or the charges will be collected much later in the order of some ms.

- **DCRpz:** The DCRpz increases with increasing distance until a maximum value is reached. After that the DCRpz decreases towards lower values. However, as it can be seen for the DCRn, this decrease does not mean that the decay time decreases.
  Similar to the DCRn there are delayed charges contributing over a much longer timescale slowing down the decay of the pulse.

- **Asymmetry Parameter:** The asymmetry increases for close p+ positions until it decreases towards the groove. The current pulse becomes more and more symmetric.

Even with an uncertainty on the position of the right side scan a consistent picture of the detector response to α events on the PL can be taken. There are some hints, especially for the A/E, of an angular dependence of the pulse shapes of the α events. The detector response to groove events is more chaotic. This might be due to the different electric fields configurations at the walls, at the bottom and in the corners of the groove.

Comparison to PONAMA I data:

When the ICPC data is compared to the data taken with the PONAMA I PPC detector, it becomes clear that the radial dependence of the energy degradation is contrary between the two data sets. The energy degrades with increasing distance for the ICPC data and increases with increasing distance for the PPC data. This difference might correspond to the sign of possible surface charges, populating the PL. Such a surface charge model will be discussed below. The DCRpz also shows a different behaviour. For the ICPC scan, the DCRpz firstly increases until a maximum value is reached and the DCRpz starts to drop again. The DCRpz increases with increasing distance in the PPC data (see [AAIB+20]). However, the behaviour of the DCRpz is not automatically proportional to the magnitude of the delayed charge recovery effect. Therefore, either the energy of the events also need to be accounted, or a full exponential fit must be performed on the tail of the waveform, which corresponds to the fraction of delayed charge recovery to the prompt energy (i.e the amplitude of the charge pulse). For the ICPC data, the delayed charge fraction increases with increasing distance to p+, and therefore with decreasing energy. For a better comparability of the radial dependency of the strength of the DCR effect, a delayed charge fraction parameter of the PONAMA I data would be needed.

6.4 Evaluation of a DCR cut

The decrease in energy in combination with the A/E degeneration might pose a threat to a $0\nu\beta\beta$ analysis. From the previous observations it becomes clear, that a cut based on the A/E parameter alone may not be sufficient to distinguish the α events from other event classes, and different parameters are needed for an event identification. These parameters will be the DCRn, the $\mathrm{rt}_{\mathrm{asy}}$ and the risetime.
In this work, the signals created by the α particles from the collimated source are the signals of interest. All other contributions will be seen as background. The goal of a cut procedure therefore is to only select these α events and to discard all other events. In this case a spectrum after the cut would contain only α surface events.
For this purpose, a cut based on three different pulse shape parameters will be introduced. A cut based on a single parameter will always contain background events and the fraction of false positive α events increases. The cut strategy therefore is to combine three different parameters in which the αs show a unique and distinct distribution. These three different cut components are:

- the Risetime - This is a cut on the detector Volume,
- the current asymmetry $\mathrm{rt}_{\mathrm{asy}}$- this is a cut on the event type and the detector volume,
- the DCR - this is a cut on the event type and the detector volume.

The first parameter, that will be discussed is the risetime of the waveform. The rise time is calculated following the procedure explained in section 5.3 and covers the time the signal needs from 0.05% of the maximum to 98% of the maximum amplitude. The rise time is highly dependent on the incident position and is proportional to the length of the drift path of the charge carriers and therefore all α events are expected to show a very short rise time. The rise time of the α distribution stays below 450 ns over the entire scan. Of course the short rise time region of the detector can easily be penetrated by other background events. This means that a cut based on the rise time alone is a volume cut on the detector and includes all events in a given region around the p+ contact. The size of this region is given by the cut threshold that is applied. A higher acceptance threshold result in a bigger region. This means that the rise time cut reduces the number of events and cuts non-α events, but the remaining events will still contain other background contributions. Since the absolute value of the rise time is

also dependent on the readout electronics, the acceptance threshold is derived directly from the data. It can be found that a conservative upper limit of 500 ns contains all visible α events.

After the rise time cut, the remaining events will be evaluated by their asymmetry parameter $\mathrm{rt}_{\mathrm{asy}}$. This parameter is a measure of the symmetry of the current pulse and it measures the time difference between the 2% points on the rising and falling side of the current to the current maximum value and gives the ratio between these times. The resulting values of $\mathrm{rt}_{\mathrm{asy}}$ can range from negative values to positive values. Current pulses with a $\mathrm{rt}_{\mathrm{asy}}$ of zero are perfectly symmetric, whereas negative values express a wider left (rising) side of the current pulse and positive values express a wider right (falling) side. The absolute value expresses how strong the asymmetry is.

This parameter is dependent on both, the event type and the detector volume. For SSE bulk events the signal is generated by the movement of one charge carrier package (electrons and holes) within the weighting potential of detector. For most of the detector volume this SSE will produce a distinct asymmetry value $\mathrm{rt}_{\mathrm{asy,SSE}}$ since the electrons and holes will travel through similar weighting potential areas and the current pulse will have a similar shape. This changes for SSE that originate close to the p+ contact. Here the current shape is also position dependent, i.e. dependent on the weighting potential of the initial charge cloud. Close to the p+ contact a high initial weighting potential is present and the current will rise quickly, resulting in a fast rise of the current and therefore a more positive asymmetry parameter.α events can be seen as such SSE close to the p+ contact and therefore a positive asymmetry parameter is expected (see [Ago13]).

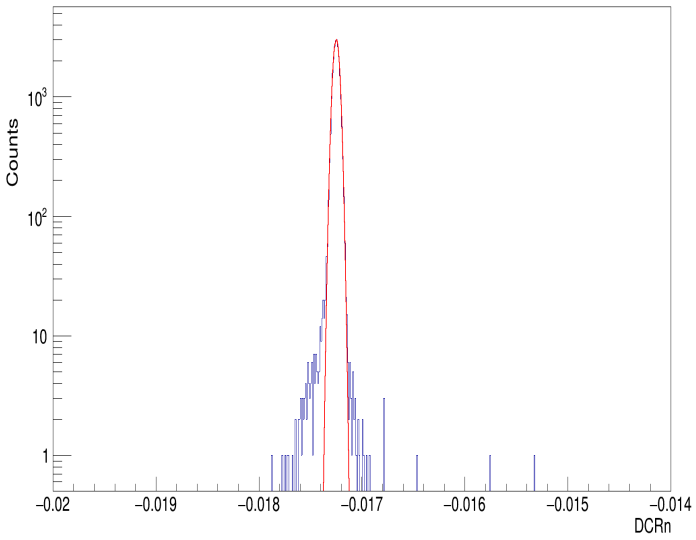

Figure 6.17: The DCRn distribution of the ^{214}Bi line at 1765 keV and the Gaussian fit in red. This procedure will be repeated on several background lines.

MSE are however a bit more troublesome, since the different charge cloud packages can originate at various positions. The maximum current can occur before, after and somewhere in between all other charge carrier packages. Their contribution to the signal can have a wide spread in time and therefore rt_{asy} for MSE has a wide spread. This also makes clear that the rt_{asy} is not a good parameter to distinguish between MSE and SSE. For this purpose the A/E is clearly a better parameter. In combination with the risetime however rt_{asy} provides additional information of the pulse shape and the α cut becomes more precise. The event region that is affected by the cut can be seen in figure 6.18. Here, in figure 6.18a an example of a risetime over rt_{asy} distribution of one run is shown. The cut affects the region which is bottom right of the red dashed line. Figure 6.18b shows a zoom into this region for the runs on the left detector side. It can be seen, that for all runs the α distribution stays inside this cut region. However, as it can also be seen, a cut based only on these two parameters will still include background events.

All α events show a short risetime and a positive rt_{asy}, but not all events with a short risetime and a positive rt_{asy} will be α events. Therefore the DCR parameter will serve as the final piece of the cut procedure.

The risetime and the r_{Asy} cut selects single site events close to the p+ contact. Now the enhanced DCRn values can be used as the final cut parameter. The DCRn distribution is in first order a Gaussian distribution around a mean value μ, with a standard deviation σ. This distribution can be plotted for different energy regions and the energy dependence of μ and σ can be calculated. The mean μ is almost constant over the energy, but σ however shows a stronger energy dependence at low energies. Here the electronic noise influences strongly the DCRn calculation and deviation becomes bigger. Now the DCRn distribution of different lines at different energies can be selected, and a Gaussian fit can be applied. An example fit of the ^{214}Bi line is shown in figure 6.17. It can be seen that the distribution is not purely Gaussian and shows a tail especially to lower DCRn values. For the development of the cut procedure this tail is however not important and only the mean and the approximated Gaussian standard deviation is of interest. The fitted μ and σ can then be plotted against the energy. The μ distribution is then fitted with a linear function and the σ distribution is fitted with $f(E) = \sqrt{a + \frac{b}{E^2}}$. This function is found experimentally and describes nicely the distribution, as it can bee seen in figure 6.19.

Again, a cut based on the DCRn alone is not sufficient since there are also events that show an

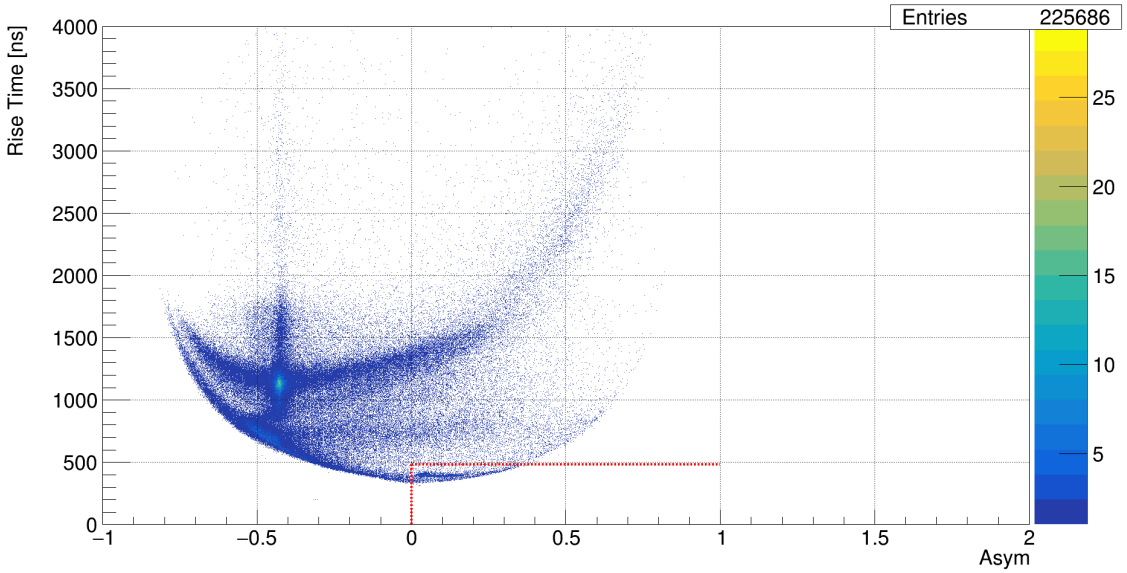

(a) The risetime against $\mathrm{rt}_{\mathrm{asy}}$. The red dashed line indicates the considered parameter space for the DCR cut.

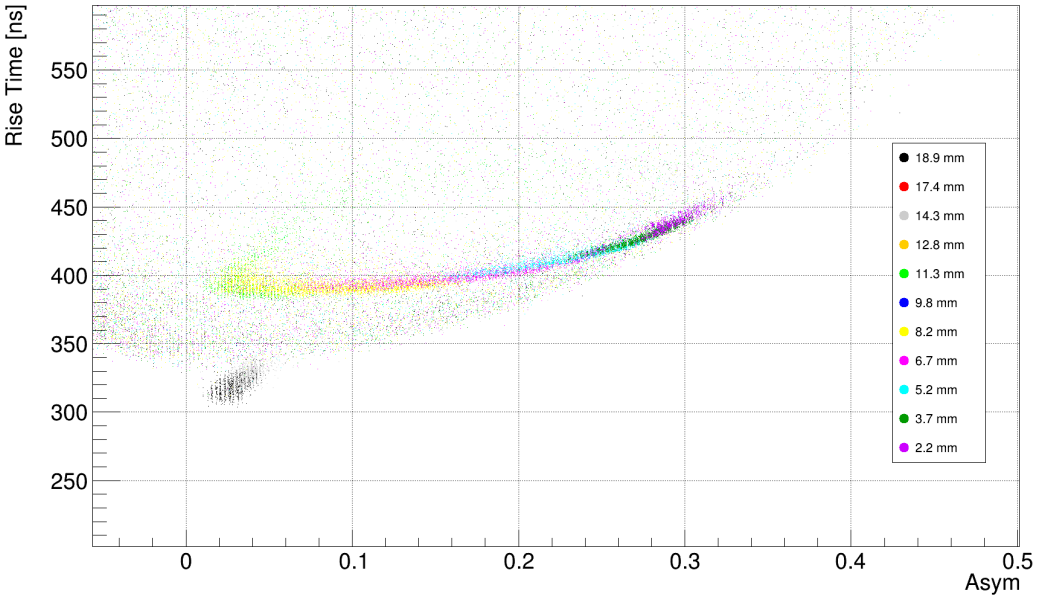

(b) A zoom into the cut region. It can bee seen that all α events stay in the cut region.

Figure 6.18: The risetime against $\mathrm{rt}_{\mathrm{asy}}$ and the region selected by the cut.

increased decay time that are not associated with α events. Not all events with a high DCRn are α events but all α eventss on the PL have a high DCRn. As it has been described in the previous section and as it can be seen in figure 6.20a, the DCRn values of all α events on the PL are enhanced compared to the bulk event distribution.

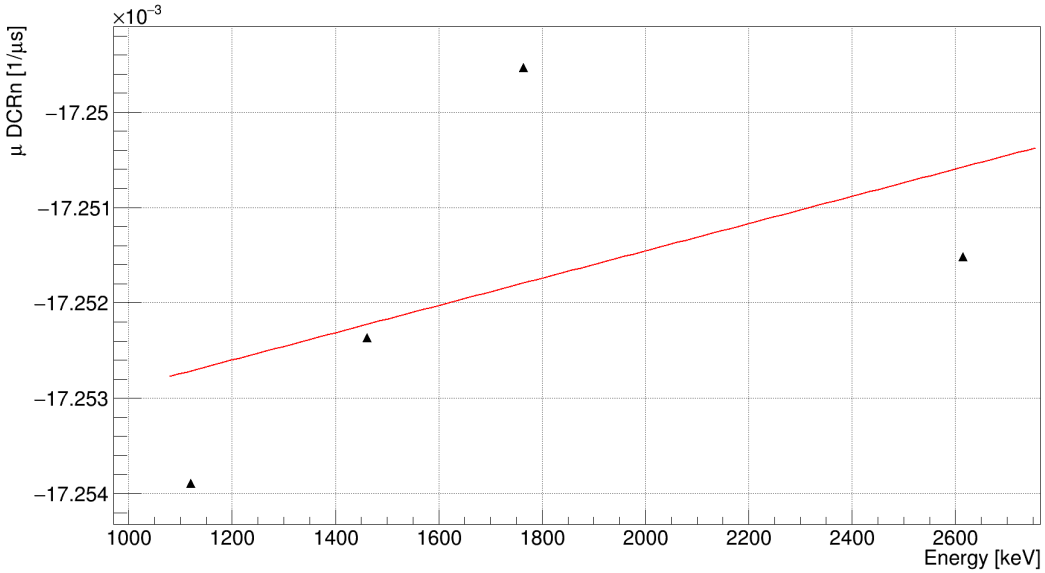

(a) The fitted Gaussian mean μ of four selected lines of a background spectrum.

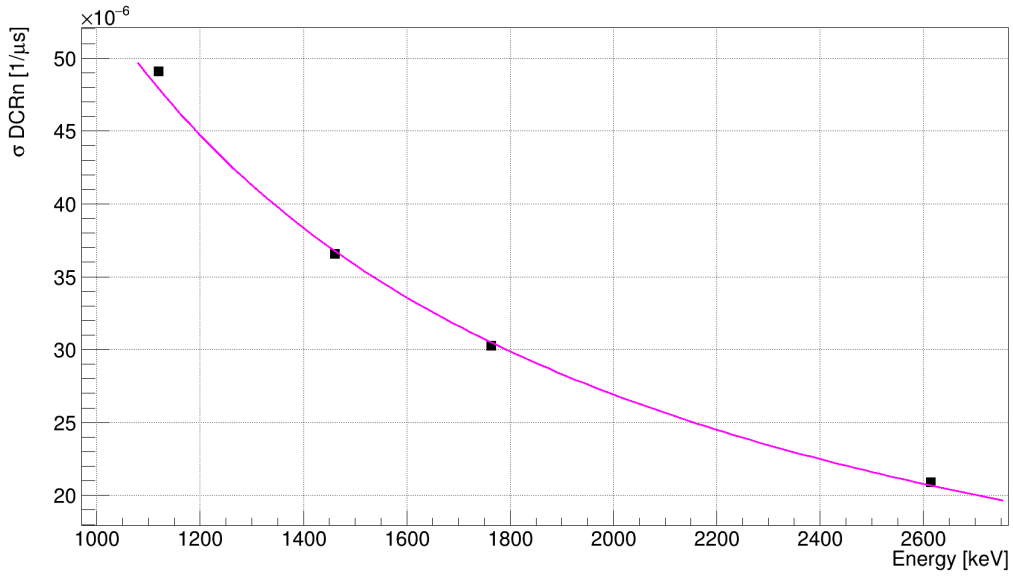

(b) The fitted Gaussian deviation σ of four selected lines of a background spectrum.

Figure 6.19: The fit parameter of the Gaussian fit on four selected background lines.

The cut value is now calculated from the fit functions of the DCRn μ and σ distributions. Therefore the DCRn value of an event is subtracted by the Gaussian mean at the energy of the event and divided by its Gaussian deviation.

$$\mathrm{C_{DCRn}} = \frac{\mathrm{DCRn} - \mu(\mathrm{E})}{\sigma(\mathrm{E})}$$

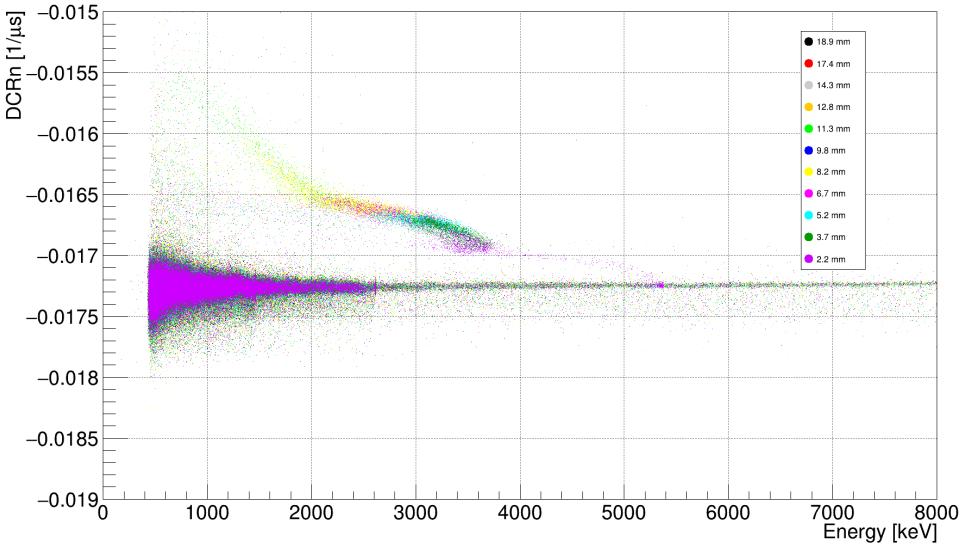

(a) A combined plot of the DCRn distributions of all left side runs. The DCRn values of the α events are enhanced compared to normal bulk events.

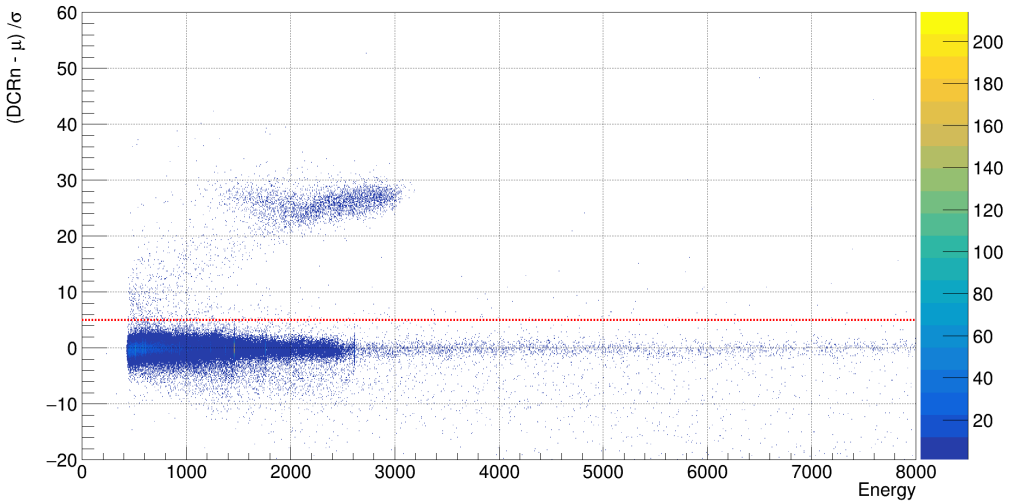

(b) The deviation of the DCRn to the mean value in terms of the standard deviation σ. The Cut value is set to 5 σ (red dashed line) this means an event with a DCRn value exceeding 5 times the standard deviation will be considered for a cut and will be cut if the asymmetry parameter and the risetime also exceed the cut threshold

Figure 6.20: The DCRn parameter distribution (a) and the cut value (b)

The cut value states how many σ's the DCRn value deviates from μ. This cut value distribution is shown in figure 6.20b. The cut line is arbitrary set to 5σ, which cuts all α PL events but also a fraction of background events. Only the tailored combination of risetime, $\mathrm{rt}_{\mathrm{asy}}$ and DCRn is

able to almost exclusively select events originating in the PL.

If the cut is applied on background runs only (i.e. runs on which no α contribution is expected) a tiny event fraction will be selected. Table 6 gives an overview of the survival fraction of background events in three runs without an α source present on the PL.

	DCRn		**DCRpz**	
# of events	# of surv. events	surv. fraction %	# of surv. events	surv. fraction %
2252809	186	$8.3 \cdot 10^{-3}$	716	$31.8 \cdot 10^{-3}$
373388	23	$6.2 \cdot 10^{-3}$	112	$30.0 \cdot 10^{-3}$
127796	5	$3.9 \cdot 10^{-3}$	32	$25.0 \cdot 10^{-3}$

Table 6: Cut efficiencies on three different background runs.

The survival fraction for all background runs is way below 0.1‰, i.e. the false positive rate of the cut is tiny. Even more interesting however is the cut efficiency. The cut efficiency ϵ_c is the fraction of events that have been correctly selected out of a signal sample. Here the cut efficiency means the identification capability of α events on the passivated surface. A 100% efficiency (or a ϵ_c of 1) means that all α events have been identified correctly, whereas an efficiency below 1 means that some α events where not identified and are counted as background. Also an efficiency above 1 is possible if background events are falsely identified as α events. For the determination of the cut efficiency a good estimate on the induced signal strength S is important. It will be shown, that this estimation will be very difficult for the TUBE setup and the computation of the cut efficiency is somewhat cumbersome. In order to point out these difficulties, a general approach on determining a cut efficiency will be introduced in the following and the difference to the TUBE data will be explained.

In general, a determination of a cut efficiency ϵ_c needs a test sample that contains a signal over a background on which the cut can be applied. Ideally such a test sample would be consistent of a Gaussian shaped signal S over a flat Background distribution B. For a correct efficiency calculation either the signal strength S or the Background B needs to be very well known. There are several ways in which a high knowledge of either S or B can be achieved. S can for example be known beforehand, i.e. the introduced Signal could be a test pulser with known properties and a known rate. The Signal strength could also be estimated from simulation. In this case of course the validity of the simulation must be very high.

Finally the signal strength S can also be estimated from test sample itself as an "On-Off"

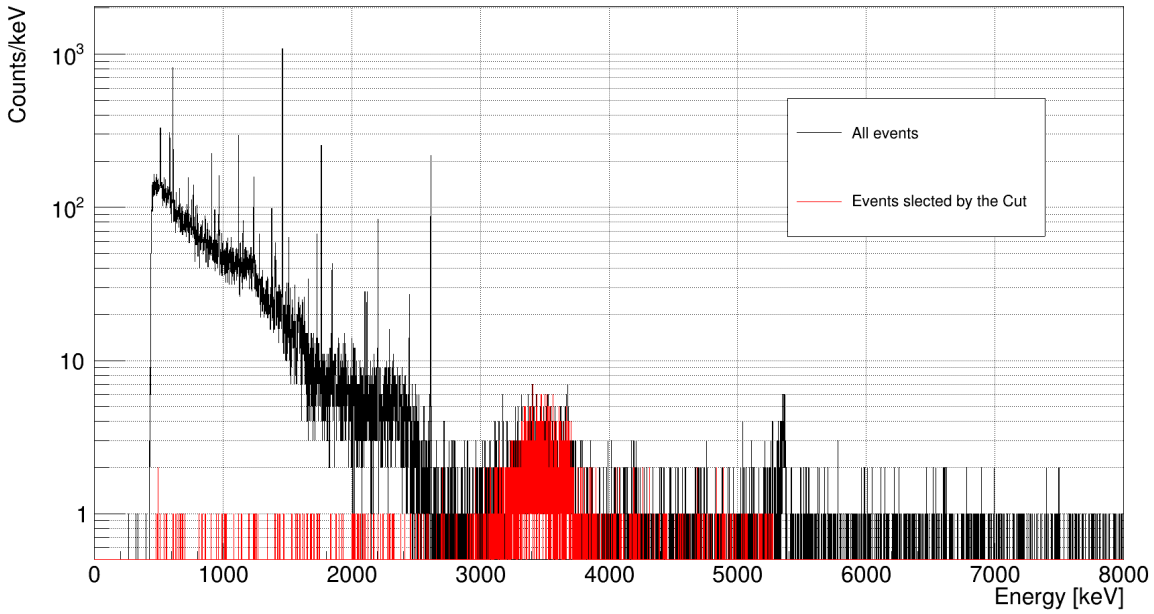

Figure 6.21: Energy Spectrum before (black) and after the cut procedure (red). The degraded α events can be seen as the excess at around 3.5 MeV. The full energy α can also be seen in black at 5.4 MeV. These events are not selected by the cut since their DCR is not increased compared to bulk events.

approach. In this case S is estimated by the comparison of a signal band ("On") to a background sideband ("Off") of the same range. In the case of a simple flat background the signal strength S is simply given by total number of events in the signal band $n_{t,s}$ minus the under laying background n_b, whereas n_b is just given by the total number of events in the sideband $S = n_{t,s} - n_b$.

With a known strength S the cut efficiency is then given by the number of events that are selected by the cut divided by the signal strength S $\epsilon_c = {}^{n_c}/_{S}$ and its uncertainty is given by Poisson statistics alone.

For the TUBE measurement campaign, this calculation cannot be directly applied, because the estimate of S appears to be very difficult. The signal strength is not known beforehand and a proper estimation from simulation suffers from various uncertainties, like the uncertainty of the source activity and the uncertainty of the source geometry which results in a high uncertainty of the expected count rate on the detector surface.

The estimation by the On-Off approach suffers especially from the very broad α energy dis-

tribution and the high background level of the TUBE setup. Below the 2614.5 keV line the measured α population is covered by several lines such that an assumption of a Gaussian peak over a flat background cannot be made. Only above the highest gamma line there is a chance to perform a signal and background estimation on the linear muoinc background. Such a signal over a linear background is shown in figure 6.21 for run 18. Here the α events can be seen as a broad peak over a range of around 1500 keV. This wide range is far from optimal, since the On-Off approach works best with sharp signals. The background estimation is carried out on a 1500 keV window from 5500 keV to 7000 keV above the kinetic energy of the emitted α particles, ensuring that no α events contribute to the reference range. However, the muonic background appears linear over energy but not constant. This means the estimated background strength from reference range cannot be simply subtracted from the signal but has to be scaled. The scaling factor to project the measured background at the reference region to the signal region is taken from a dedicated background run without any α contribution. The ratio between the number of counts in the signal range to the reference range gives the scaling factor for the background projection. The overall cut efficiency is then given by

$$\epsilon_c = \frac{\mathrm{S_c}}{\mathrm{n_t} - \mathrm{n_b}} = \frac{\mathrm{S_c}}{\mathrm{n_t} - \mathrm{n_{c,r}} \cdot \frac{\mathrm{n_{b,s}}}{\mathrm{n_{b,r}}}}$$

with $\mathrm{S_c}$ as the number of events selected as signal by the cut, $\mathrm{n_t}$ as the total number (S+B) in the signal region of the α run, $\mathrm{n_b}$ as the number of background events in the signal region which are estimated by the number events in the reference window of the α run $\mathrm{n_{c,r}}$ scaled with the factor taken from the background run $\frac{\mathrm{n_{b,s}}}{\mathrm{n_{b,r}}}$.

It becomes clear that also this On-Off approach suffers from (mainly statistical) uncertainties and assumes a stable muon induced background rate between the signal and background runs. In this case the uncertainties can be derived from Poisson statistics and can be expressed by common error propagation.

$$\Delta\epsilon_c = \sqrt{\left(\frac{\delta\epsilon_c}{\delta \mathrm{n_t}} \cdot \Delta \mathrm{n_t}\right)^2 + \left(\frac{\delta\epsilon_c}{\delta \mathrm{n_{c,r}}} \cdot \Delta \mathrm{n_{c,r}}\right)^2 + \left(\frac{\delta\epsilon_c}{\delta \mathrm{n_{b,s}}} \cdot \Delta \mathrm{n_{b,s}}\right)^2 + \left(\frac{\delta\epsilon_c}{\delta \mathrm{n_{b,r}}} \cdot \Delta \mathrm{n_{b,r}}\right)^2}$$

where the relative uncertainty of the count numbers is given by $\Delta \mathrm{n_i} = \sqrt{\mathrm{n_i}}$.

In general, the cuts are performing very well and no significant difference between the DCRn - and DCRPz based cutting procedures can be observed. Both parameters work similar in this

	DCRn			**DCRpz**		
distance [mm]	cut eff. ϵ_c	$\Delta\epsilon_c$	90% lower limit	cut eff. ϵ_c	$\Delta\epsilon_c$	90% lower limit
9.8	0.990	0.051	0.906	0.992	0.051	0.908
8.2	0.978	0.046	0.90	0.979	0.046	0.903
6.7	0.936	0.059	0.839	0.94	0.059	0.843

Table 7: Cut efficiencies on three different signal runs.

energy range. Also, from these three α runs at different positions, an energy dependence can be interpreted. Especially the run closest to the p+ shows a decreased efficiency, since not all α particles interact on the PL. Here the fraction of p+ α events is bigger compared to the other runs. As seen in 6.14 the DCR and its deviation from the mean bulk value increases for a bigger energy degradation. This means at positions close to the p+ with lower degradation a worse separation and therefore a worse cut efficiency is expected.
Unfortunately, it is impossible to study the cut efficiencies in detail at the DEP and at $Q_{\beta\beta}$. However, the separation of the DCR-values from the mean bulk events increases down to 1 MeV before it starts losing separation power. This loss below 1 MeV can be attributed to the higher influence the electronic noise has on the pulse shape. The higher the noise fraction, the less the performance for PSD parameters. This means that, from this data, confidence in the discrimination capability of α events in the PL can be gained. A deeper analysis of the efficiency would most likely need another, dedicated scanning campaign with much lower background in the region below 2.6 MeV and a narrower geometrical α distribution on the detector surface. This way the α peak would also become more narrow and the signal discrimination would become easier. This could be achieved with a smaller collimation and, in case the same or even a higher count rate should be achieved, a source with increased activity would be needed. Also an investigation of the incident angular dependence is needed for this detector type.

6.5 Delayed Charge Recovery Models

I the previous section, it could be shown that the delayed α events can be removed with great accuracy. But the origin of the DCR-effect is still not fully understood. In order to study this effect, the charge and current pulses will be analysed in more detailed in the following. In the figure 6.22 the charge and current pulses of different α events are shown, starting from a full

energy α and ending with a groove event. The charge pulses are normalized to the full energy α event and the current pulses are simple derivatives of the normalized charge.

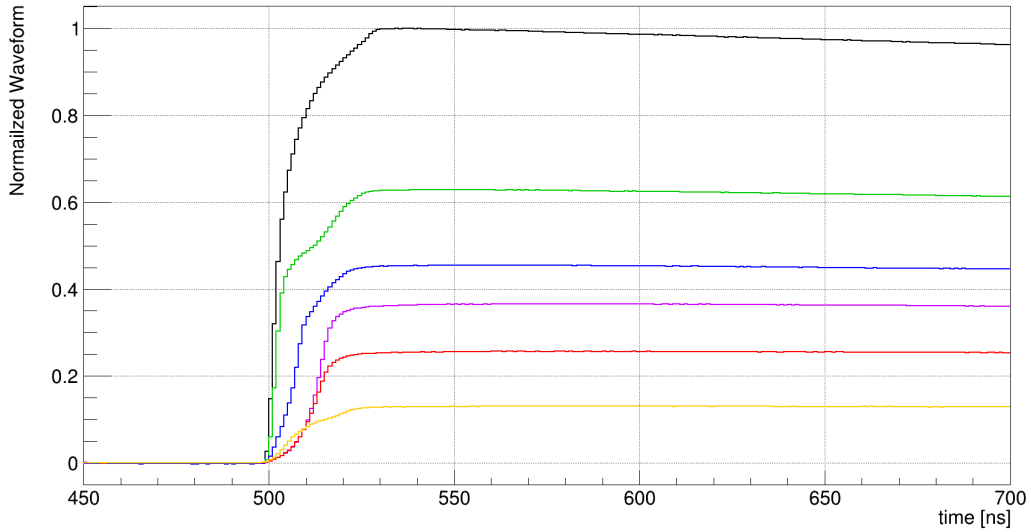

(a) Charge pulses of different α Events, normalized to the (black) full energy α. The other pulses consecutively degrade in energy. The red pulse is the last pulse associated with the PL. The yellow pulse is assumed to to be a groove event. A time offset has been applied in order to make a better visual representation.

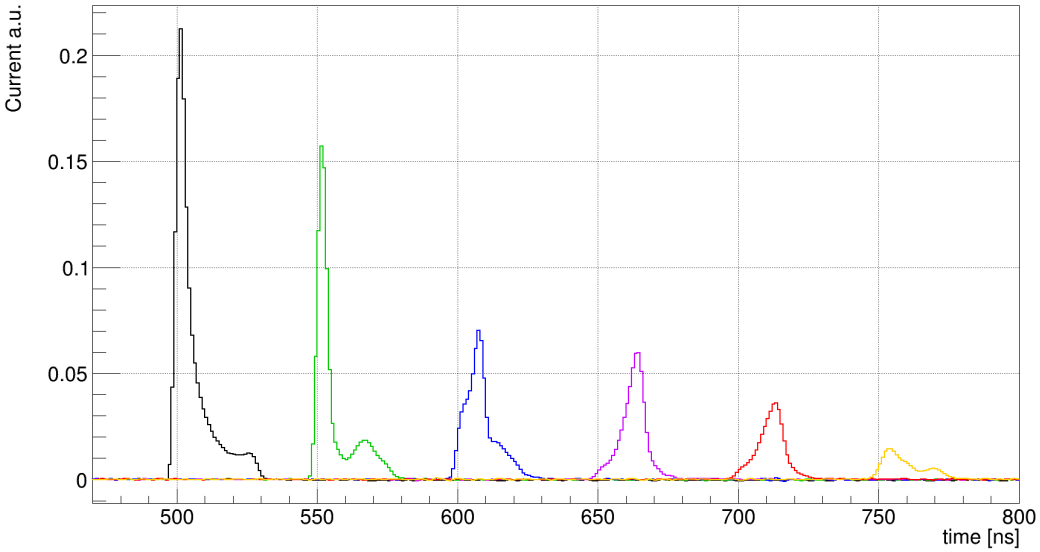

(b) Currents of different α events. The colors correspond to the same charge pulses on the top panel. A time offset has been applied in order to make a better visual representation.

Figure 6.22: Comparison of charge pulses and currents for different α events.

The full energy α event pulse shapes meet the expectations based on the normal signal formation. These events originate in high weighting potential areas which leads to fast rise of the charge and the current. Because of the relative long drift path of the electrons the current decays rather slowly which is also responsible for the round side of the charge at the end of the rising edge.
The α events on the PL do not meet any expectations due to a normal signal formation. In figure 6.22 in green an event close to the p+ is shown which seems to be composed out out two parts. A normal fast rising charge and current pulse and another slower and weaker part. When the point of origin moves away from the p+ the slower part seems to overlap more and more with the normal rising edge. It is expected for the normal part that the pulse shapes changes with increasing distance. Lower weighting potential areas are being crossed by the hole for a longer time which makes the rising edge of the charge smoother and the current amplitude lower. Also the asymmetry of the current and therefore the asymmetry parameter is expected to change toward lower values. The second part interferes and distorts the pulse shapes. The increasing decay time of the charge pulses can be anticipated. This is not visible in the current pulses since the decay time is much longer then the timescale of the derivative.

Previous to this work, several models of α PL events on a PPC detector have been developed and tested. These models can be applied and the result will be discussed in the following. Two important observations could be made previously. It could be shown that the measured energy of the α PL events decrease with increasing radii and the decay time increases with increasing radii. This radial dependency has not been observed prior to this work on the ORTEC PPC PONAMA I campaign with the TUBE setup back in 2016.
Contrary to the ICPC campaign, the observation that has been made with PONAMA I showed a increasing energy with increasing radii, i.e. events originating close to the p+ contact show a smaller energy. The DCRpz however showed a similar behaviour to the ICPC observation, i.e. an increasing DCR value with increasing distance to p+.

In order to reprocess and to understand the PONAMAI observation different models of charge collection have been developed and tested within the MAJORANA collaboration and have been reported here [AAIB+20]. These models have been developed using the mjd_siggen and mjd_fieldgen software packages for electric field and pulse shape simulation in Germanium detectors. It has been found that the energy degradation can be modeled when additional charges are placed on the passivated surface and a delayed surface drift of the charge carriers

will be implemented. These surface charges attract or repel the charge carriers, based on the sign of the charges (i.e. electrons are attracted to positive surface charges and holes are attracted to negative surface charges) and undergo a slower transportation on the passivated surface. This way the complementary directions of energy degradation in radial dependence can be expressed by the sign of the surface charge. The increasing energy with bigger distance to p+, as seen within the PONAMAI campaign, can be assigned to a positive surface charge that reduces the electron contribution to the signal. Vice versa a negative surface charge is expected to reduce the energy as the incident radius increases. This has not been observed prior to this work but is indeed what could be seen within the ICPC campaign.

The modeling of the DCR however appeared to be more complex and the observations could not be reproduced sufficiently. Further studies on the charge recovery are needed to fully understand the mechanics behind this effect.
However, the models of surface charges have also been tested within this work and its results will be presented in the following.

6.5.1 Monte Carlo and Pulse Shape Simulations

For the Monte Carlo simulation the software MaGe has been used and the geometry of the ICPC detector and the TUBE setup, as it has been described in chapter 5.3, has been implemented in detail. A part of this implementation is the collimator, tilted by an angle of 66° that can be moved along the detector axis such that different interaction positions of the simulated ^{241}Am αs can be achieved. The interaction position in (x,y,z) coordinates together with the deposited energy at each step are recorded and stored to an output file. An example of the output coordinates of four different starting position of the collimator position is shown in figure 6.23. It can be seen that interaction positions of the αs follow the detector axis as the source moves further. Also the shadowing effects due to the incoming angle at the edge of the groove and the read out pin is clearly visible.

These Monte Carlo output now serves as input for the pulse shape simulation, which has also been done with the mjd_siggen software. Due to a difference in the coordinate systems of the different software packages the positions from the MaGe output have to be converted in order to represent the same position in mjd_siggen coordinates. The point of origin in MaGe is the detector center whereas in mjd_siggen the point of origin is at the p+ contact. After this

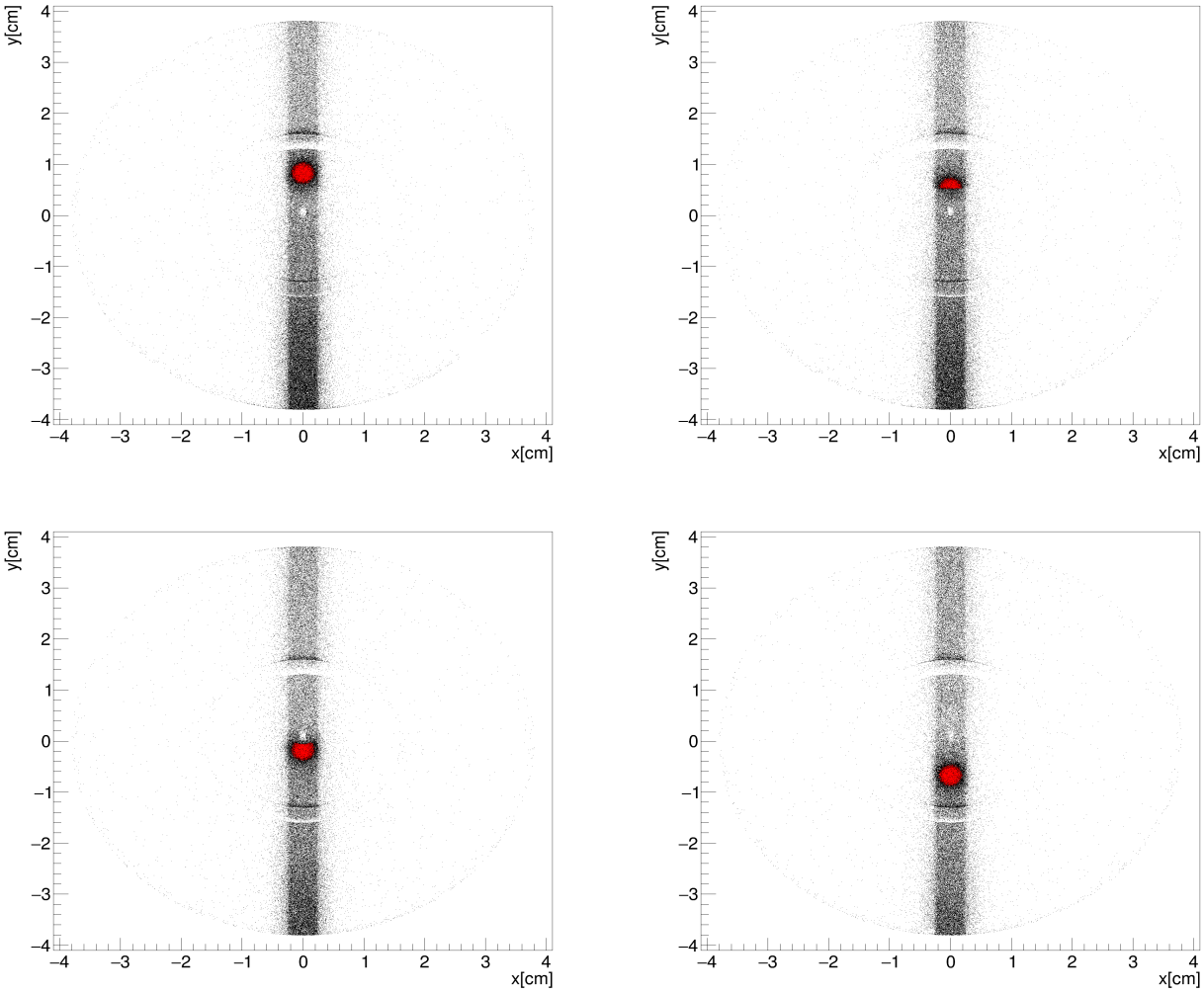

Figure 6.23: The interaction position of the in the x-y plane of four different collimator positions. The red dots indicate α particles whereas the black dots are gamma interactions. The shadowing from the Copper shield can be seen as the band along the y-axis. Also the shadowing effect of the groove and the readout pin can be seen.

conversion the charge pulses of all interactions within the detector will be simulated. Therefore all individual energy depositions of on event are simulated individually and will be summed up afterwards, scaled by their individual energy contribution.

The resulting charge pulses are now additionally convoluted with a simple electronic response function, taken from [Pan18], that simulates the bandwidth limiting frequency pass of the rising edge and the decay of the pulse from the feedback loop. At the end a simple Gaussian noise is added to the pulse.

A comparison of a received raw spectrum from the MaGe output, the raw mjd_siggen output and the final spectrum with an electronic response applied is shown in figure 6.24.

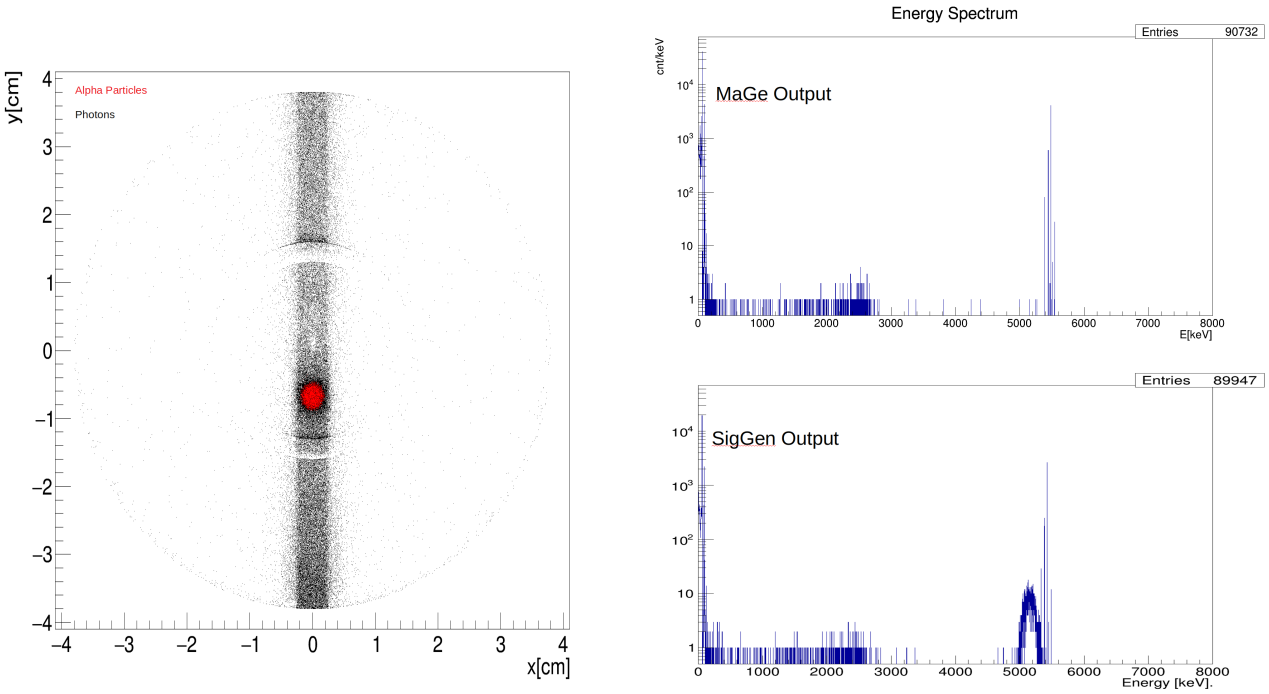

Figure 6.24: A comparison of a simulated Spectrum from a raw Monte Carlo to a full pulse shape simulation with a standard Signal formation. A small Deadlayer effect can be seen on the PL events. This effect is included in the mjd_siggen software and is not part of MaGe. Hence the MaGe output only contains full energy α events.

The calculation of the pulse shape simulations can now be modified, especially by the addition of either positive or negative surface charges on the PL and by allowing for surface drift of the charge carriers. With the modifications the position dependent response of the α signals to the surface charges can be tested. Three different models on various collimator positions have been simulated and compared.

Model 1: No surface charges have been placed.

Model 2: A negative surface charge of $-0.6 \cdot 10^{10} \frac{\mathrm{e}}{\mathrm{cm}^2}$ has been placed on the passivated surface.

Model 3: A positive surface charge of $0.6 \cdot 10^{10} \frac{\mathrm{e}}{\mathrm{cm}^2}$ has been placed on the surface.

The surface drift velocity has been reduced by a factor of 0.0001 for **Model 2** and **3**.

For all models the received pulse shapes and energy distributions can now be compared to each other and to the data. In figure 6.26 and 6.25 the same comparison of the simulated energy

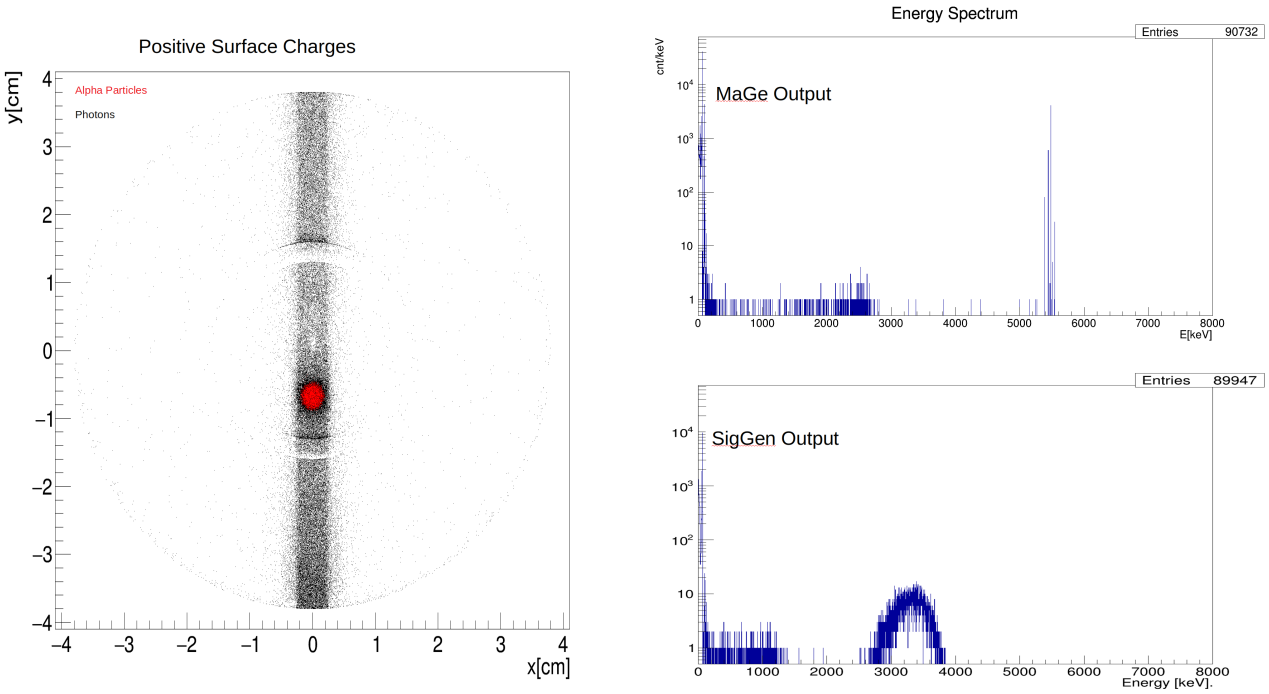

Figure 6.25: The mjd_siggen Model with a positive surface charge on the PL. An energy degradation can be seen.

spectra with the different models applied are shown. It can be seen that both surface charge models lead to a reduction of the measured energy.

Both models show a position dependent energy degradation. However, both models do not match what can be observed in the data. The negative surface charge model creates a very broad smearing of the α energy distribution, beyond of what can be observed in the data. This can be seen in figure 6.27 where the energy in dependence of the distance to the p+ is shown.

The positive surface charge model decreases the energy, but only until a certain level of around 4 MeV. A further increase in distance does not lead to a further decrease in energy. The electrons already contribute so less that a further increase in distance does not cut any significant contribution anymore. This is also shown in figure 6.27.

The mismatch between the models and the data can also be seen when looking at the pulses. Figure 6.28 shows the resulting charge and current pulses for two α events at different positions. The nominal energy is the same and only the incident radius is higher for the red event.
The negative surface model leads to reduction of the charge amplitude. The pulse shape itself stays unchanged. The positive surface charge also leaves the pulse shape unchanged but splits

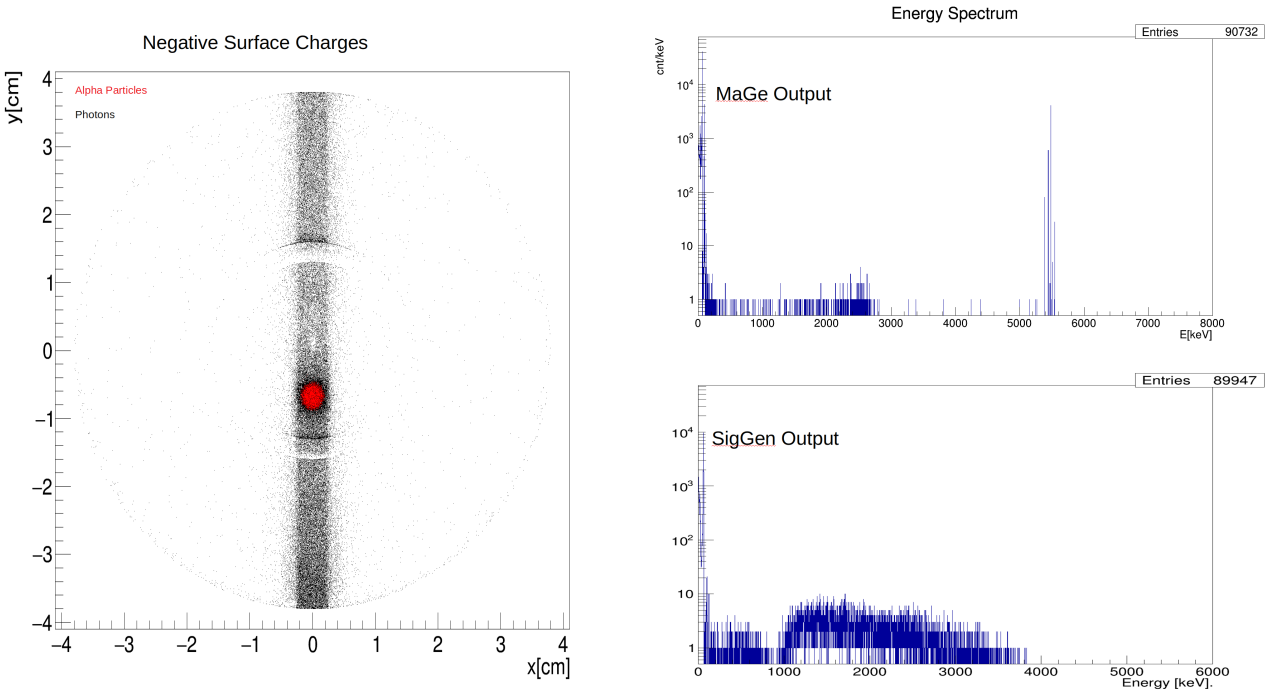

Figure 6.26: The mjd_siggen Model with a negative surface charge on the PL. An even higher energy degradation can be seen.

the pulse basically into to parts. But unlike to the data these two parts have normal pulse shapes, one just delayed and reduced in amplitude.

Overall both models are not able to reproduce the observed energy degradation and the pulse shape. Also the increase of the decay time is not reproduced by these models. It becomes clear that more effects play a role in these PL events and the mechanics in their signal formation are more complicated.
One attempt to get more insight is to have again a closer look on the mechanisms of the signal formation.

6.5.2 Qualitative signal modulation

For the modulation of the degraded signals, a qualitatively approach will be introduced. It will be discussed how the charge carrier transportation in general can be used to change the signal formation.

As a start it becomes useful to study a simple toy model of a signal formation. Therefore the a single charge carrier pair will be placed inside an arbitrary one dimensional weighting potential and the charge and current will be calculated.

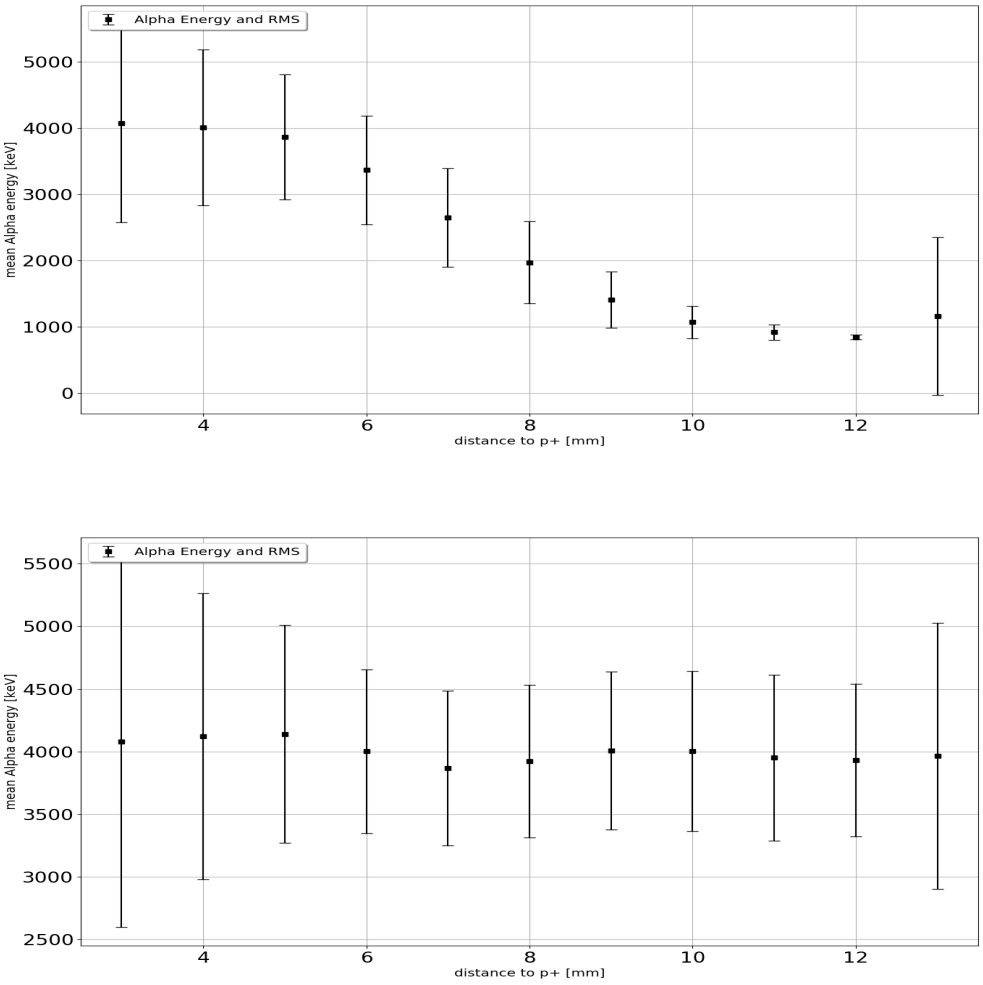

Figure 6.27: Mean simulated α Energy in dependence of the distance to p+ for negative (top) and positive (bottom) surface charges.

Single Charge Carriers inside a Weighting Potential:

The signal formation inside a HPGe detector can be calculated from the movement of the charge carriers through the Weighting Potential of the detector (see section 4.2.3). The induced charge at the electrodes in dependence of the position x inside the weighting potential can be expressed as:

$$\mathrm{Q_{e,h}(x)} = \mathrm{q^{e,h}} \cdot \phi_W(\mathrm{x})$$

with its induced current

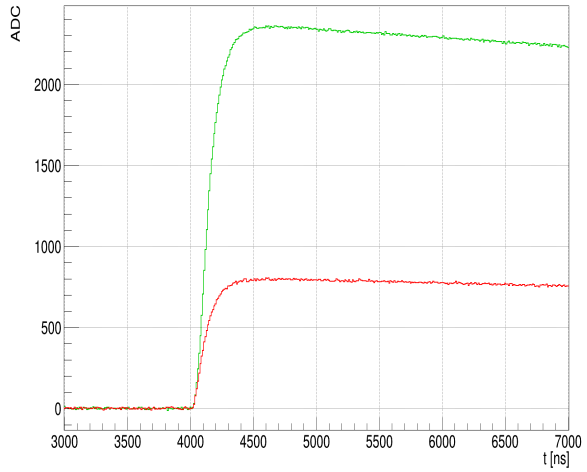

(a) Charge pulses with negative surface charges.

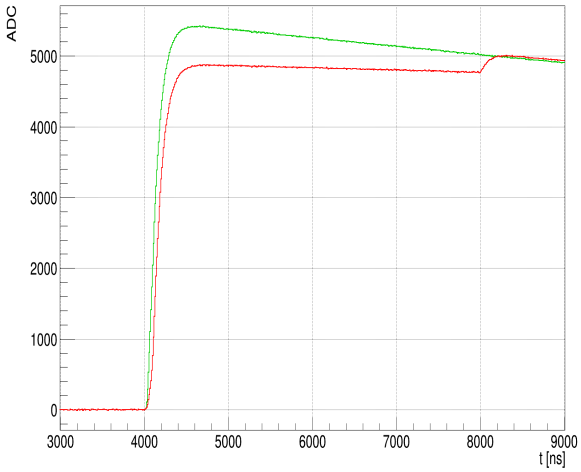

(b) Charge pulses with positive surface charges.

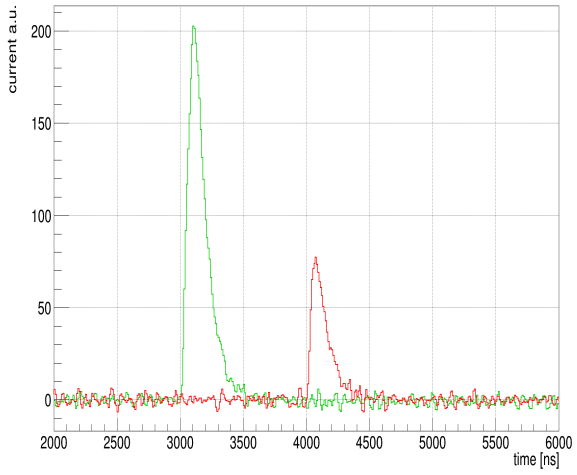

(c) Current pulses with negative surface charges. A time offset is introduced for better visibility.

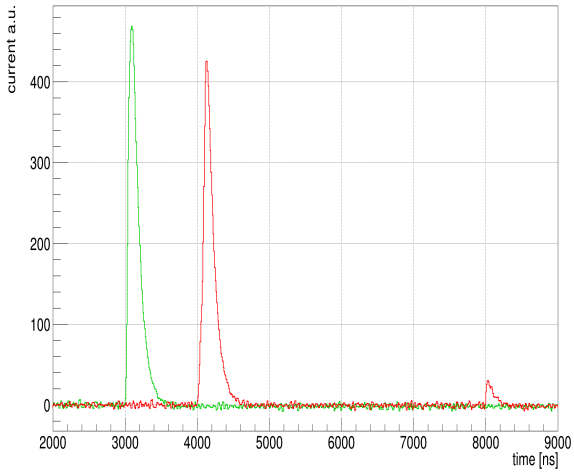

(d) Current pulses with positive surface charges. A time offset is introduced for better visibility.

Figure 6.28: Charge and current pulses with different surface charges applied. In green a close by event is shown and in red an event far away from the p+. Both events have nominal the same energy.

$$I_{e,h}(x) = \frac{dQ_{e,h}(x)}{dt} = q_{e,h} \cdot v_{e,h} \cdot E_W(x).$$

Here $\Phi_W(x)$ and $E_W(x)$ are the weighting potential and its gradient the weighting field.
The drift path of the charge carriers inside the HPGe is determined by the electric field inside the detector. In this example the drift path is only along the x-axis with a constant velocity. The measured signal is then the sum of all charge carrier contributions and the measured

current is sum over all induced currents.

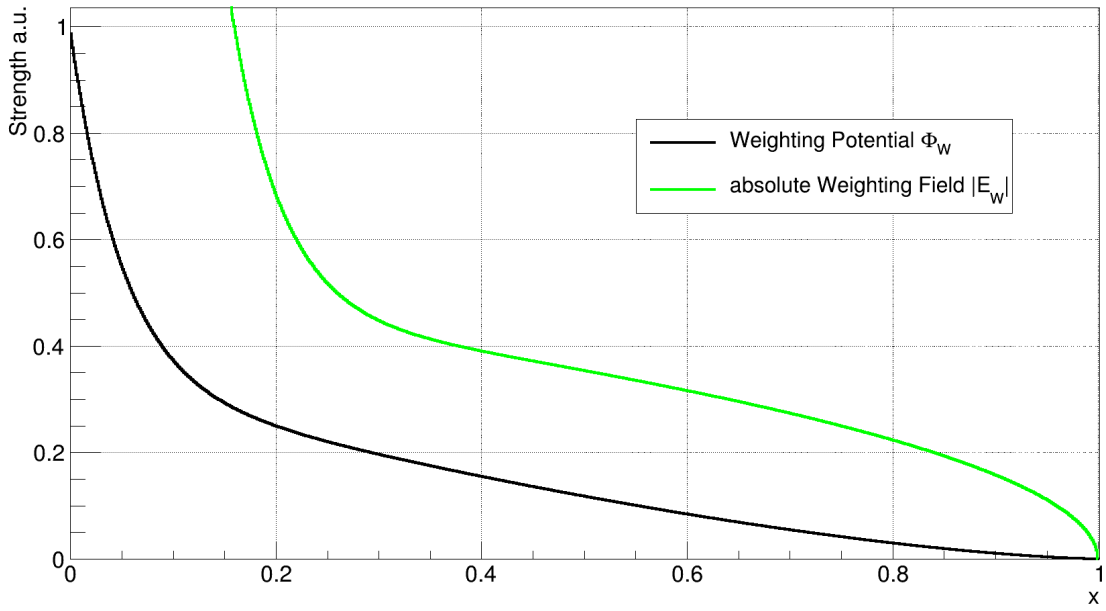

Figure 6.29: The constructed weighting potential in red and the absolute value of its gradient in green.

In the following only single site bulk events will be considered. Single site events can be approximated by one electron-hole cloud migrating through the detector and forming only one signal. No surface effect and also no other charge cloud properties like diffusion or self-repulsion are applied so far. α events, with a mean free math in the order of tens of μm in Germanium, can be seen as such single site events.

Inside a depleted ICPC detector the weighting field (i.e. the gradient of the weighting potential) is usually highest close to the p+ read out contact (see figure 6.29) and the signal creation happens mainly in high weighting field areas. Therefore, the initial creation point of the charge carriers has a big effect on the shape of the measured signal. To demonstrate this behaviour, a simple one dimensional weighting potential can be constructed that simulates qualitatively the signal formation by the movement of an electron hole pair. Such a potential can be given as

$$E_{\phi(x)} = \frac{2}{3} \cdot \left[\left(\frac{1-x}{1+x} \right)^{10} + \frac{1}{2} \cdot \left(1-x \right)^{1.5} \right]$$

This potential has been taken from [Bud09] and is shown in figure 6.29. The choice of the potential is arbitrary with the requirements of a small almost constant gradient that is sharply

increasing close to the read out contact and an arbitrary range of x between 0 and 1, whereas the position of the p+ contact would be set to 0.

Now the charges $q^{e,h} = \pm 1$ can be placed somewhere in the potential (e.g at $x_0 = r = 0.5$) and their migration starts whereas the hole moves towards 0 and the electron moves towards 1. The resulting induced charge of both charge carriers and their sum is shown in figure 6.30 From this diagram it becomes obvious that the shape of the charge pulse, and therefore also the shape of the current pulse, is highly dependent on the incident position. If the interaction happens close to the p+ contact in a high weighting potential, the holes contribute fast and the charge pulse rises quickly until all holes are collected at the p+ electrode. The electrons however are still migrating through the detector and contributing to the signal on a longer timescale, resulting in the visible "kink" of the pulse in the first three panels of figure 6.30. This also means that the current rises fast and decays slowly which leads to a positive asymmetry parameter.

For incident position closer to the n+ contact, the electrons contribute less and less to the signal, as the incident point is in an area of a low weighting potential and the electrons are moving against its gradient. This means for these positions the charge pulse is almost exclusively dominated by the holes and can be approximated by $Q(x) = 1 - \Phi_W(x)$ for the weighting potential along the drift path.

The current rises slower compared to close p+ positions which shifts the asymmetry parameter to smaller values.

Overall, the delayed charge recovery and the energy degradation cannot be reproduced by only a delay of the charge carrier mobility. Additional effects must play a role in this signal formation.

Therefore a qualitative approach to reproduce the energy degradation and the DCR will be introduced in the following. This means that the modifications on the signal are tailored to reproduce the observed pulses and are not an implementation of a given physical effect. This approach is not meant to provide an accurate physical model but rather to show and describe what properties must be applied in order to reproduce the measured signals. This approach will be discussed in the following.

It has been shown that an energy degradation originating from a delayed charge collection leads to a DCR effect that has not been observed. The idea of this effective model is to split the initial signal into several parts which create the different observed modifications and combine them again afterwards. This means that the input charges q_e, h will be split into three parts.

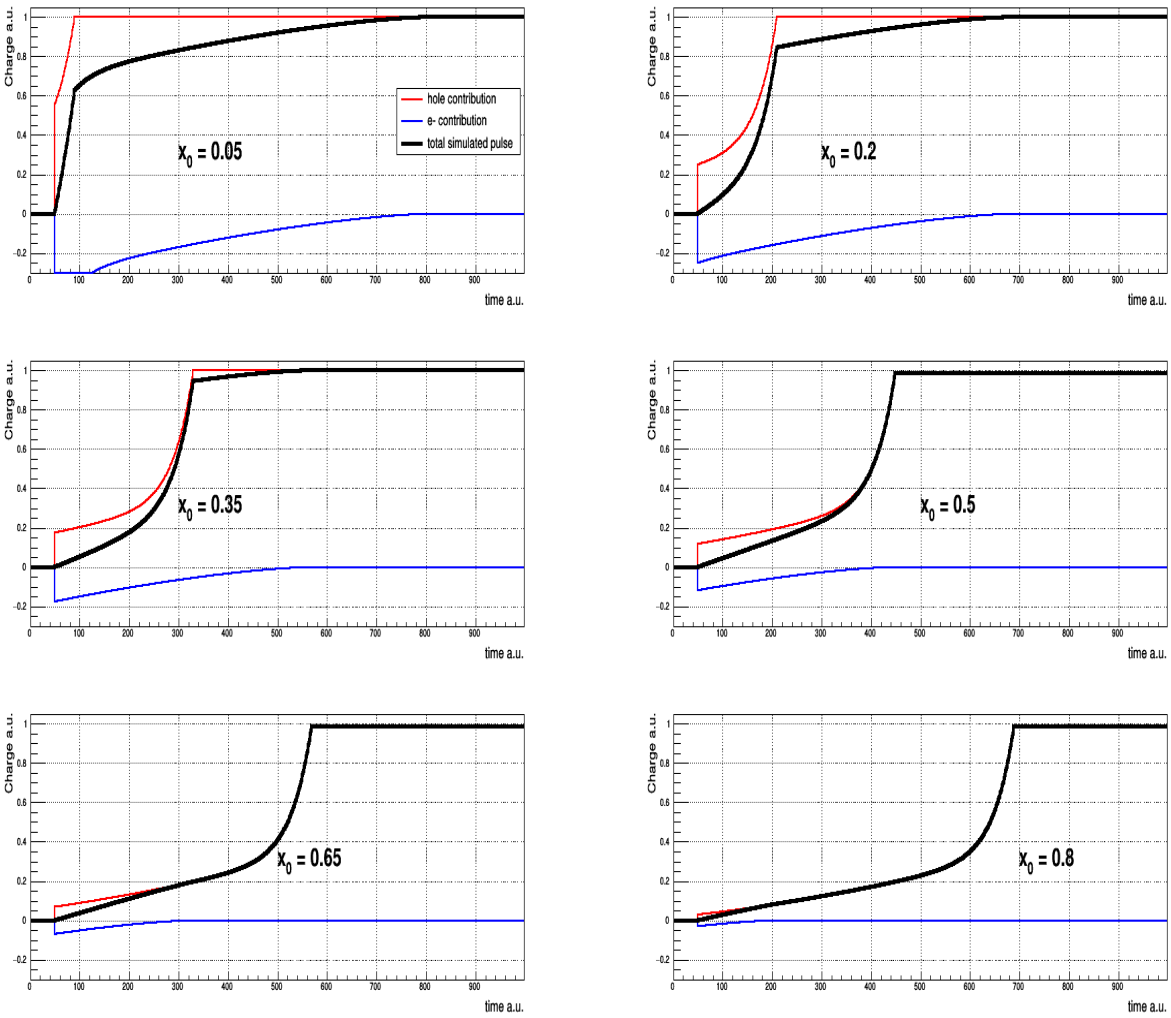

Figure 6.30: Simulated pulses for different starting positions x_0. The hole contribution to the signal is shown in red and the electron contribution is shown in blue. The overall signal is shown in black.

I) The normal component

Here, a fraction of 0.25 times the input charges (both e- and holes) will be calculated as before with the normal velocity, resulting in a normal pulse with a decreased amplitude.

II) The trapped component

Here again, a fraction of 0.25 times the input charges and normal velocities will be taken but the hole component decreases along the way to the p+, mimicking a charge trapping. This way events starting farther away from the p+ are more susceptible to this charge trapping and therefore the signal height will be smaller.

III) The delayed component

Here, the remaining 50 % of the initial charges will be taken and will be moved with a 1000 times decreased velocity through a modified weighting potential. This potential will be arbitrary set to a Gaussian distribution. This step is needed to bring the weighting field down to 0 at the position of the p+ contact The normal weighting field leads to an increasing DCR for events originating close to the p+ what is the opposite to what has been measured.
With this modifications the pulses shown in figure 6.31 can be created.
Compared to the data following observations can be made:

- The model is able to reproduce an energy degradation and an increase of the decay time in dependence of the incident distance.
- The rising edge however is still not reproduced correctly.
- The amount of energy degradation is dependent on the fraction of charge trapping.
- The amount of DCR effect is dependent on the fraction of charges in the modified weighting potential.

From this qualitative approach it could be learned that only the modification of the charge carrier mobilities is not sufficient to reproduce the measured pulses. The energy degradation is only possible if there is a high fraction of charge trapping and some form of recombination. A fraction of the charges must be lost for the signal depending on the drift path. However another fraction of the signal must be produced in a normal way. Otherwise the normal rising edge cannot be reproduced. The DCR, as measured in this work, cannot be understood by only changing charge carrier properties in a normal weighting potential. A fraction of the signal seems to be influenced by a different field configuration.
In conclusion it appears that the observed surface events are affected by several different mechanisms and effects and that the signal formation must be split into different parts that overall shape the signal.
So far also no effects of a charge cloud and its propagation have been taken into account which may alter the signal formation. Recent studies seem to provide a promising shaping effect on the rising edge if the charge cloud and diffusive effects are also taken into account. This is however work to be done in the future.

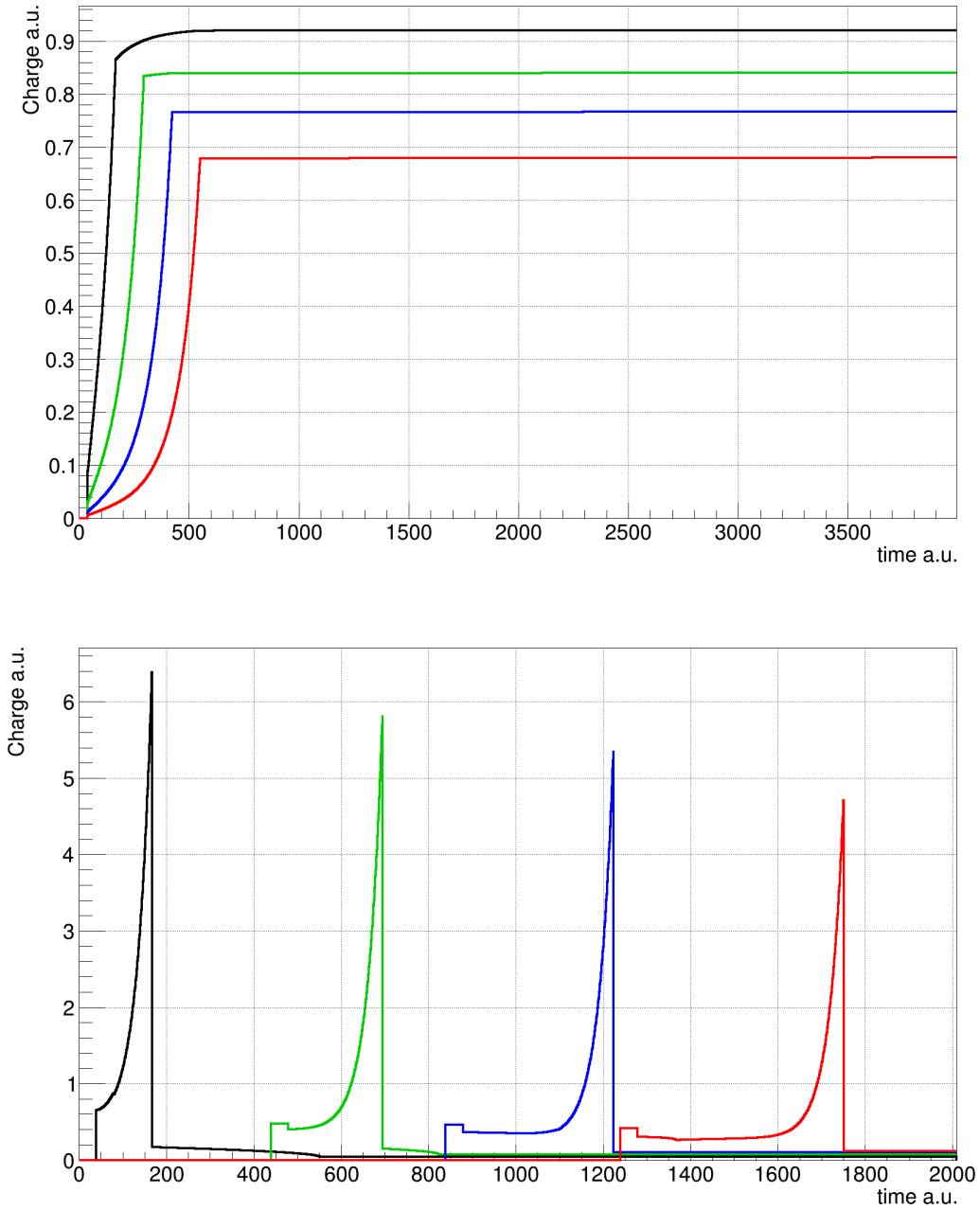

Figure 6.31: The resulting current pulses with the modification of the weighting potential for different starting positions starting from close to the p+ in black and ending at a far away position in red. An time offset has been introduced for the currents for a better visibility.

6.6 Possible beta scans

Overall, the effects that lead to the delay and the degradation of α events are not fully understood yet. There is no satisfying model that explains all observations so far. It is also not clear if the observations are dependent on the sign of the incoming particle and how deep the

observed effects reach into the detector volume.

Material	beta/gamma fraction
Cu-PTFE-Cu	3.5
PTFE	5.9

Table 8: beta to gamma fractions for different collimator designs

One possibility to investigate these possible dependencies would be to employ a beta source (e.g a ^{90}Sr source) instead of the ^{241}Am source and irradiate the detector surface with electrons. However, in order to do so, the collimation system would need to be changed. One big problem with the current collimator would arise since the collimator is partially made out of copper and the emitted electrons would produce a high fraction of Bremsstrahlung. A fraction of these produced Bremsstrahlung photons would also irradiate the detector and the discrimination between photons and electrons would be problematic. Therefore a different collimator design would be needed in order to produce less Bremsstrahlung and to ensure that mostly betas interact with the detector surface. Additionally, the background in the TUBE setup would be needed to be reduced drastically. With the measured background level during the α run, a beta scan seems impossible since the high rate would cover all possible beta candidates.

However, the possibility of a beta scan has been investigated and a decent collimator design has been found by implementing different designs in the previous described MaGe geometry. The properties of a possible ^{90}Sr source could be found and the beta scan campaign has been started to be prepared in the end of 2019.
Unfortunately the COVID-19 outbreak led to an interruption of the preparation and the beta scan could not be performed so far.
Nevertheless the studies of the different collimator design will be briefly presented.

As mentioned the ^{241}Am simulations that have been done before have been recycled for the studies of the possible beta scan. The only difference in the geometry was the material that is used for the collimator. The ^{241}Am source have been collimated with a PTFE - Copper - PTFE cylinder. Especially the Copper would lead to a high production rate of Bremsstrahlung. Therefore a possible beta scan would benefit from the use of a low Z material and the production rate of Bremsstrahlung would decrease. However, the thickness remains still big enough to ensure a proper collimation of the betas. Several designs made out of different materials (PTFE, PET, PVC and Copper) have been implemented and 10^8 decays of ^{90}Sr followed by 10^8 decays

of the daughter ^{90}Y have been simulated for each design. ^{90}Sr decays with a half life of 28.79 years and a Q-value of 546 keV to ^{90}Y, which also decays via beta-decay to ^{90}Zr with a Q-value of 2280 keV and a half life of 3.2 hours. Therefore both isotopes must be taken into account. The Energy depositions along with their position information inside the detector have been collected. Additionally, the information of the particle type of the first interaction point on the detector has been stored, i.e. if an electron or a photon hits the detector. This way it can be ensured if a beta or a gamma deposit the energy. It could be found that the lowest fraction of Bremsstrahlung could be achieved with a full PTFE-based collimator design. The low energy part of the spectrum below 400 keV is dominated by Bremsstrahlung in all designs. Above 400 keV the betas contribute more. Out of the studied designs, a full PTFE collimator showed the biggest fraction of betas above 400 keV. In comparison to the α collimator the beta to gamma ratio nearly doubled. A comparison of different simulated spectra can be seen in figure 6.33. Here, in blue, the energy deposition from the betas and the energy deposition from gammas are shown. The collimation however decreases compared to the α particles. This can be seen in figure 6.32. The incident position of the betas (blue) and the gammas (black) are drawn in the xy-plane. A high uncollimated fraction reaches the detector surface through the slit of the IR-Shield. The collimation can now be increased again with more material, i.e. a bigger collimator. This leads again to an increased fraction of produced Bremsstrahlung. However, it could be found that an increase of the collimator diameter to 70 mm leads to a sufficient collimation, while the fraction of betas remains ca. 1.5 times higher compared to the standard α collimator.

With this trade off a beta scan of the PL should be feasible.

Of course a further background reduction would also be needed. The current background rate would be to high and the betas would be probably covered by gamma background. Given these preparations a beta scan could possibly be performed and the dependence of the sign of the incoming charge and the penetration depth on the PL could be studied.

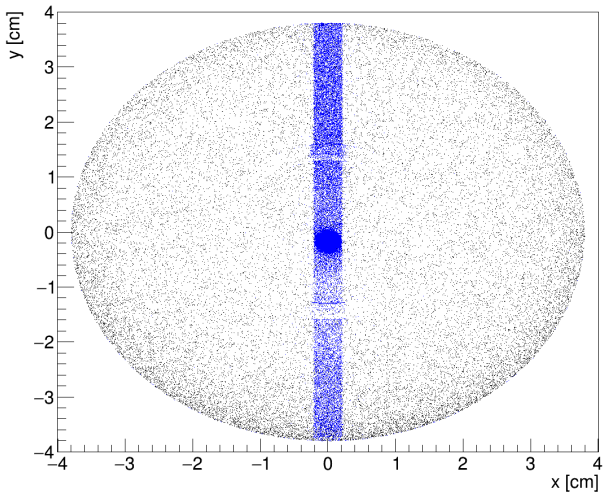

(a) 50 mm diameter full PTFE collimator.

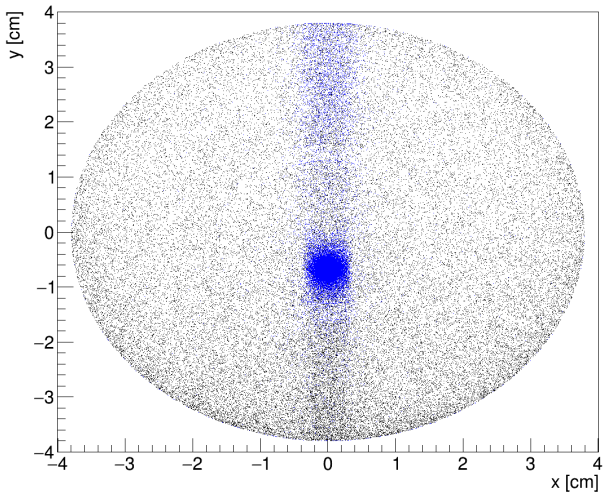

(b) 70 mm diameter full PTFE collimator.

Figure 6.32: The positions of the first particle interaction on the detector in the xy-plane. The betas are shown in blue and in black the γ positions . The strength of the collimation is dependent on the collimator thickness.

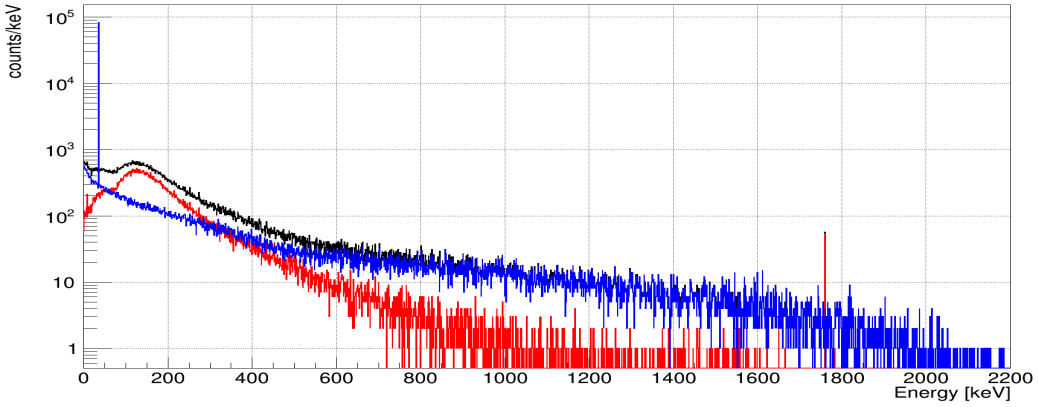

(a) Standard 50 mm Cu-PTFE-Cu collimator.

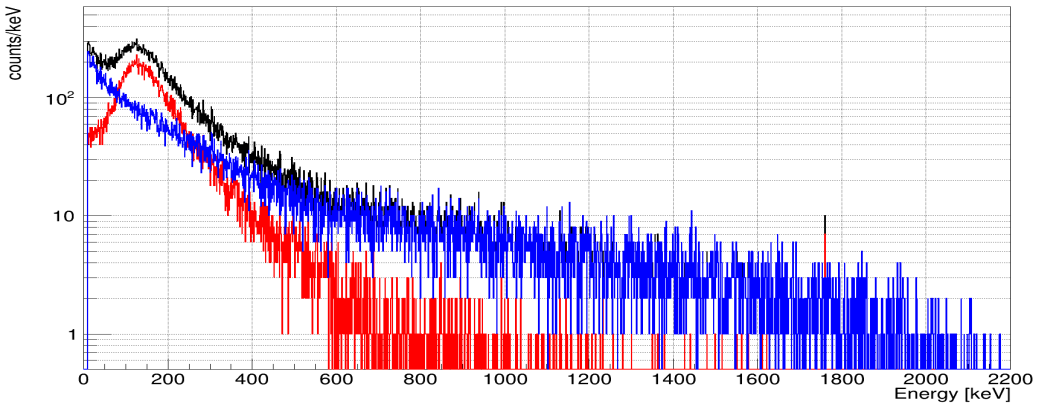

(b) 50 mm full PTFE collimator.

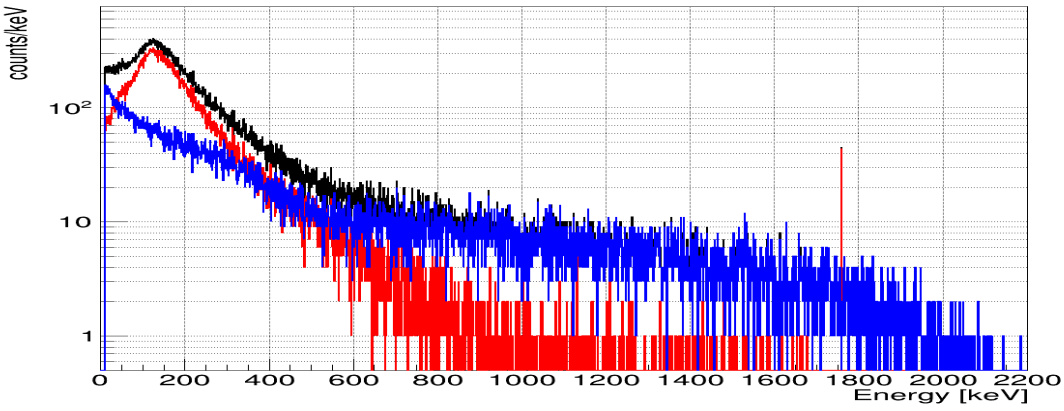

(c) 70 mm full PTFE collimator.

Figure 6.33: Different collimator designs. In black the total deposited energy on the detector is shown. The blue indicates the depositions by electrons and the red the depositions by photons.

7 Summary and conclusion

This work depicted the analysis and evaluation of the newly developed *Inverted Coaxial Point Contact* detector type. The results can be divided into two distinct parts.
At first, a general performance test has been carried out at different test setups. It could be found that the ICPC detector type fulfills the high requirements. A good energy resolution could be found, that however could still be improved by the optimization of the energy estimator and by the application of a charge trapping correction. The good energy resolution could be found in vacuum as well as in LAr.
The PSD performance also showed a very good MSE rejection capability. However, hints of an A/E double structure for SSE could be observed. This structure could be associated with the detector geometry, making it dependent on the drift time of the event. This effect is still under investigation and is unique for IC-detectors.

Furthermore, detailed studies of the detector response to α events in the passivated surface have been carried out. It could be shown that the response of the detector, i.e. the measured signals, change in dependence of the incident position. The response can be summarized as:

- The energy degrades with increasing radii. The farther away the interaction happens to the p+ contact the smaller the measured energy.
- The fraction of recovered delayed charges of the signals increase with increasing radii. The farther away the interaction happens to the p+ contact the higher the decay time.

It could also be shown that the prior to this work established DCR parameter (named DCRpz in this work) is still energy dependent, making statements about the strength of the DCR-effect more complex. An alternative DCR parameter, the DCRn, has been introduced, which normalizes the delayed charge recovery by the energy, leading to a delayed charge recovery fraction. This fraction can be directly compared at different radii and energies.

α PL events show a distinct pulse shape, which can be identified and removed by a multivariate cut procedure. This procedure has been developed within this work. The cut relies on the risetime, the asymmetry of the current pulse and the decay time of the charge pulse. Due to the high background during the campaign an overall cut efficiency could not be found. However

the cut shows a very high efficiency above 90% and with 1 σ statistical uncertainties in the order of 5%.

Models based on the addition of surface charges on the passivated surface and the surface drift of the charge carriers have been tested and it has been found that these models do not reproduce the measured data. The observed effect could not be reproduced only by a delay of the charge carriers. In order to model the DCR-effect, additional weighting fields might be needed, dividing the charge carrier contributions into distinct parts. However, further studies are needed to fully understand this effect and further scan campaigns could help to develop better models. For future campaigns the background should be drastically decreased. This is crucial for a proper determination of the efficiencies. Also the spot size of the incoming α particles should be narrowed with a simultaneous increase of the activity. This way a smaller spot size with a similar event rate can be achieved. Of further interest is also the angular dependence and what effects originate from the different angles. These scans could be performed in the near future with the CAGE scanner at the University of Washington and the surface scanner at the University of North Carolina.
Additionally the response to beta particles could provide further insides of the mechanisms which are shaping the pulses close to the PL.

List of Figures

List of Tables

References

[AAA+13] M Agostini, M Allardt, E Andreotti, AM Bakalyarov, M Balata, I Barabanov, M Barnabé Heider, N Barros, L Baudis, C Bauer, et al. Pulse shape discrimination for gerda phase i data. *The European Physical Journal C*, 73(10):2583, 2013.

[AAAI+19] SI Alvis, IJ Arnquist, FT Avignone III, AS Barabash, CJ Barton, V Basu, FE Bertrand, B Bos, M Busch, M Buuck, et al. Search for neutrinoless double-β decay in ge 76 with 26 kg yr of exposure from the m ajorana d emonstrator. *Physical Review C*, 100(2):025501, 2019.

[AAB+20] M Agostini, GR Araujo, AM Bakalyarov, M Balata, I Barabanov, L Baudis, C Bauer, E Bellotti, S Belogurov, A Bettini, et al. Final results of gerda on the search for neutrinoless double-beta decay. *arXiv preprint arXiv:2009.06079*, 2020.

[AAIB+20] IJ Arnquist, FT Avignone III, AS Barabash, CJ Barton, FE Bertrand, E Blalock, B Bos, M Busch, M Buuck, TS Caldwell, et al. α-event characterization and rejection in point-contact hpge detectors. *arXiv preprint arXiv:2006.13179*, 2020.

[ABB+18] M Agostini, AM Bakalyarov, M Balata, I Barabanov, L Baudis, C Bauer, E Bellotti, S Belogurov, ST Belyaev, G Benato, et al. Upgrade for phase ii of the gerda experiment. *The European Physical Journal C*, 78(5):1–30, 2018.

[ABD17] Matteo Agostini, Giovanni Benato, and Jason A Detwiler. Discovery probability of next-generation neutrinoless double-β decay experiments. *Physical Review D*, 96(5):053001, 2017.

[Ago13] Matteo Agostini. *Signal and background studies for the search of neutrinoless double beta decay in GERDA*. PhD thesis, Technische Universität München, 2013.

[Amm18] Mark Amman. Optimization of amorphous germanium electrical contacts and surface coatings on high purity germanium radiation detectors. *arXiv preprint arXiv:1809.03046*, 2018.

[APZ12] M Agostini, L Pandola, and P Zavarise. Off-line data processing and analysis for the gerda experiment. In *Journal of Physics: Conference Series*, volume 368, page 012047. IOP Publishing, 2012.

[BBC+06] M Bauer, S Belogurov, Yd Chan, M Descovich, J Detwiler, M Di Marco, B Fujikawa, D Franco, V Gehman, R Henning, et al. Mage: a monte carlo framework for the gerda and majorana double beta decay experiments. In *Journal of Physics: Conference Series*, volume 39, page 362. IOP Publishing, 2006.

[BD76] John N Bahcall and Raymond Davis. Solar neutrinos: A scientific puzzle. *Science*, 191(4224):264–267, 1976.

[BHR+00] J Boger, RL Hahn, JK Rowley, AL Carter, B Hollebone, D Kessler, I Blevis, F Dalnoki-Veress, A DeKok, J Farine, et al. The sudbury neutrino observatory. *Nuclear Instruments and Methods in Physics Research Section A: Accelerators, Spectrometers, Detectors and Associated Equipment*, 449(1-2):172–207, 2000.

[BRP+03] René Brun, Fons Rademakers, Suzanne Panacek, Ilka Antcheva, and Damir Buskulic. The root users guide. *CERN, http://root. cern. ch*, 2003.

[Bud09] Dušan Budjáš. *Germanium detector studies in the framework of the GERDA experiment*. PhD thesis, 2009.

[CAS20] Tommaso Comellato, Matteo Agostini, and Stefan Schönert. Modeling the collective motion of charge carriers in germanium semiconductor detectors. *arXiv preprint arXiv:2007.12910*, 2020.

[Cha32] James Chadwick. Possible existence of a neutron. *Nature*, 129(3252):312–312, 1932.

[coled] GERDA collaboration. Test of inverted coaxial 76ge detectors in gerda for future double beta decay experiments. to be published.

[CRHK56] CL Cowan, F Reines, FB Harrison, and HW Kruse. Mcguire, and ad,"detection of the free neutrino: a confirmation,". *Science*, 124(3212):103–104, 1956.

[DJ55] Raymond Davis Jr. Attempt to detect the antineutrinos from a nuclear reactor by the cl 37 (ν, e-) a 37 reaction. *Physical Review*, 97(3):766, 1955.

[DJ64] Raymond Davis Jr. Solar neutrinos. ii. experimental. *Physical Review Letters*, 12(11):303, 1964.

[DMVV16] Stefano Dell'Oro, Simone Marcocci, Matteo Viel, and Francesco Vissani. Neutrinoless double beta decay: 2015 review. *Advances in High Energy Physics*, 2016, 2016.

[FFH+03] S Fukuda, Y Fukuda, T Hayakawa, E Ichihara, Masaki Ishitsuka, Y Itow, T Kajita, J Kameda, K Kaneyuki, S Kasuga, et al. The super-kamiokande detector. *Nuclear Instruments and Methods in Physics Research Section A: Accelerators, Spectrometers, Detectors and Associated Equipment*, 501(2-3):418–462, 2003.

[GGS58] Maurice Goldhaber, L Grodzins, and AW Sunyar. Helicity of neutrinos. *Physical Review*, 109(3):1015, 1958.

[Gru17] Julieta Gruszko. *Surface Alpha Interactions in P-Type Point-Contact HPGe Detectors: Maximizing Sensitivity of 76Ge Neutrinoless Double-Beta Decay Searches*. PhD thesis, 2017.

[HBGS10] M Barnabé Heider, D Budjáš, Konstantin Gusev, and Stefan Schönert. Operation and performance of a bare broad-energy germanium detector in liquid argon. *Journal of Instrumentation*, 5(10):P10007, 2010.

[Heg18] Alexander Hegai. Study on pulse shapes of germanium detectors with a point like contact geometry for the gerda and majorana experiments, phd thesis, 2018.

[KM73] Makoto Kobayashi and Toshihide Maskawa. Cp-violation in the renormalizable theory of weak interaction. *Progress of theoretical physics*, 49(2):652–657, 1973.

[Kno10] Glenn F Knoll. *Radiation detection and measurement*. John Wiley & Sons, 2010.

[Leh15] Björn Lehnert. Search for $2\nu\beta\beta$ excited state transitions and hpge characterization for surface events in gerda phase ii, phd thesis, 2015.

[Maj37] Ettore Majorana. Theory of the symmetry of electrons and positrons. *Nuovo Cim*, 14(171):50, 1937.

[MNS62] Ziro Maki, Masami Nakagawa, and Shoichi Sakata. Remarks on the unified model of elementary particles. *Progress of Theoretical Physics*, 28(5):870–880, 1962.

[Pan18] Krzysztof Panas. *Development of Pulse Shape Discrimination Methods as Tools for Background Suppression in High Purity Germanium Detectors used in the GERDA Experiment*. PhD thesis, Jagiellonian University in Cracow, 2018.

[Pau30] Wolfgang Pauli. Offener Brief an L.Meitner et al.. (German) [open letter to l.meitner], 1930.

[Rad] Mjd _fieldgen and mjd _siggen software, online available at http://radware.phy.ornl.gov/mj/mjdsiggen/ [accessed, 2020].

[Ram39] Simon Ramo. Currents induced by electron motion. *Proceedings of the IRE*, 27(9):584–585, 1939.

[RC56] Frederick Reines and Clyde L Cowan. The neutrino. *Nature*, 178(4531):446–449, 1956.

[Sch97] N. Schmitz. *Neutrinophysik*. Teubner Studienbuecher, 1997.

[Sch18] Christopher Schmitt. Measurement of the spatial location of double escape events in a germanium detector using a pet scanner, phd thesis, 2018.

[Sho38] William Shockley. Currents to conductors induced by a moving point charge. *Journal of applied physics*, 9(10):635–636, 1938.

[SK16] Marco Salathe and Thomas Kihm. Optimized digital filtering techniques for radiation detection with hpge detectors. *Nuclear Instruments and Methods in Physics Research Section A: Accelerators, Spectrometers, Detectors and Associated Equipment*, 808:150–155, 2016.

[Tar15] Andrea Taroni. Nobel prize 2015: Kajita and mcdonald. *Nature Physics*, 11(11):891–891, 2015.

[Wag17] Victoria Elisabeth Wagner. *Pulse Shape Analysis for the GERDA Experiment to Set a New Limit on the Half-life of Neutrinoless Double Beta Decay of Ge-76*. PhD thesis, 2017.

[WAH+57] Chien-Shiung Wu, Ernest Ambler, RW Hayward, DD Hoppes, and Ralph Percy Hudson. Experimental test of parity conservation in beta decay. *Physical review*, 105(4):1413, 1957.

Acknowledgments/Danksagung

Ohne die Hilfe vieler Menschen, die mich mit Rat und Tat in den letzten vier Jahren begleitet haben, wäre diese Arbeit nicht entstanden.

Zuerst möchte ich mich bei meinem Betreuer Professor Josef Jochum bedanken, der mir die Möglichkeit zu dieser Arbeit gegeben hat. Alles begann mit einer spannenden Einführung in die Welt der Neutrinos mit einer Neutrinophysik Vorlesung im Jahr 2014. Über die Suche der Neutrinomasse mit dem ECHo Experiment im Bachelor und im Master Studium, führte mich mein Weg zu der spannenden Frage nach dem eigentlichen Wesens des Neutrinos. Ich habe in all der Zeit viel über die Physik und viel über das faszinierende Feld der Astroteilchen-Experimente gelernt. Dafür möchte ich mich herzlich bedanken.
Ein besonderer Dank gilt auch Ann-Kathrin Schütz, die mich vor allem beim Einstieg in die Kollaboration unterstützt hat und mir oft mit viel Wissen weitergeholfen hat.

I want to give a special thanks to Yoann Kermaidic, who introduced me to the exciting HPGe technology and helped me a lot in the understanding of germanium detectors and the analysis of their data. I could not have done this work without him. Thanks for the discussions, opportunities and beers in Belgium. I have learned a lot.
I also want to thank Tomasso Comellato who became a professional in turning the spindle. Without him , there would not have been any TUBE data in Heidelberg.
I want to thank the whole GERDA and LEGEND collaborations for the opportunity to participate in such great and complex experiments and to travel around the world to learn so much about experimental physics.

Weiterhin möchte ich der gesamten Astroteilchen Gruppe der Uni Tübingen und vor allem der GERDA Gruppe, Katharina, Khushi und Lukas für viele Diskussionen über Physik und außerhalb der Physik danken. Danke auch an die Deutsche Magnetdart Liga und deren Nationalmannschaft Alex, Axel und David für offene Türen und spannende Matches.

Solch eine Arbeit wäre auch nicht möglich gewesen, ohne die vielen Menschen außerhalb der Uni. Danke an alle, die mich über die Jahre begleitet haben.

Ein besonderer Dank gilt Anne, ohne dich hätte ich das nie geschafft. Danke, dass du immer für mich da warst.

Zu guter Letzt möchte ich meinen Eltern danken. Danke für die Unterstützung und den Rückhalt und alles, was ihr für mich getan habt. Ohne euch wäre ich heute nicht hier. Danke.